In-depth Thermokinetic Investigation on Co-pyrolysis of Low-rank Coal and Algae Consortium Blends over CeO_2 loaded Hydrotalcite (MgNiAl) Catalyst

By

Waqar Ul Habib Khan

00000320924

Session 2019-2021

Supervised By

Dr Asif Hussain Khoja

A Thesis Submitted to U.S. – Pakistan Center for Advanced Studies in Energy in partial fulfillment of the requirements for the degree of

MASTERS of SCIENCE

in

THERMAL ENERGY ENGINEERING

U.S. –Pakistan Center for Advanced Studies in Energy (USPCAS-E)

National University of Sciences and Technology (NUST)

H-12, Islamabad 44000, Pakistan

June 2022

In-depth Thermokinetic Investigation on Co-pyrolysis of Low-rank Coal and Algae Consortium Blends over CeO_2 loaded Hydrotalcite (MgNiAl) Catalyst

By

Waqar Ul Habib Khan

00000320924

Session 2019-2021

Supervised By

Dr. Asif Hussain Khoja

A Thesis Submitted to U.S. – Pakistan Center for Advanced Studies in Energy in partial fulfillment of the requirements for the degree of

MASTERS of SCIENCE

in

THERMAL ENERGY ENGINEERING

U.S.– Pakistan Center for Advanced Studies in Energy (USPCAS-E)

National University of Sciences and Technology (NUST)

H-12, Islamabad 44000, Pakistan

June 2022

THESIS ACCEPTANCE CERTIFICATE

Certified that final copy of MS/MPhil thesis written by Mr. Waqar Ul Habib Khan, (Registration No. 00000320924), of U.S.-Pakistan Center for Advanced Studies in Energy (USPCAS-E), NUST has been vetted by undersigned, found complete in all respects as per NUST Statues/Regulations, is in the allowable limits of plagiarism, errors, and mistakes and is accepted as partial fulfillment for the award of MS/MPhil degree. It is further certified that necessary amendments as pointed out by GEC members of the scholar have also been incorporated in the said thesis.

Signature: _____

Name of Supervisor: Dr. Asif Hussain Khoja

Date: _____

Signature (HoD TEE): _____

Date: _____

Signature (Principal/Dean): _____

Date: _____

Certificate

This is to certify that work in this thesis has been carried out by **Mr. Waqar Ul Habib Khan** and completed under my supervision in Fossil Fuels laboratory, USPCAS-E, National University of Sciences and Technology, H-12, Islamabad, Pakistan.

Supervisor:

_____

Dr. Asif Hussain Khoja
U.S.-Pakistan Center for Advanced Studies in Energy
NUST, Islamabad

GEC member 1:

_____

Dr. Rabia Liaquat
U.S.-Pakistan Center for Advanced Studies in Energy
NUST, Islamabad

GEC member 2:

_____

Dr. Mustafa Anwar
U.S.-Pakistan Center for Advanced Studies in Energy
NUST, Islamabad

GEC member 3:

_____

Dr. Abeera Ayaz Ansari
U.S.-Pakistan Center for Advanced Studies in Energy
NUST, Islamabad

HoD-TEE:

_____

Dr. Majid Ali
U.S.-Pakistan Center for Advanced Studies in Energy
NUST, Islamabad

Principal:

_____

Prof. Dr. Adeel Waqas
U.S.-Pakistan Center for Advanced Studies in Energy
NUST, Islamabad

Acknowledgments

All praise and thanks to Allah Almighty, who provided me with the power and skills to comprehend, learn, and complete my thesis report.

It gives me great pleasure to express my heartfelt gratitude to my research supervisor, Dr. Asif Hussain Khoja, for allowing me to join the Fossil Fuels Lab study group, USPCAS-E, NUST, Islamabad. I consider myself fortunate to have worked under his supervision. It was a combination of his patience, perseverance, guidance, and inspiration that enabled me to complete my research goals on time. He showed me the approach to conducting research and presenting the findings as clearly as possible.

I owe a debt of gratitude to the members of my GEC committee, Dr. Abeera Ayaz Ansari, Dr. Rabia Liaquat, and Dr. Mustafa Anwar, who honored my committee's presence. I'd want to express my gratitude to my colleagues and friends for their unwavering support. I'd want to express my gratitude to Lab Engineers Mr. Ali Abdullah and Raja Asim Feroz for their unwavering assistance throughout the research.

I owe my parents, Siblings, and friends a debt of gratitude for their love, prayers, care, and sacrifices in educating and preparing me for the future.

Abstract

This study investigates the co-pyrolysis behaviors of bituminous coal (100%BC), algae consortium (100%AC), and their blends at various blending ratios. The pure and coal-biomass blends were characterized using CHN-S, GCV, and FTIR. Whereas, co-pyrolysis of blends were performed in thermogravimetric analysis (TGA). The deviation between the experimental and calculated values of weight loss (WL%), the residue left (RL%), and the maximum rate of weight loss (wt. %/min) was used to calculate the synergistic effects. Kinetic parameters were investigated using TGA by employing the Coats-Redfern integral method through eighteen reaction mechanisms. The activation energy (E_a) for 100%BC was 85.04 kJ/mol through the F3 model, while for 100%AC showed 78.22 kJ/mol using the D3 model. Thermodynamic parameters such as Enthalpy (ΔH), and Gibbs free energy (ΔG) showed positive values, while Entropy (ΔS) was negative for each coal-biomass blend. The catalytic co-pyrolysis of the optimum blend (20BC-80AC) were studied using CeO_2@MNA as a multifunctional catalyst. Catalytic co-pyrolysis of the optimum blend in an in-situ mixing with the catalyst CeO_2@MNA was performed using TGA. The TG-DTG curve shows the decomposition rate of the optimum blend (20BC-80AC) being affected by the catalyst. The increased WL% shows a positive effect toward a higher yield of volatile matter. The kinetic triplets and thermodynamic parameters were calculated. The E_a of the optimum blend (20BC-80AC) in co-pyrolysis was further lowered through catalytic co-pyrolysis. The E_a of the optimum blend (20BC-80AC) in the first and second stages are (72.48 kJ/mol) and (13.76 kJ/mol), while 3wt.% further reduced its E_a in both stages as (67.82 kJ/mol) and (41.21 kJ/mol). The use of CeO_2@MNA at 3wt.% loading showed a reduction in the peak devolatilization temperature (T_p) of the optimum blend substantially increasing the reaction rate, and reducing the E_a required for the decomposition process.

Keywords:

Bituminous coal; Algae consortium; Co-pyrolysis; Kinetics; CeO_2@MNA; Catalytic co-pyrolysis;

Table of Contents

List of Figures

List of Tables

List of Publications

"In-depth thermokinetic investigation on Co-pyrolysis of low-rank coal and algae consortium blends over CeO_2 loaded hydrotalcite (MgNiAl) catalyst". ***Waqar Ul Habib Khan[1], Asif Hussain Khoja[1,*], Hamad Gohar[1], Salman Raza Naqvi[2], Israf Ud Din[3], Brock Lumbers[4], Mohamed A. Salem[5,6], Abdullah A. Alzahrani[5].***

Journal of Environmental Chemical Engineering (Under Review) (IF = 7.968)

List of Abbreviations

Abbreviation:	Description:
A	Pre-exponential Factor
100%AC	Algae Consortium
100%BC	Bituminous Coal
BC-AC	Bituminous Coal-Algae Consortium
CHN-S	Carbon, Hydrogen, Nitrogen, and Sulfur
DTG	Derivative Thermo-gravimetry
E_a	Activation Energy
FBR	Fixed Bed Reactor
FTIR	Fourier Transform Infrared Spectroscopy
GCV	Gross Calorific Value
GHG	Greenhouse Gases
h	Planck Constant
K	Rate Constant
R	Gas Constant
R^2	Linear Regression
RL%	Residue Left %
TGA	Thermo-gravimetric Analysis
WL%	Weight Loss %
α	Conversion Factor
β	Heating Rate
ΔH	Change in Enthalpy
ΔG	Change in Gibbs free energy
ΔS	Change in Entropy
f(α)	Reaction Mechanism

$g(\alpha)$	Integral Function
k_b	Boltzmann Constant
(wt. %/min)	Maximum Rate of Weight Loss %
T_p	Peak Decomposition Temperature

Chapter 1 Introduction

1.1 Background

Energy production based on fossil fuels (coal, natural gas, and conventional oil) is the cornerstone of economic growth in developed countries. The penalty, however, should be offset by increased economic development [1, 2]. The gas and oil industries are currently dealing with how to develop sustainable energy from conventional resources to save some of their reserves. Natural gas and oil are seen as fast depleting energy sources in the future, while coal reserves can make a significant contribution to meeting future global energy demand because coal reserves are expected to last for the next two centuries. While natural gas will be available for 65 years and oil for 40 years [3].

Coal as a fossil fuel is known to be one of the most important energy sources for energy production in many industrialized and developing countries of the world due to escalating energy demands [4], but it has several negative influences, like its rapidly increasing depletion [5], air pollution, environmental concerns linked to climate change [6], and various health issues caused by the emission of greenhouse gases (GHGs) and their effect during its processing which led to the phenomenon of global warming due to their increased atmospheric CO_2 levels because of coal firing [7] and posing a greater threat in the form of toxic gases such as NO_x and SO_x [8], eventually forcing us to move towards renewable energy [9-11]. The desire for clean renewable fuels has been a greater focus because of the limitations discussed above, globally researchers are exploring options for secure, sustainable, eco-friendly renewable fuels for the future [12-14].

In recent decades, to replace fossil fuels, alternative renewable energy resources have been discovered such as wind, solar, hydro, biodiesel, etc. but none of them provided a permanent solution [9, 11]. Biomass has been acknowledged as a favorable candidate out of all the available renewable resources to meet the global demands [9, 10, 15]. Researchers studied several biomasses considering them as a potential source for sustainable and available renewable energy, currently being the most abundant, and holding about 50% of the total renewable energy produced in the world [16, 17]. Biomass energy ranks fourth in the world behind coal, petroleum, and natural gas, while producing various biofuels, including biodiesel,

biogas, and biohydrogen, as a means of reducing society's reliance on fossil fuels providing a stable energy supply [18-20]. Biomass is the most promising fossil fuel alternative having no impact on the atmosphere and being considered a carbon-neutral fuel, that's why the derived biofuels are regarded as a greener fuel type since they are cheaper, abundant, and can be renewed over time [21]. When a plant grows, it absorbs carbon from the atmosphere for photosynthesis, and when plants biomass burns to generate energy, it releases carbon into the atmosphere. Biomass energy is stored in plants and algae as chemical energy and can be converted into a variety of biofuels through a sequence of conversions to provide clean fuels [22, 23].

Biomass fuel is divided into three generations namely the First-generation includes food crops such as wheat, soybean, rapeseed oil, sugarcane, etc., which have a significant influence on the global food market and increased price. Second-generation biomass known as lignocellulosic-biomass containing hemicellulose, cellulose, and lignin [24], includes agricultural residues, forest waste, municipal and industrial wastes, successfully overcome the shortcomings of first-generation biomass, but the technologies used to convert them have not been successful enough to use on a commercial scale and produce economically viable biofuels along with their biomass seasonality [16, 17]. Marine plants, also called algae, are third-generation biomass-derived biofuels that are not food crops and don't require land for growth, which helps in mitigating the CO_2 emissions due to their excellent CO_2 fixation rate [16, 17, 25]. Algae, such as microalgae and macroalgae have emerged as promising sources for biofuel production in recent years. Their chemical constituents vary in many ways especially their lipid, protein, and carbohydrate contents. Algae consist of 7-23% lipid, 4-57% carbohydrates, and 6-71% of protein content [8, 21, 25]. Algae are one of the most promising bioenergy sources having multiple advantages such as fulfilling high biomass energy needs for biofuel production, because of their large number of species and high O/C and H/C ratio [26], the ability to grow in diverse climatic conditions, as well as being environmentally benign and renewable biomass [27, 28]. Nevertheless, there are some barriers to their sole use, such as taxonomic classification, increased production costs, and less efficient final algal biofuels [18, 29], that must be solved.

1.2 Problem Statement

The individual pyrolysis of coal produces products such as char [30, 31], it also produces liquids and other chemicals, although the yield is poor due to the low quantity of

hydrogen [32], over time it has become less popular compared to biomass pyrolysis, except in nations with high coal reserves [10]. Coal is the main energy source for energy generation in many nations but its reserves are rapidly depleting and its sole use is not efficient through high carbon emissions and low pyrolytic products due to low H/C ratio [6].

The difficulty of exploring and characterizing more types of biomass to alleviate the problem of biomass seasonality and its wide distribution is a challenge [33, 34], due to the increase in the cost of transportation and storage [26]. Mostly in sole biomass pyrolysis, their products have low GCV due to low carbon content, contain high water content, and oxygenated compounds that lead to poor ignition characteristics, corrosion problems, high chemical reactivity, and instability [35]. Despite being good for the environment, pyrolysis oil has worse fuel quality than fossil fuels [36].

It is difficult to define the optimal coal-biomass blending ratio for synergistic effect during co-pyrolysis. Co-pyrolysis products also have some issues such as oxygenated compounds and water contents to further improve their products and provide stability to them, an alternative up-gradation method is required. Understanding the kinetics and thermodynamic behavior of co-pyrolysis and catalytic co-pyrolysis is vital to designing, optimizing, and scaling up industrial co-feed conversion applications for reactor design [37, 38].

1.3 Research hypothesis

Global energy policy is acceptable to reduce the share of coal as a main type of fuel in the world with renewable energy due to the limitations, coal still occupies a leading position in the coming years because some technologies known as co-utilization are developed to provide reasonable power generation [39]. Co-thermochemical conversion of biomass both (lignocellulosic and algal) with coal as a key energy source in many nations, which includes co-pyrolysis, co-combustion, and co-gasification being the suitable options for efficient and coordinated usage of renewable and fossil energy which improves the overall performance [40, 41]. Co-pyrolysis received a lot of attention from academia and industry, having the potential to transform materials into bioenergy [10, 42, 43]. As a result, biomass with a greater H/C ratio can be used to provide hydrogen for coal [44, 45] which helps to increase its structure cracking [26], during co-pyrolysis. Individual pyrolysis has disadvantages such as low GCV, lower volatiles, and higher oxygen content, they are viscous, corrosive, relatively unstable, and chemically very complex so they were improved significantly through the co-pyrolysis process

[43, 46, 47]. Coal can be used with biomass to sometimes offset its seasonal nature and provide sustainable feedstock through co-pyrolysis, so product yields are enhanced [48].

Presently, advanced pyrolysis techniques involve numerous approaches, such as catalytic co-pyrolysis. They aim to improve the selectivity and targeted product yields as well as processing parameters by lowering pyrolysis temperature, and processing time [21, 49], and decreasing the coke formation in catalytic pyrolysis, thus improving the catalyst efficiency [49]. Porous ceramics, alkali metals, metal oxides, Ni-based catalysts, zeolite catalysts, or a mixture of different materials all have been developed as catalyst systems for the process and also improve the characteristics of the products [25, 42, 50]. For this purpose, Bituminous Coal-Algae Consortium (BC-AC) blends were prepared at various blending ratios and characterized to evaluate their physiochemical properties. Each blending ratio was characterized to find out the optimum blending ratio through synergistic effects. Additionally, the kinetics and thermodynamic parameters of (BC-AC) blends were calculated through a detailed study to evaluate the reaction mechanism for each stage of devolatilization. Furthermore, the optimum blend selected was mixed with the catalyst CeO_2@MNA at different loadings to perform catalytic co-pyrolysis in TGA to check their bioenergy potential and stability, both co-pyrolysis and catalytic co-pyrolysis are compared which will help in designing and scaling of co-pyrolysis and catalytic co-pyrolysis reactor.

1.4 Objectives of study

The research conducted in this thesis mainly focuses on the co-pyrolysis and catalytic co-pyrolysis of coal-biomass blends. The goal of this study is to develop and investigates the characterization of coal-biomass blends to assess the chemical and physical properties of separate coal and biomass, as well as how these qualities may change when they are blended. To select an optimum blend through synergistic effects along with the kinetic and thermodynamic analysis. The optimum blend is catalytically co-pyrolyzed to further improve its characteristics for bio-oil production, while further studying its kinetic and thermodynamic parameters. The experimental work reported in this study is consistent and agrees with the previous studies. The study's key objectives are as follows:

- To prepare coal-algae blends at different ratios and evaluate their characteristics.
- To find out the optimum blend that has the highest synergistic effects in terms of WL% or RL%.

- To assess their kinetics and thermodynamic parameters through the Coats-Redfern integral method that will help in approaching the most suitable reaction mechanism for each stage of decomposition during co-pyrolysis.
- To prepare catalytic blends with the optimum blend at different loadings and investigate them through TGA, while further studying their kinetic and thermodynamic parameters and comparing them for the analysis of bioenergy potential.

1.5 Scope of Study

Coal-biomass blends were created and studied to replicate the co-pyrolysis system. The bituminous coal (100%BC) and algae consortium (100%AC) were dried for 12-24 hours at 105 °C after removing the moisture. Both coal and biomass had particle sizes of 0.2 mm after grinding. Heating rate, feedstock type, blending ratio, reaction mechanism, and reactor design are all elements that influence coal and biomass co-pyrolysis. The scope of the research is shown in Fig. 1.1. In this work, different coal-biomass blends were created for the co-pyrolysis process. The coal-biomass blends were analyzed using ultimate analysis (CHN-S), gross calorific value (GCV), and Fourier transform infrared spectroscopy (FTIR). To analyze their co-pyrolysis behavior, TGA analysis of coal-biomass blends was performed in an inert (N_2) atmosphere. The difference between experimental and calculated data was used to calculate the synergistic effects. Using eighteen integral functions, the Coat-Redfern technique was utilized to calculate kinetics parameters such as activation energy (E_a) and pre-exponential factor (A). Change in enthalpy (ΔH), change in Gibbs free energy (ΔG), and change in entropy (ΔS), as well as other thermodynamic parameters, were calculated. Then the catalytic co-pyrolysis of the optimum blend was also carried out in TGA to study its thermal behavior at various catalyst loadings, additionally, its kinetic and thermodynamic behavior was also studied and both co-pyrolysis and catalytic co-pyrolysis blends were compared for the analysis of bio-energy potential.

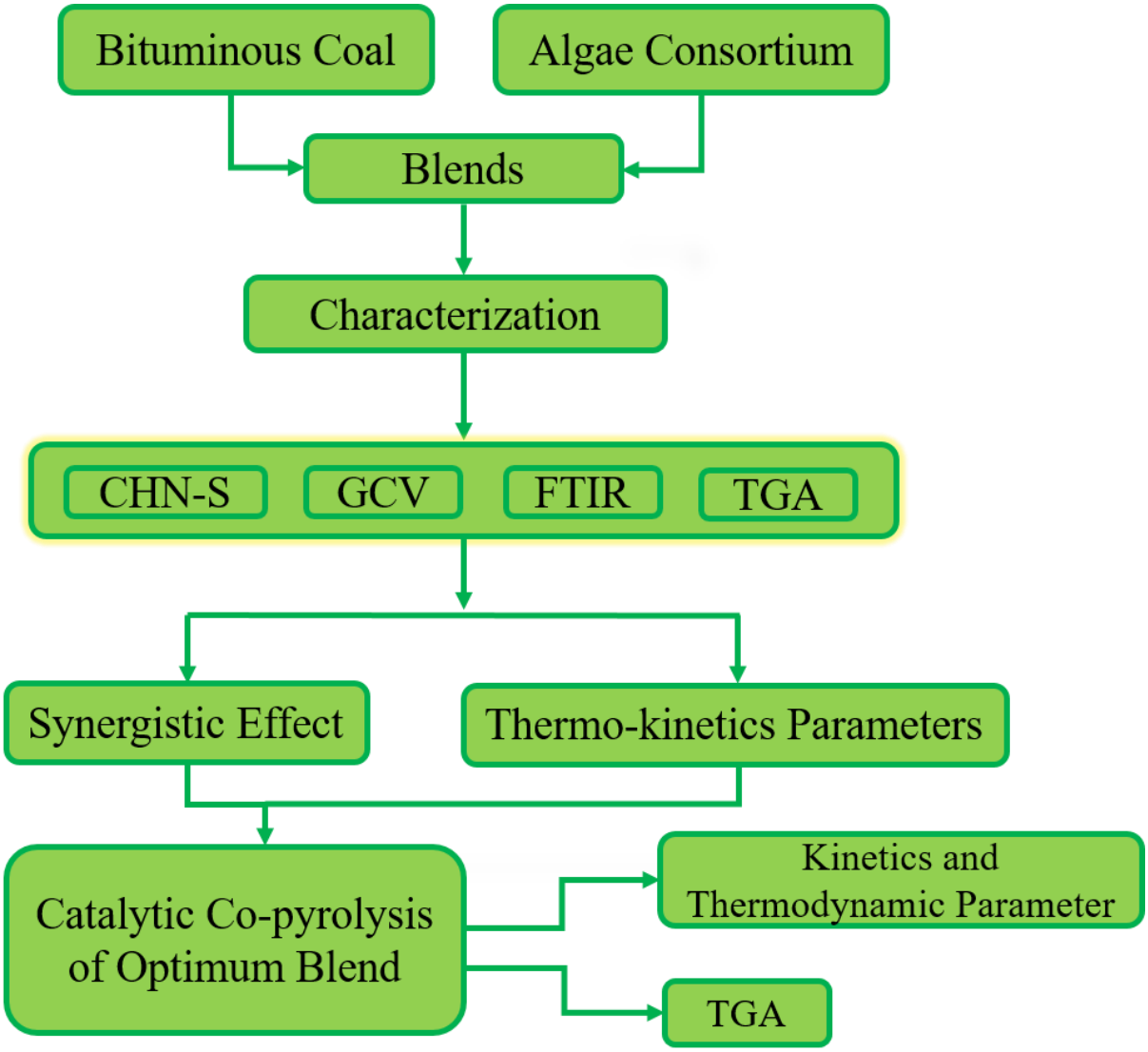

Fig. 1.1 Scope of the Research

1.6 Flow Chart of Thesis

The flow chart of the thesis is shown in Fig. 1.2. The study's goal was to evaluate how biomass and coal may be used more economically and sustainably rather than being thrown away in landfills or polluting the environment. For this goal, a literature review was conducted on existing coal and biomass data and utilization. Coal-biomass blends were prepared and characterized using CHN-S, GCV, FTIR, and TGA. The kinetics and thermodynamics of the co-pyrolysis process were also described using TGA data. TGA was used to perform catalytic co-pyrolysis on the optimum blend. The data from the results were thoroughly reviewed in the results and discussion section.

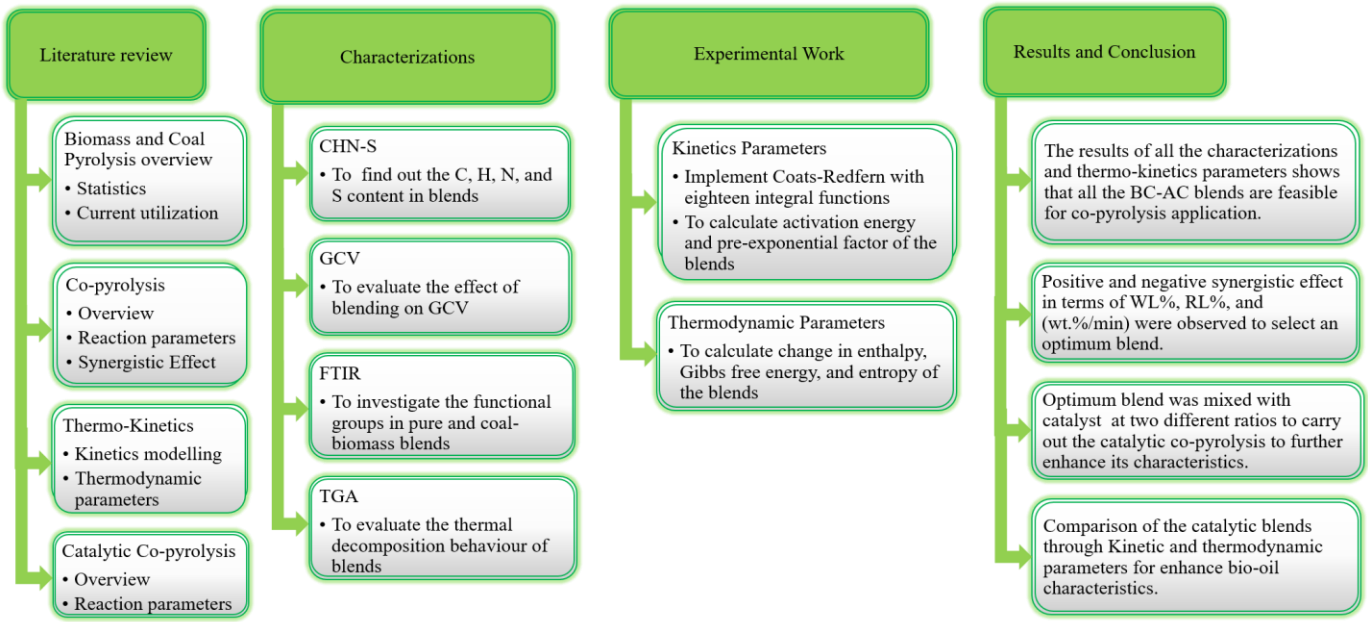

Fig. 1.2 Flow chart of the thesis

Summary

The energy production demands are increasing globally, fossil fuels (coal, natural gas, furnace oil, and shale oil, etc.) are playing a prominent role in fulfilling the desired energy demands. Although, fossil fuels are depleting with time rapidly and are causing severe damage to the environment. Several studies showed coal will be available for about two centuries, whereas natural gas and oil for about 65 and 40 years respectively. Globally researchers are exploring options for secure, sustainable, eco-friendly renewable fuels for the future. Biomass has been acknowledged as a favorable candidate out of all the available renewable resources to meet global demands. But there is some problem with biomass utilization such as in pyrolysis the low carbon content, high moisture, and oxygen content causes the low gross calorific value (GCV) of fuel. Also, in combustion excessive amount of this content causes fouling and slagging in the boiler. As a result, this study looked at the co-pyrolysis of coal-biomass blends and catalytic co-pyrolysis of an optimum blend using a catalyst. Co-pyrolysis solves the challenges associated with individual coal and biomass pyrolysis, catalytic co-pyrolysis further improves the issues associated with co-pyrolysis i.e. quality and yield of bio-oil. Furthermore, combining coal and biomass reduces harmful emissions because biomass is carbon neutral and contains high hydrogen, and less sulfur and nitrogen contents.

References

1. REN, R.J.R.e.p.n.f.t.s.c.P., France: REN21 Secretariat, *Global status report.* 2015.
2. Vuthaluru, H.B., *Thermal behaviour of coal/biomass blends during co-pyrolysis.* Fuel Processing Technology, 2004. **85**(2): p. 141-155.
3. Ismail, T.M., et al., *Coal and biomass co-pyrolysis in a fluidized-bed reactor: Numerical assessment of fuel type and blending conditions.* Fuel, 2020. **275**: p. 118004.
4. Magida, N.E., et al., *Co-combustion Characteristics of coal-Scenedesmus Microalgae Blends and Their Resulting Ash.* Combustion Science and Technology, 2021. **193**(3): p. 419-436.
5. Chia, S.R., et al., *Sustainable approaches for algae utilisation in bioenergy production.* Renewable Energy, 2018. **129**: p. 838-852.
6. Nyoni, B., et al., *Co-pyrolysis of South African bituminous coal and Scenedesmus microalgae: Kinetics and synergistic effects study.* International Journal of Coal Science & Technology, 2020. **7**(4): p. 807-815.
7. Martins, F., C. Felgueiras, and M. Smitková, *Fossil fuel energy consumption in European countries.* Energy Procedia, 2018. **153**: p. 107-111.
8. Das, P., et al., *Recent advances in thermochemical methods for the conversion of algal biomass to energy.* Science of The Total Environment, 2021. **766**: p. 144608.
9. Azizi, K., M. Keshavarz Moraveji, and H. Abedini Najafabadi, *A review on bio-fuel production from microalgal biomass by using pyrolysis method.* Renewable and Sustainable Energy Reviews, 2018. **82**: p. 3046-3059.
10. Gouws, S.M., et al., *Co-pyrolysis of coal and raw/torrefied biomass: A review on chemistry, kinetics and implementation.* Renewable and Sustainable Energy Reviews, 2021. **135**: p. 110189.
11. Jalilian, N., G.D. Najafpour, and M. Khajouei, *Macro and Micro Algae in Pollution Control and Biofuel Production – A Review.* ChemBioEng Reviews, 2020. **7**(1): p. 18-33.
12. Halder, P. and K. Azad, *Recent trends and challenges of algal biofuel conversion technologies*. 2019.
13. Kaloudas, D., N. Pavlova, and R. Penchovsky, *Lignocellulose, algal biomass, biofuels and biohydrogen: a review.* Environmental Chemistry Letters, 2021. **19**(4): p. 2809-2824.
14. Srivastava, N., et al., *Substrate Analysis for Effective Biofuels Production.* Clean Energy Production Technologies, 2020.
15. Bach, Q.-V. and W.-H. Chen, *Pyrolysis characteristics and kinetics of microalgae via thermogravimetric analysis (TGA): A state-of-the-art review.* Bioresource Technology, 2017. **246**: p. 88-100.
16. Vasudev, V., X. Ku, and J. Lin, *Pyrolysis of algal biomass: Determination of the kinetic triplet and thermodynamic analysis.* Bioresource Technology, 2020. **317**: p. 124007.
17. Walia, A., et al., *Co-Conversion of Algal Biomass to Biofuel*, in *Liquid Biofuels*. 2021. p. 391-439.
18. Gautam, R. and R. Vinu, *Reaction engineering and kinetics of algae conversion to biofuels and chemicals via pyrolysis and hydrothermal liquefaction.* Reaction Chemistry & Engineering, 2020. **5**(8): p. 1320-1373.
19. Sharma, A. and S.K. Arya, *Hydrogen from algal biomass: A review of production process.* Biotechnology Reports, 2017. **15**: p. 63-69.
20. Uzoejinwa, B.B., et al., *Co-pyrolysis of macroalgae and lignocellulosic biomass.* Journal of Thermal Analysis and Calorimetry, 2019. **136**(5): p. 2001-2016.

21. Lee, X.J., et al., *State of art review on conventional and advanced pyrolysis of macroalgae and microalgae for biochar, bio-oil and bio-syngas production.* Energy Conversion and Management, 2020. **210**: p. 112707.
22. Xu, G., et al., *Non-natural catalysts for catalytic tar conversion in biomass gasification technology.* International Journal of Hydrogen Energy, 2021.
23. Zhang, K., F. Zhang, and Y.-R. Wu, *Emerging technologies for conversion of sustainable algal biomass into value-added products: A state-of-the-art review.* Science of The Total Environment, 2021. **784**: p. 147024.
24. Yuan, T., A. Tahmasebi, and J. Yu, *Comparative study on pyrolysis of lignocellulosic and algal biomass using a thermogravimetric and a fixed-bed reactor.* Bioresource Technology, 2015. **175**: p. 333-341.
25. Lee, J., E.E. Kwon, and Y.-K. Park, *Recent advances in the catalytic pyrolysis of microalgae.* Catalysis Today, 2020. **355**: p. 263-271.
26. Li, S., et al., *Study on co-pyrolysis characteristics of rice straw and Shenfu bituminous coal blends in a fixed bed reactor.* Bioresource technology, 2014. **155C**: p. 252-257.
27. Sekar, M., et al., *A review on the pyrolysis of algal biomass for biochar and bio-oil – Bottlenecks and scope.* Fuel, 2021. **283**: p. 119190.
28. Vasudev, V., X. Ku, and J. Lin, *Combustion Behavior of Algal Biochars Obtained at Different Pyrolysis Heating Rates.* ACS Omega, 2021. **6**(29): p. 19144-19152.
29. Vassilev, S.V. and C.G. Vassileva, *Composition, properties and challenges of algae biomass for biofuel application: An overview.* Fuel, 2016. **181**: p. 1-33.
30. Tahmasebi, A., et al., *Pressurized entrained-flow pyrolysis of lignite for enhanced production of hydrogen-rich gas and chemical raw materials.* Journal of Analytical and Applied Pyrolysis, 2020. **145**: p. 104741.
31. Zhang, W., et al., *The evolution characteristics of bituminous coal in the process of pyrolysis at elevated pressure.* Fuel, 2021. **302**: p. 120832.
32. Miura, K., *Mild conversion of coal for producing valuable chemicals.* Fuel Processing Technology, 2000. **62**(2): p. 119-135.
33. Jin, X., et al., *Co-pyrolysis of rice straw and water hyacinth: Characterization of products, yields and biomass interaction effect.* Biomass and Bioenergy, 2019. **127**: p. 105281.
34. Yang, Z., et al., *Recent advances in co-thermochemical conversions of biomass with fossil fuels focusing on the synergistic effects.* Renewable and Sustainable Energy Reviews, 2019. **103**: p. 384-398.
35. Abnisa, F. and W.M.A. Wan Daud, *A review on co-pyrolysis of biomass: An optional technique to obtain a high-grade pyrolysis oil.* Energy Conversion and Management, 2014. **87**: p. 71-85.
36. Oasmaa, A. and S. Czernik, *Fuel Oil Quality of Biomass Pyrolysis OilsState of the Art for the End Users.* Energy & Fuels, 1999. **13**(4): p. 914-921.
37. White, J.E., W.J. Catallo, and B.L. Legendre, *Biomass pyrolysis kinetics: A comparative critical review with relevant agricultural residue case studies.* Journal of Analytical and Applied Pyrolysis, 2011. **91**(1): p. 1-33.
38. Zhang, X., et al., *Thermal behavior and kinetic study for catalytic co-pyrolysis of biomass with plastics.* Bioresource technology, 2016. **220**: p. 233-238.
39. Larionov, K.B., et al., *Combustion of bituminous coal and semicoke with copper salts.* Fuel Processing Technology, 2021. **213**: p. 106706.
40. Fakayode, O.A., et al., *Co-pyrolysis of lignocellulosic and macroalgae biomasses for the production of biochar – A review.* Bioresource Technology, 2020. **297**: p. 122408.

41. Li, Y., et al., *Studies on individual pyrolysis and co-pyrolysis of peat–biomass blends: Thermal decomposition behavior, possible synergism, product characteristic evaluations and kinetics.* Fuel, 2022. **310**: p. 122280.
42. Wang, Y., et al., *Hydrogen-rich syngas production from biomass pyrolysis and catalytic reforming using biochar-based catalysts.* Fuel, 2022. **313**: p. 123006.
43. Wu, Z., et al., *Co-pyrolysis behavior of microalgae biomass and low-rank coal: Kinetic analysis of the main volatile products.* Bioresource Technology, 2019. **271**: p. 202-209.
44. Tang, F., et al., *Catalytic co-pyrolysis behaviors, product characteristics and kinetics of rural solid waste and chlorella vulgaris.* Bioresource Technology, 2020. **299**: p. 122636.
45. Hassan, H., J.K. Lim, and B.H. Hameed, *Recent progress on biomass co-pyrolysis conversion into high-quality bio-oil.* Bioresour Technol, 2016. **221**: p. 645-655.
46. Chen, W., et al., *Co-pyrolysis of lignocellulosic biomass and microalgae: Products characteristics and interaction effect.* Bioresource Technology, 2017. **245**: p. 860-868.
47. Wu, Z., et al., *Synergistic effects from co-pyrolysis of lignocellulosic biomass with low-rank coal: A perspective based on the interaction of organic components.* Fuel, 2021. **306**: p. 121648.
48. Vuppaladadiyam, A.K., et al., *Thermogravimetric and kinetic analysis to discern synergy during the co-pyrolysis of microalgae and swine manure digestate.* Biotechnology for Biofuels, 2019. **12**(1): p. 170.
49. Shafaghat, H., et al., *In-situ and ex-situ catalytic pyrolysis/co-pyrolysis of empty fruit bunches using mesostructured aluminosilicate catalysts.* Chemical Engineering Journal, 2019. **366**.
50. Nishu, et al., *A review on the catalytic pyrolysis of biomass for the bio-oil production with ZSM-5: Focus on structure.* Fuel Processing Technology, 2020. **199**: p. 106301.

Chapter 2 Literature Review

2.1 Biomass Overview

Biomass resources are one of the world's potentially plentiful energy resources; annual primary output surpasses 4500 EJ, with 2900 EJ as potential bioenergy, around 270 EJ of which is sustainable. Global biomass residues and wastes, which comprise byproducts of food, fiber, and forest production, currently exceed 110 EJ per year, with only around 10% of that being used for energy. Residues concentrated at industrial sites are currently the most widely used biomass source in the commercial sector [1]. Pakistan generates roughly 220 billion tonnes of biomass and municipal solid waste per year, indicating a significant improvement in energy output. A significant portion of it is inefficiently burned in open places, harming the environment. According to the International Energy Agency, biofuels could meet around 27% of the world's fuel needs by 2050. This shows that biofuels have a lot of potential and can meet the masses' future energy needs. In advanced countries, agricultural waste is used as biomass fuel for sustainable energy generation, however, biomass is still underutilized in developing countries. The World Bank has published an atlas with a study on Pakistan's biomass energy potential, which includes sugar mills, rice plants, municipal solid waste dumps, and dairy farms. Crop leftovers in agricultural fields that are left or discarded because they are no longer useful.

According to the report, agricultural processing leftovers have a potential of 25.3 million tonnes per year, with an equivalent energy potential of 61,838 GWh/year, while crop harvesting residues have a potential of 114 million tonnes per year, with an equivalent energy potential of 448,990 GWh/year. Pakistan is expecting to gather over 20 million tonnes of organic garbage this year, a 2.4 percent increase over the previous year. Karachi generates approximately 9000 tonnes of municipal trash every day. When energy-saving measures are implemented, on the one hand, reliance on traditional fossil fuels can be reduced and finally phased out if widespread consideration is given to biomass fuel technology adaptation [2]. The three main components that make up the majority of biomass are hemicellulose, lignin, and cellulose. Hemicellulose is a polysaccharide composed of shorter chains (500-3000 sugar units), accounting for 25-30% of the biomass. Hemicellulose begins to dissolve at 150 degrees Celsius, and significant weight loss occurs at 200 degrees Celsius. Light volatiles is generated

during the thermal degradation of hemicellulose, resulting in fewer char and tars [3]. Cellulose, a polymer with a molecular weight of 106 or more, is the fibrous component of wood and biomass. Because of its more crystalline structure than hemicellulose, cellulose resists heat decomposition. Cellulose decomposes at temperatures ranging from 240 to 350 degrees Celsius [4]. Lignin is a component of plant cell walls that fills the gaps between cellulose, hemicellulose, and pectin. The thermal decomposition of lignin begins between 280 and 500 degrees Celsius, producing phenols [5]. Fig. 2.1 shows how biochemical and thermochemical processes can transform biomass into fuels and chemicals. The most prevalent thermochemical processes are pyrolysis, hydrothermal liquefaction, gasification, combustion, and hydrothermal carbonization [6].

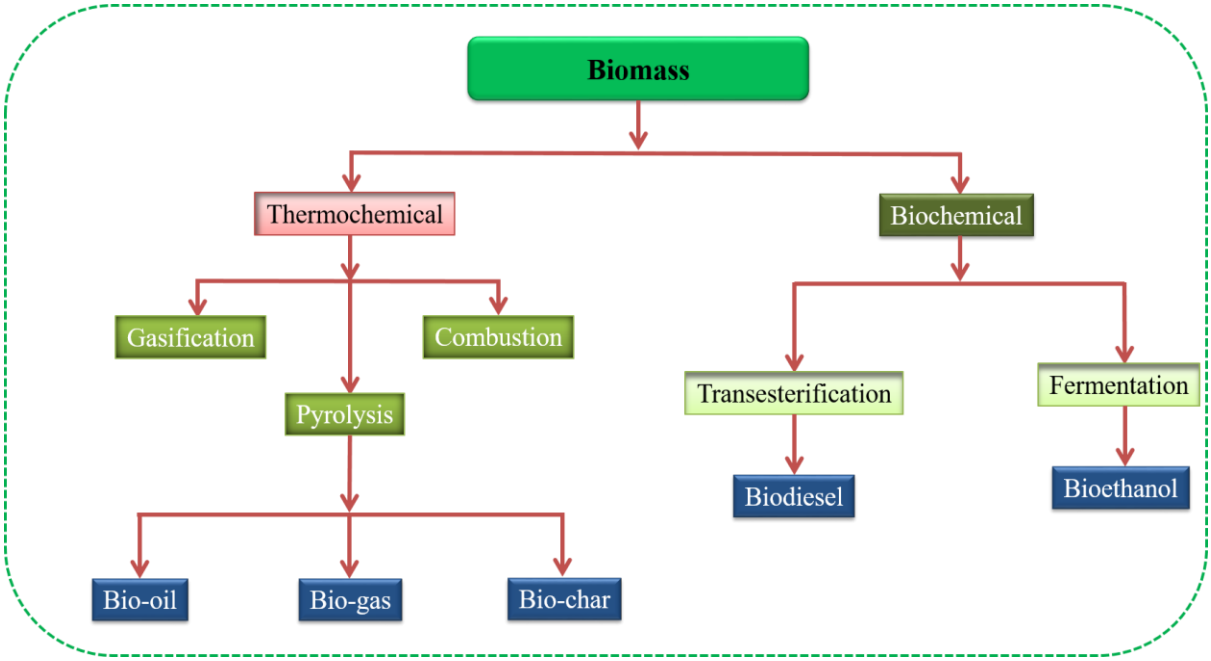

Fig. 2.1 Biomass utilization pathway for biofuels production

2.1.1 Biomass pyrolysis

Biomass pyrolysis is a thermochemical process in which the thermal decomposition of organic matter occurs in the absence of oxygen. To generate a high yield of hydrogen-enriched syngas, this process is often run at a high temperature (600–900°C), with modest heating rates and a longer residence time.

Fast pyrolysis in biomass pyrolysis combines high heating rates and short hot vapor residence times (less than one second) to create a liquid with a 75% yield. The pyrolysis liquid, also known as bio-oil, has the potential to be converted into transportation fuels and valuable

chemicals. Char and other gaseous products, such as methane, might be burned to create the energy needed for the pyrolysis reaction. Because of the increasing demand for liquid transportation fuels, biomass pyrolysis technology is gaining traction in academics and business [6, 7]. Atmospheric pressure can be used for pyrolysis. As a result, pyrolysis has sparked public interest in converting biomass into liquid fuel. Slow and fast pyrolysis are the two types of biomass pyrolysis based on the heating rate. Because of its rapid reaction rate and much higher bio-oil yields, fast pyrolysis is currently the preferred method [8].

Fast pyrolysis has been the topic of numerous investigations, including the investigation of pyrolysis mechanisms, reaction processes, and reactor design, as well as the development of catalytic pyrolysis catalysts. Many authors explored the reaction pathways of biomass components during pyrolysis. Three essential mechanisms are considered for biomass pyrolysis: char generation, depolymerization, and fragmentation. Secondary reactions that can occur include cracking and recombination [8]. Biomass pyrolysis is performed in a different type of reactor and reactor type affects the yield of the product.

2.2 Coal Overview

The majority of coal is composed of carbon and hydrocarbons, which have a high energy density and are created when coal is burned (burning). Coal-burning became a movement during the First Industrial Revolution. This energy source was groundbreaking from an economic standpoint. Ambient air pollution, on the other hand, is damaging to the environment [9-11]. Coal output is increasing as demand for low-cost electricity, iron, steel, and cement rises. Coal, which has an estimated 1.1 trillion tonnes of verified reserves worldwide, will last around 115 years longer than conventional oil and gas reserves, depending on current extraction rates. The world's coal production is controlled by ten countries, which account for 90 percent of global output. China has been the world's largest coal producer for the past three decades (with over a third of total reserves), followed by the United States of America, India, Australia, Indonesia, Russia, South Africa, Kazakhstan, Columbia, and Ukraine [12].

Coal is the world's second most important energy source, accounting for 40% of total primary energy use [13]. Coal is used as a primary energy source in many developing countries. In Paris in December 2015, all nations pledged to invest in and intensify efforts to avert global warming and establish a sustainable, low-carbon future. The Paris Agreement's goal is to

reduce greenhouse gas emissions [14]. Because most poor countries are obsessed with the here and now rather than the future, the goals are unlikely to be realized. Toxins released by power plants into the environment can be harmful to people's health [15]. Not only is coal burning hazardous to one's health, but the massive volume of coal dust produced during extraction and transportation is also a source of xenobiotic diseases for workers and adjacent communities [16]. Low and middle-income countries, with around 97 percent of their cities with populations greater than 0.1 million, do not meet WHO air quality criteria [17]. Although coal combustion is one of the pollutants, it is also essential to note that coal transportation, point-source residential heating and cooking sources, and automotive fuel combustion all contribute to pollution. The ability of an organism to function properly is determined by the quality of the air it breaths [18].

Lignite (60-75% carbon on a dry ash-free basis, 30-70 % moisture) is made from compacted peat. It is also low-rank coal that is highly volatile and is mostly used in power plants. It is used in the generation of electricity. Polished "jet" lignite is frequently used to create decorative stones [19]. Subbituminous coal (carbon content varies between 71 and 77 percent on a dry ash-free basis): It's substantial and ranges from dusky brown to lean black, with a moisture level of 15-30%. The heat content of this coal ranges from 8300 to 11500 BTU/lb. It is used to produce steam-powered energy [20]. Bituminous coal (carbon content ranges from 77 to 87 percent): This form of coal is dense black with a carbon content of 77-87 percent and a moisture level of 1.5-7 percent. Bituminous coal is dense, black coal that is formed by compressing and breaking down lignite. These coals are often used in the manufacture of briquettes and power plants, as well as the manufacture of coke. It has two to three times the heat content of lignite coal [21]. Anthracite (carbon content varies between 86 and 97 percent): It has a black vitreous gloss and is the best ignitable coal. It is the most abrasive coal variety. It is a non-smoking fuel that is generally utilized in homes and businesses. It generates a lot of heat and burns for a long time. It contains a low proportion of sulfur [22]. Coal accounts for only 0.2 percent of overall electrical output in Pakistan. Its primary function is to generate heat. It is inexpensive, yet it is damaging to the environment. If the right coal policies are put in place, it can lead to significant growth [23].

2.2.1 Coal pyrolysis

It is the thermal decomposition of coal that occurs at higher temperatures under the complete absence of oxygen to produce char and other products. The pyrolysis of coal produces

liquids and other chemicals, however, the yield is poor due to the low amount of hydrogen [23]. Coal pyrolysis is an intriguing technology for enhancing fluid quality and output, but it is not generally employed in the industry due to the high cost of hydrogen [24]. Over time it has become less popular compared to biomass pyrolysis, except in nations with high coal reserves [25]. Coal is the main energy source for energy generation in many nations but its reserves are rapidly depleting and its sole use is not efficient through high carbon emissions and low pyrolytic products due to low H/C ratio [26], thus requiring hydrogen-rich biomass because chemical structure cracking needs more hydrogen.

2.3 Co-pyrolysis

Co-pyrolysis of coal or biomass with readily available materials could be a cost-effective way to make biofuels [27]. Biomass co-pyrolysis is gaining popularity as a feasible substitute method for increasing pyrolysis product quality. Co-pyrolysis, as opposed to basic biomass rapid pyrolysis, uses a variety of raw materials as feedstock in addition to biomass, such as plastics, coal, sludge, tyres, and so on. Co-pyrolysis is distinguished by the synergistic influence of chemical interactions between diverse feedstocks. However, the synergistic effect differs greatly depending on the additional raw materials used in co-pyrolysis.

As a result, coal and biomass co-pyrolysis may yield liquid and gaseous products with high economic value, exceeding the limitations of separate coal and biomass pyrolysis [28]. Biomass could provide hydrogen during the process, rapidly producing volatile compounds in significant quantities. Improving gas-lignite contact may result in changes in product distribution, kinetics, and tar and gas composition, as well as improved char gasification and interaction with the gaseous phase during secondary tar, cracking. Incorporating biomass into coal is a viable option for reducing our reliance on fossil fuels while also addressing the environmental challenges faced by CO_2 emissions from coal; CO_2 emissions are the second most significant cause of global warming [29]. The research of co-pyrolysis is a contentious topic. Its major goal is to improve coal thermal transformation. The majority of previous research [30, 31] has shown little evidence of a synergistic effect between coal and biomass. Recent research [32-35] has revealed the importance of co-pyrolysis interactions in TGA. Other studies [36, 37] have discovered that they have a synergistic influence on pyrolytic product yields, gaseous component yields, tar component yields, and char reactivities. Table 2.1 illustrates the literature review of coal and various biomasses at different operating conditions and in different reactors. Coal is an excellent fuel for biomass co-pyrolysis due to its high

energy density and low cost. The co-pyrolysis process is influenced by alkali and alkaline-earth metals in biomass, as well as hydrogen donors. Research on the synergistic effects that occur when biomass and coal are combined is still needed.

Table 2.1 Literature review on co-pyrolysis of coal and biomass

Co-pyrolysis Feedstock	**Biomass (wt. %) in the blend**	**Gas/Flowrate (mL/min)**	**Reactor**	**Heating rate (°C/min)**	**Temperature (°C)**	**Ref.**
legume straw and Dayan lignite	0/20/40/60/ 80/100	N_2/35	Free fall reactor	8.3	500 – 700	[36]
Rice straw and bituminous coal	0/20/40/60/ 80/100	N_2/500	Fixed bed reactor	NR	700 – 900	[28]
Rice straw, sawdust, microcrystalline cellulose, lignin, and Bituminous coal	0/20/40/60/ 80/100	N_2/150	TGA	10/15/20/25/ 30	25 – 900	[38]
Sawdust and bituminous coal	0/20/40/60/ 80/100	N_2/500	Drop tube furnace and fixed bed reactor	NR	DTF = 800 – 1400 FBR = 25 – 800	[39]
Pine and sub-bituminous coal	0/25/50/75/ 100	N_2	TGA and free fall reactor	10	25 – 800	[40]
Corn stalks and bituminous coal	0/25/50/75/ 100	N_2/20	TGA	10/20/30/40/ 60	40 – 850	[41]
Rice Husk and Coal	0/20/40/60/ 80/100	N_2/35	TGA and Fixed Bed Reactor	20	TGA = 25 – 900 FBR = 750	[42]
Sawdust, Hemp, and Coal	0/20/40/60/ 80/100	N_2/35	TGA	20	25 – 900	[43]

2.3.1 Synergistic effects

The interaction of biomass and coal was explored by comparing experimental data to theoretical data, which is the sum of each sample value in proportion to its blending value. The percentage increase or decrease in experimental outcomes relative to theoretical values is referred to as a synergistic effect. Because there are so many variables to examine, the conclusions of some organizations may be inconsistent. To put it another way, co-pyrolysis practices involving biomass and coal have demonstrated synergistic or cumulative effects. The pyrolysis of coal-biomass blends in various coal and biomass ratios was found to have no synergistic impact using thermogravimetric analysis (TG), and the char generation and the ratio of biomass in the blend were proven to have a linear relationship [30]. Pan et al. [44] and Kastanaki et al. [45] both confirmed that biomass and coal in a blend did not interact during pyrolysis. Chen et al.[34], Shui et al. [35], and Aboyade et al. [46], have challenged this viewpoint, indicating that substantial interactions between the coal and biomass fractions occur during pyrolysis in TGA. Li et al. [39], Sonobe et al. [31], and Onay et al. [33] said that pyrolysis goods, tar, gaseous, and char component yields all confirmed the presence of a synergistic effect. Park et al. [47] found the interaction in both fixed-bed reactors and TG, however, Sonobe et al. [31], who studied the co-pyrolysis of corncob and lignite discovered that synergy occurs in a fixed bed reactor rather than a TG device. Furthermore, studies that examined the dispersion of major products such as char, gas, and liquid found minimal evidence of a synergistic effect [48], Those who investigate the makeup of the volatiles, on the other hand, are more likely to reach the opposite result [49]. It is difficult to prove synergy in co-pyrolysis because it is dependent on the type of fuels used and the pyrolysis technology used. These conflicting results are perplexing and require clarification. A flood of reviews has resulted from individual investigations on coal and biomass pyrolysis [50, 51]. Instead of this, there are few reviews on the co-pyrolysis of coal-biomass blends [52]. During co-pyrolysis, the hydrogen released from biomass can stabilize the large radicals produced from coal resulting in improved oil yield and quality [28].

2.4 Factors that affect the co-pyrolysis process

2.4.1 Feedstock type

The main component that might entice the synergy should be the types of blending fuels. Many coal-biomass blends, such as hazelnut shells-coal, have been demonstrated to be

effective [53], legume straw-coal [36], corncob-coal [31], microalgae-coal [31], sawdust-coal [54], and corn stalk-sub-bituminous coal [55], show synergetic effects during co-pyrolysis. Minerals are the primary chemical components of biomass, as are hemicellulose, cellulose, and lignin extractives. Cellulose, hemicellulose, and lignin may have cumulative effects on the thermal behaviour of coal [56]. In co-pyrolysis, the OH and H functional groups of biomass promote the cracking of coal's aromatic rings [57, 58]. According to certain studies, biomass natural resources facilitated interaction between coal and biomass [59]. According to Yuan et al. [60], in co-pyrolysis, hemicellulose has the largest effect on coal cracking and conversion. The hemicellulose and cellulose constituents of biomass are primarily responsible for the volatiles created by pyrolysis, which can then be used to make hydrogen via secondary processes. Lignin in biomass may facilitate low-temperature polymerization reactions, resulting in the creation of reactive radicals and stabilised phenoxy radicals [61, 62].

Many studies have revealed that synergy among biomass and low-rank coals can occur easily during co-pyrolysis and that interactions are stronger than interactions between high-rank coal and biomass [53, 60, 63, 64]. In addition, when the coal rank is low, the primary pyrolytic zones are shifted to lower temperatures [65]. Immediately, the hydrogen acceptor ability of low-ranked coal was superior to that of high-ranked coal [66]. During the procedure, the coal's structures will be broken, resulting in significant coal fragmentation into hydrogen with no active sites. Between biomass and coal, a hydrogen transfer process occurs. Because low-rank coals have a higher capacity for hydrogen uptake, the synergistic positive effect is more visible.

2.4.2 Blending ratio

The biomass component of the blend had a substantial impact on the distribution of liquid, solid, and gas products [49]. By increasing the blending ratio, the char yield is reduced but the gas and liquid yields are raised [40, 55]. According to TG co-pyrolysis studies, the RL % in blends decreased as the biomass quantity increased. [34, 38, 67]. For coal-biomass blends, the TGA bends are exposed in fig2.4. Coal's solid phase is mostly composed of aromatics rings [49]. Biomass decomposes faster than coal. Fig. 2.2 shows that the percent residual mass decreased with an increasing biomass content for blends of coal/biomass indicating that biomass loses more weight than coal. Changing the proportion of biomass in coal-biomass blends can also affect the ignition and peak decomposition temperatures. The blending ratio has the largest influence on other breakdown characteristics, such as weight loss and residue

remaining. When compared to coal, most studies show that biomass results in the highest weight loss.

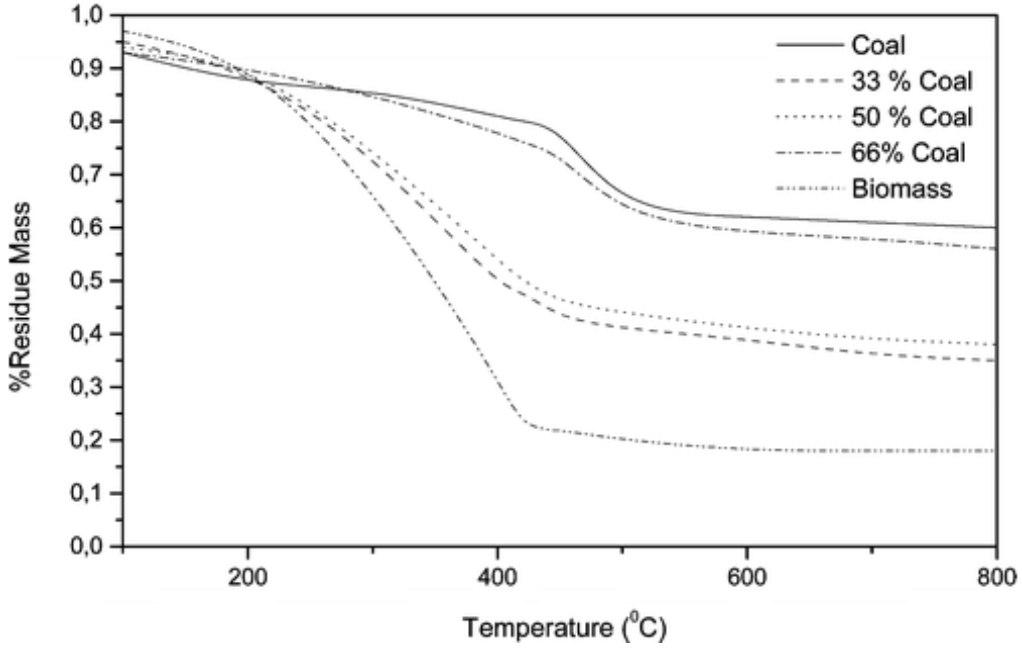

Fig. 2.2 Percent residual mass versus the temperature for raw materials and coal-biomass blends [68]

However, some studies [36, 69] stated that the amount of biomass in the blends did not affect the degree of synergistic effect because biomass has a lower thermal conductivity packing density than coal, increasing the amount of biomass in the blend would slow the heating rate and cause the volatiles from both coal and biomass to take longer to be released [47]. As a result, biomass H and OH radicals are released slowly, enhancing coal tar cracking [31, 35]. Furthermore, biomass char residues formed during co-pyrolysis easily adhere to coal molecules, preventing the volatile material produced by coal pyrolysis from escaping through cracks. Biomass pyrolysis resulted in hydrogen-rich gas [52].

2.4.3 Operating temperature

According to a literature search and prior tests, pyrolysis temperature has a significant influence on the product distribution of coal-biomass blends. [36, 37, 47]. Coal pyrolysis yields predominantly particles with a tiny quantity of gas and liquid, whereas biomass pyrolysis yields solid, gaseous, and liquid compounds. The results of coal-biomass co-pyrolysis are similar to both separate fuels. The synergistic impact, however, caused them to deviate from the predicted amount of product [31]. Char yield reduced and the volatiles yield increased as the temperature increased [47]. As a result, as the temperature rose, so did the conversion of pyrolysis. Many

experts believe that biomass can aid in the devolatilization of coal at low temperatures [70]. The signs of coal-biomass synergy, are largely dependent on the reaction temperature. The synergistic effect mostly happened at 300-500°C, according to Aboyade et al. [46], conforming to the beginning of coal breakdown and end of biomass devolatilization. There is synergy between secondary processes in the blends, according to Ulloa et al. [71], Synergy between coal pyrolysis and sawdust in the production of volatiles is strongest around 400°C. According to Park et al. [47], Synergistic effects result in the formation of extra volatiles in a fixed bed reactor under isothermal conditions between 500°C and 700°C when the biomass ratio is 0.6 at a temperature of 600°C. The optimal temperature for co-pyrolysis of biomass and coal mixtures is 600°C, where significant free radical and hydrogen donors are generated [36]. As a result, the appropriate temperature range for the occurrence of synergy is 400-600°C. Several academics have stated that [31, 47], as the temperature rises to 800°C, the difference between experimental and estimated yields reduces.

2.4.4 Heating Rate

The temperature decomposition for coal and biomass pyrolysis is generally different, and observing synergistic effects is difficult if the heating rate is sluggish [72]. Blend pyrolysis could occur at a high heating rate, resulting in a volatile emission overlap from both coal and biomass [36]. Because the reaction environment contains non-inert species, the yields and products of coal pyrolysis may change at high heating rates [73]. In other words, co-pyrolysis of coal-biomass blends at high heating rates enhanced synergism [37, 60, 74]. When biomass and coal are co-pyrolyzed in an inert atmosphere, they devolatilize together, resulting in a mixed solid char and volatile stream. As a result, the synergistic effect observed during co-pyrolysis may be explained by volatile-char and volatile-volatile interactions [75, 76]. A faster heating rate aided in the production of higher volatile yields [72, 77]. Adopting these parameters increases the potential of gas-phase reactions in biomass and coal volatiles, hence enhancing the intensity of the synergism [71, 78].

2.4.5 The reactor types

Various reactors, including fixed-bed reactors, TGA, drop type high frequency magnetic field-based furnaces, fluidized bed reactors, and free-fall reactors, have been used to study the performance of the co-pyrolysis process [58, 73, 79, 80]. TGA lacks synergistic effects due to the reduced heating rate utilized, which allows the many devolatilization stages

of together fuel in the mixture to be divided. Furthermore, the flow velocity of nitrogen is high enough that volatiles may not remain near the devolatilizing constituents in the vessel. As a result, the main causes for the lack of interactions are attempts to maintain an inactive atmosphere [73]. Many researchers, however, have all challenged this notion, indicating that in TGA, a considerable synergistic impact is detected during coal-biomass blend co-pyrolysis [34, 46, 71]. Table 2.1 represents the summaries of literature work on co-pyrolysis carried out in TGA.

In fixed bed reactors with high sample volumes, close interaction between neighbouring fuel particles and associated volatiles would be conceivable, resulting in a synergistic effect for both gas product compositions and pyrolysis product formation [59, 81, 82]. Close contact between coal and biomass particles during co-pyrolysis, however, does not always imply the presence of interaction [83]. When compared to atmospheric fixed-bed reactors, vacuum pyrolysis and pressurized pyrolysis of coal-biomass blends demonstrated the existence of a synergistic effect [49, 84]. The tube furnaces used for pyrolysis, on the other hand, often include extended high-temperature zones, and the volatiles travels through this zone before exiting from the reactors. It is feasible to increase secondary reactions for char formation and tar cracking by extending the residence time of intraparticle volatiles [85]. As a result, determining whether the synergies in these reactors are mostly attributable to the second volatile reaction or the initial pyrolysis phase is impossible [58].

Many different types of reactors have been built for co-pyrolysis products with high heating rates. According to some studies, fluidized-bed reactors are unsuitable for analyzing interactions because the sample particles are separated in this setting, resulting in a lack of synergistic effect during co-pyrolysis [59]. Xu et al. [40] Researchers tested coal-biomass blends co-pyrolysis in a free-fall reactor and discovered that a higher blending ratio of approximately 70% and a lower temperature of around 600°C are more favourable to synergistic effects. The co-pyrolysis behaviour of coal-biomass blends has been studied using specially designed reactors such as a micro fluidized bed reactor, a single-particle reactor system, and congruent mass TGA [83, 86, 87].

2.5 Kinetic Analysis

2.5.1 Overview

Pyrolysis is an efficient and dependable method for producing bio-oil, charcoal, and gas all in one process. Producer gas is a gaseous fuel that can both power a gas turbine and heat a building. As a result, determining the yields of bioenergy products necessitates a full understanding of the pyrolysis mechanism. As a result, simulating the pyrolysis mechanism is the only way to estimate it. The TGA method examines a sample's mass change as a function of time. Before converting biomass to fuel, a kinetic analysis should be conducted to gain essential information for building pyrolysis reactors and optimizing process parameters [88, 89]. Various feedstocks have different thermal behaviour profiles due to differences in composition [90]. A heterogeneous chemical reaction occurs during the pyrolysis of solid-state materials such as biomass and coal [91].

Interfacial diffusion of reactants and products, changing reaction geometry, and chemical bond breakdown and redistribution are three critical components that can influence the chemical kinetics and reaction dynamics of heterogeneous processes [91]. Concentration, unlike in homogeneous reactions, is a worthless parameter that cannot be used to track the evolution of heterogeneous reaction kinetics because it changes spatially [91-93]. Adsorption, nucleation, interfacial reaction, desorption, and surface or bulk diffusion are examples of heterogeneous reactions that often include a superposition of many primary processes [93]. The initiation step in solid-state decomposition reactions typically involves a "random walk" of vacancies and defects inside the crystal lattice, which results in nucleation growth [94]. In addition, the reaction interface is defined as the border surface between the product and the reactant. This idea is widely used to simulate the kinetics of solid-state reactions [93]. The model-free and model-fitting methods were employed in the non-isothermal kinetics. Therefore, both methods have pros and cons. The combined, can obtain not only the E_a, and A but also find the most probable reaction mechanism [95].

2.5.2 Model-free methods overview

Model-free methods are also a reliable way to calculate the apparent E_a for fixed mass conversions [90]. The model-free methods such as Kissinger Akahira Sunose (KAS) [96] and Flynn Wall Ozawa (FWO) method [97], which assumes that the reaction rate was only

dependent on the reaction temperature for a fixed conversion along with the Friedman method these isoconversional methods were used to calculate the kinetic parameters [98, 99]. To determine more trustworthy kinetic parameters, different heating rates were employed instead of a single heating rate without knowledge of the reaction process. Vyazovkin et al. [100] believe that the kinetic parameters attained by model-free methods are more accurate and consistent [101, 102]. In the starink method, the calculated values of kinetic parameters were found to be more accurate than the KAS and FWO models. The activation energy is estimated using only the degree of conversion and not the reaction technique [103].

Model fitting approaches for non-isothermal TGA data produce very inaccurate kinetic parameter values that can be corrected using isoconversional methods. Several experiments at various heating rates are required to employ these methods. Isoconversional methods are the quickest way to calculate the kinetic parameters of complex reactions with many steps. These methods are sometimes referred to as model-free kinetics analysis. Isoconversional methods estimate activation energy (E_a) as a function of conversion without making any assumptions about the reaction mechanism model. This method is based on the premise that the reaction rate for the constant amount of conversion is only determined by temperature, and that the reaction mechanism model is unaffected by the heating rate. Isoconversional methods define the kinetics of single-step and multi-step processes as defined by the energy of activation (E_a) with the extent of conversion [104]. The apparent activation energy (E_a) calculated using isoconversional methods is regarded as global energy that includes numerous reactions and physical transformations [98, 99]. Table 2.2 presents the most frequent models used in the evaluation of kinetics parameters and discusses the assumption that has been made to perform these models.

Table 2.2 General form of equations for model-free methods [99, 103, 105, 106]

Kinetic models	General equation form	Rules	Plotting variables
Kissinger Akahira Sunose (KAS) method (integral Iso-conversional)	$\ln\left(\frac{\beta}{T^2}\right) = \frac{-E_a}{R}\left(\frac{1}{T}\right) - \ln\left[\left(\frac{E_a}{AR}\right)\int_0^{\alpha}\frac{d\alpha}{f(\alpha)}\right]$	T: temperature At max reaction rate Assumes conversion is fixed.	$\ln\left(\frac{\beta}{T^2}\right)\ vs\ \left(\frac{1}{T}\right)$ and $Slope = E_a$
Flynn Wall Ozawa (FWO) method (integral Iso-conversional)	$\ln\beta = \ln\frac{AE_a}{Rg(\alpha)} - 5.331 - 1.052\frac{E_a}{RT}$	Assumes apparent activation energy remains constant during the degradation and Doyle approximation is applicable for mathematical formulation.	$\log\beta\ vs\ \left(\frac{1}{T}\right)$ and slope = $-0.4567\frac{E_a}{R}$
Friedman method (differential Iso conversional)	$\ln\left(\frac{d\alpha}{dt}\right) = \ln\left[\beta\left(\frac{d\alpha}{dt}\right)\right] = \ln[A\ f(\alpha)\ ] - \frac{E_a}{RT}$	Assumes f(α) remains constant. degradation is independent of temperature and depends only on the rate of mass loss.	$\ln\left(\frac{d\alpha}{dt}\right)\ vs\ \left(\frac{1}{T}\right)$ and $Slope = -\frac{E_a}{R}$
Starink method (integral Iso-conversional)	$\ln\left(\frac{\beta}{T^{1.8}}\right) = -1.0037\ \frac{E_a}{RT} + C_1$	In this method, activation energy is assessed from the slope of the equation at each conversion	$\left(\frac{\beta}{T^{1.8}}\right)\ vs\ \left(\frac{1}{T}\right)$
Vyazovkin method (integral Iso-conversional)	$\sum_{i=1}^{n}\sum_{j\neq 1}^{n}\frac{I(E_{\alpha\alpha},\ T_{\alpha,i})\beta_j}{I(E_{\alpha\alpha},\ T_{\alpha,j})\beta_i} = min$	Assumes g(α) is independent of the heating program and nonlinear regression proposed by Senum and Yang is used.	-

2.5.3 Model-fitting methods overview

A variety of models and methodologies were used to investigate pyrolysis kinetics. The model-fitting method provides useful information on the pyrolysis reaction processes as well as the determination of E_a [107, 108]. Based on calculated kinetic triplets such as E_a, and A and mechanism function, a key technique for investigating the thermal degrading process of biomass is currently widely used [109]. Non-isothermal kinetics strategies offered the benefit of finishing the temperature program faster and easier than isothermal methods [110]. The model-fitting technique, on the other hand, was designed to show the conversion reliance on the reaction rate using a specific reaction mechanism such as diffusion, order-based, or power-law models [93, 111]. The most crucial step in using a mode-fitting approach, such as in Coats Redfern's method [112], was to find an adequate reaction mechanism that describes the degradation of the sample [113]. Model-free methods provide less definitive information than model-fitting methods [101, 102].

2.5.3.1 Coats-Redfern Method

The Coats Redfern method is used to test the validity of model-fitting methods and to offer the best reaction model for biomass breakdown. This model-based technique employs the Arrhenius equation. With considerable effectiveness, the Coats Redfern approach is used to investigate the E_a and A of complex compounds [114, 115]. The most extensively used strategies for determining reaction mechanisms are attained by Coat Redfern methods. Zakrzewski et al. [116] study biomass kinetics in a non-isothermal condition using the coats Redfern method at a heating rate of 5 °C/min, and the E_a and A were determined to be 93.1-174.9 kJ/mol and 4.9104-7.11011/min, respectively. Reina et al. [117] TGA was employed under isothermal conditions to investigate the kinetics of forest wood and ancient furniture, and E_a and A values were found to be in the range of 215.7-127.8 kJ/mol and 1.89107-3.40107 s^{-1}, respectively. Using the Coats Redfern method, B. Nyoni et al. [26] explore the co-pyrolysis kinetics behavior of bituminous coal and microalgae. The coal activation energy was 81.8 kJ/mol in the first stage and 649.3 kJ/mol in the second, whereas microalgae activation energy was 145.5 kJ/mol in the first and second stages, respectively. Coats Redfern technique was used to study co-pyrolysis and co-combustion kinetics on coal-biomass blends by Jian Wang et al. and co-authors [118]. Their results showed that the blending ratio of biomass in the blend affects the E_a and A. In literature, L. F. Madiedo et al. [119] found kinetic parameters (Friedman, KAS, and FWO), and the reaction mechanism for decomposition was discovered

using the Coats Redfern method during co-pyrolysis of coal, terrified sawdust, and paraffin. Hence, the Coats Redfern method has been extensively used in kinetics for solid materials decomposition [120].

2.5.4 Thermodynamic parameters

ΔH, ΔG, and ΔS are essential thermodynamic parameters that can be calculated using kinetics parameters (E_a, A, and peak decomposition temperature T_p) [121]. In reactor design and scaling, thermodynamic parameters are just as important as kinetic characteristics. The thermodynamic parameters validate whether or not a procedure is conceivable. The ΔH represented process endothermic and exothermic behaviour. The ΔH represents the changes in energy in the reagents and activated complex. If the energy barrier is low, complex activation is preferable [122]. Furthermore, higher ΔH values indicate greater structural heat resistance, which could be attributed to a lower level of (positive) synergistic interactions [123]. The ΔG denotes the total energy increase of the system as it approaches chemical equilibrium and the formation of an activated complex [124]. Because the process is not spontaneous, positive ΔG values imply that the system requires external energy. The value of ΔS reflects how near the system is to achieving the thermodynamic equilibrium [123]. The low ΔS value indicates that the substance has experienced some chemical or physical change that has brought it close to thermodynamic equilibrium [125].

The thermodynamics parameter of acai seed biomass during pyrolysis was determined by Vanuza O. Santos et al. [126] who found that the value of ΔH was 154.298 kJ/mol, the value of ΔG was 148.76 kJ/mol, and the value of ΔS was positive. Also, during the sewage sludge- and rice husk co-pyrolysis, S. R. Naqvi et al. [121] also discovered the thermodynamics parameter. The results revealed that the ΔH reaction mechanism exhibited both exothermic and endothermic behavior, and the ΔG was positive for all samples, although the ΔS values were negative for all samples. A study on sewage sludge-HDPE co-pyrolysis was undertaken by A. Zaker et al. [127]. The findings of thermodynamic parameters showed that the ΔH values of a 50 percent sewage sludge mix were 194.56-206.44 kJ/mol and the ΔG values were 119.28-119.54 kJ/mol, showing that bioenergy production is viable.

2.6 Catalytic co-pyrolysis

2.6.1 Catalytic co-pyrolysis overview

Presently, advanced pyrolysis techniques involve numerous approaches, such as catalytic co-pyrolysis. It is a process in which the thermal decomposition of two or three organic materials is carried out at elevated temperatures under the complete absence of oxygen or an inert atmosphere in a temperature range of 300 – 800 °C to produce bio-products such as biochar, bio-oil, and bio-gas in the presence of a catalyst. The catalytic co-pyrolysis technology employs two materials as feedstock and an acidic catalyst for the production of bio-oils [128]. Catalytic upgrading of co-pyrolytic bio-oil resulted in reduced content of oxygenates, enhanced production of aromatics, and conversion of wax species (C_{17}) to lighter HCs [129]. The catalyst breaks down higher molecular compounds into lighter compounds during the process. They aim to improve the selectivity and targeted product yields as well as processing parameters by lowering pyrolysis temperature, and processing time [130, 131]. The effect of catalyst on the pyrolysis process can differ greatly depending on the catalyst used as well as the nature of the parent materials [132].

Several studies have been conducted on catalytic pyrolysis on T. weissflogii and *Pavlova* sp. microalgae using various metals doped alumina supported ceria catalysts to improve the bio-oil yield as compared to the parent material, reducing the Nitrogen, Oxygen content and reducing the formation of coke due to its excellent redox properties [133, 134]. Various comparative studies have been reported between the non-catalytic and catalytic pyrolysis of coconut copra, and rice husk to study the effect of multifunctional catalyst Ni-Ce/Al_2O_3 [135], macroalgae (Ulva prolifera), and douglas fir in TGA and fixed bed reactor with zeolite catalysts showing better bio-oil yield [135-137]. Recently several studies have been conducted on catalytic co-pyrolysis of seaweeds and polypropylene with (Al-SBA-15) [138], and MFI [129] as catalysts producing high-quality bio-oil, reduced water content, and the calorific value nearly equal to that of commercial fuels. Catalytic Co-pyrolysis of Microalgae and Polypropylene using HZSM-5 catalyst was carried out in TGA and bench-scaled fixed bed reactor to promote the efficient production of aromatic hydrocarbons [139]. Several studies have been reported on catalytic co-pyrolysis of numerous biomasses with different plastics with varying compositions, with significantly varying results thus improving the reaction activity, yields, and selectivity of aliphatic hydrocarbons than aromatics [140, 141]. Several investigations related to catalytic co-pyrolysis of biomass with oil shale and

plastics in TGA and Bed reactors have been carried out to study their kinetics, and improve the bio-oil quality, thus promoting the formation of aromatic hydrocarbons over ZSM-5 and CaO catalyst [142-144]. Co-pyrolysis products also have some issues such as oxygenated compounds and water contents to further improve their products and provide stability to them, an alternative up-gradation method is required [128, 135].

Catalytic co-pyrolysis may be regarded as a promising method for the production of high-quality bio-oil. Apart from the co-pyrolysis process conditions such as temperature, particle size, flow rate, heating rate, and feedstock, the type of catalyst used, catalyst loading rate, type of feedstock, and feedstock composition are the major influential factors affecting the product yield and quality during the process.

2.6.2 Catalyst overview for the process

The addition of an acidic catalyst into catalytic co-pyrolysis can deoxygenate bio-oils and enhance the yield and selectivity of hydrocarbon products through catalytic cracking and refineries [128]. Porous ceramics, alkali metals, metal oxides, Ni-based catalysts, zeolite catalysts, or a mixture of different materials all have been developed as catalyst systems for the process and also improve the characteristics of the products [132, 145]. Metal oxides such as CaO, ZnO, ZrO_2, CeO_2, and TiO_2 have been used as catalysts and were effective in decreasing oxygenated compounds, such as phenols, acid, and sugars. The hydrocarbon and aromatic selectivity of these catalysts are very low [146].

Metal-supported catalysts exhibit high activity towards deoxygenation and dehydration. The current catalyst (zeolite and metal-based catalyst) and emerging catalyst (ceria-based catalyst) are broadly applied [132, 146]. CeO_2 gained huge attention in its application for heterogeneous catalysis, due to its diverse configuration thus making them attractive catalysts in the process [132]. CeO_2 has distinctive redox properties that influence the catalyst physio-chemical properties and increase the active metal dispersion over support, further reducing the sintering of active metals [147].

2.6.3 Processes for catalytic co-pyrolysis

They are mixed through dry or wet mixing. Catalytic co-pyrolysis can be divided into two categories based on how the sample is mixed with the catalyst: in-situ and ex-situ catalytic co-pyrolysis process. The catalysts are directly mixed with the blends in the in-situ catalytic

co-pyrolysis process. It requires lower equipment cost and spacing with a simple one-reactor configuration. The in-situ process promotes liquid (e:g naphthalene and higher aromatic compounds) and gas (e:g CO) product generation [131, 148].

On the other hand, in ex-situ, the process occurs in two stages i.e. Primary and secondary stages. In the primary stage, the decomposition of the blends occurs by itself. But in the secondary stage, the pyrolyzed blend products are transported to the catalyst bed which is downstream of the pyrolyzer, where the cracking and the condensation of the volatile products occur [131, 148]. While ex-situ promotes solid (biochar) and gas (monocyclic aromatics) product generation [132].

Summary

The depletion of fossil fuel reserves and damaging emissions must be addressed urgently to save some of their reserves and mitigate climate change. Coal reserves will be available for the next 200 years, yet their emissions cause significant harm. Coal, on the other hand, may be used efficiently through a variety of processing procedures such as pyrolysis, gasification, and so on. To reduce emissions, coal pyrolysis is a viable method for producing synthesis fuels. However, because coal has a low H/C ratio, the product yield is low. Biomass pyrolysis is an appealing alternative to coal since it is a renewable, widely available, and CO_2-neutral organic material. All of these products are sustainable sources of energy, although their calorific value is rather low when compared to coal. Furthermore, bio-oil derived from biomass pyrolysis has significant levels of moisture and oxygenated compounds, which can lead to fouling, slagging, and corrosion.

As a result, coal-biomass co-pyrolysis is a viable alternative because biomass possesses a high hydrogen concentration that will aid in coal pyrolysis. Additionally, coal blending will boost the calorific value of products. Blending coal with biomass helps to save certain coal reserves. However, coal-biomass blends must be characterized to evaluate their co-pyrolysis behaviour. Various characterizations are employed for this drive. The yield of the co-pyrolysis product or the synergistic effect is affected by reaction conditions.

The kinetic analysis aids in determining the best response mechanism for the thermal degradation of coal-biomass mixtures. It will also help with the design and scalability of co-pyrolysis reactors. By modeling multiple integral functions, Coats Redfern's method

approaches the most appropriate response mechanism. In addition, the thermodynamic parameters are generated from the kinetic parameter, which yields the ΔH, ΔG, and ΔS. These characteristics are critical for understanding the co-pyrolysis process.

Catalytic co-pyrolysis is carried out to overcome the issues of co-pyrolysis such as oxygenated compounds and water contents to further improve their products and provide stability to them, it is carried out in TGA, fixed bed reactor, and fluidized bed reactor to check their bioenergy potential and stability. Understanding the kinetics and thermodynamic behavior of catalytic co-pyrolysis is vital to designing, optimizing, and scaling up industrial co-feed conversion applications for reactor design. Porous ceramics, alkali metals, metal oxides, Ni-based catalysts, zeolite catalysts, or a mixture of different materials all have been developed as catalyst systems for the process and also improve the characteristics of the products. Catalytic co-pyrolysis can be divided into two categories based on how the sample is mixed with the catalyst: in-situ and ex-situ catalytic co-pyrolysis process.

References

1. Kammen, D.M., *Renewable Energy, Taxonomic Overview*, in *Encyclopedia of Energy*, C.J. Cleveland, Editor. 2004, Elsevier: New York. p. 385-412.
2. Irfan, M., et al., *Assessing the energy dynamics of Pakistan: prospects of biomass energy.* 2020. **6**: p. 80-93.
3. Kumar, N. and A. Dixit, *Chapter 4 - Management of biomass*, in *Nanotechnology for Rural Development*, N. Kumar and A. Dixit, Editors. 2021, Elsevier. p. 97-140.
4. Mudgil, D., *Chapter 3 - The Interaction Between Insoluble and Soluble Fiber*, in *Dietary Fiber for the Prevention of Cardiovascular Disease*, R.A. Samaan, Editor. 2017, Academic Press. p. 35-59.
5. Calvo-Flores, F.G., *Lignin: A Renewable Raw Material*, in *Encyclopedia of Renewable and Sustainable Materials*, S. Hashmi and I.A. Choudhury, Editors. 2020, Elsevier: Oxford. p. 102-118.
6. Zhao, S.-X., N. Ta, and X.-D. Wang, *Effect of Temperature on the Structural and Physicochemical Properties of Biochar with Apple Tree Branches as Feedstock Material.* Energies, 2017. **10**(9).
7. Chen, D., et al., *Investigation of biomass torrefaction based on three major components: Hemicellulose, cellulose, and lignin.* 2018. **169**: p. 228-237.
8. Hu, X. and M. Gholizadeh, *Biomass pyrolysis: A review of the process development and challenges from initial researches up to the commercialisation stage.* Journal of Energy Chemistry, 2019. **39**: p. 109-143.
9. Oberschelp, C., et al., *Global emission hotspots of coal power generation.* 2019. **2**(2): p. 113-121.
10. Oliveira, M.L., et al., *Multifaceted processes controlling the distribution of hazardous compounds in the spontaneous combustion of coal and the effect of these compounds on human health.* 2018. **160**: p. 562-567.
11. Lozano, R., et al., *Measuring progress from 1990 to 2017 and projecting attainment to 2030 of the health-related Sustainable Development Goals for 195 countries and territories: a systematic analysis for the Global Burden of Disease Study 2017.* 2018. **392**(10159): p. 2091-2138.
12. Wagner, N.J., *Geology of Coal*, in *Encyclopedia of Geology (Second Edition)*, D. Alderton and S.A. Elias, Editors. 2021, Academic Press: Oxford. p. 745-761.
13. Council, W.E.J.W.E.C., London, UK, *World energy resources 2016.* 2016.
14. Agreement, P. *Paris agreement*. in *Report of the Conference of the Parties to the United Nations Framework Convention on Climate Change (21st Session, 2015: Paris). Retrived December*. 2015. HeinOnline.
15. Hendryx, M., et al., *Air pollution emissions 2008–2018 from australian coal mining: Implications for public and occupational health.* 2020. **17**(5): p. 1570.
16. Oliveira, M.L., et al., *Study of coal cleaning rejects by FIB and sample preparation for HR-TEM: mineral surface chemistry and nanoparticle-aggregation control for health studies.* 2018. **188**: p. 662-669.
17. World Health Organization %J World Health Organization: Geneva, S., *WHO global ambient air quality database (update 2018).* 2018.
18. Gasparotto, J. and K. Da Boit Martinello, *Coal as an energy source and its impacts on human health.* Energy Geoscience, 2021. **2**(2): p. 113-120.
19. Zhang, H., S. Fu, and Y.J.I.j.o.b.m. Chen, *Basic understanding of the color distinction of lignin and the proper selection of lignin in color-depended utilizations.* 2020. **147**: p. 607-615.

20. Iglauer, S., et al., *Hydrogen Adsorption on Sub-Bituminous Coal: Implications for Hydrogen Geo-Storage.* 2021. **48**(10): p. e2021GL092976.
21. Xiao, Y., et al., *Influence of element composition and microcrystalline structure on thermal properties of bituminous coal under nitrogen atmosphere.* 2021. **147**: p. 846-856.
22. Liu, J., et al., *Molecular characterization of Henan anthracite coal.* 2019. **33**(7): p. 6215-6225.
23. Miura, K., *Mild conversion of coal for producing valuable chemicals.* Fuel Processing Technology, 2000. **62**(2): p. 119-135.
24. Abnisa, F. and W.M.A. Wan Daud, *A review on co-pyrolysis of biomass: An optional technique to obtain a high-grade pyrolysis oil.* Energy Conversion and Management, 2014. **87**: p. 71-85.
25. Gouws, S.M., et al., *Co-pyrolysis of coal and raw/torrefied biomass: A review on chemistry, kinetics and implementation.* Renewable and Sustainable Energy Reviews, 2021. **135**: p. 110189.
26. Nyoni, B., et al., *Co-pyrolysis of South African bituminous coal and Scenedesmus microalgae: Kinetics and synergistic effects study.* International Journal of Coal Science & Technology, 2020. **7**(4): p. 807-815.
27. Jin, X., et al., *Co-pyrolysis of rice straw and water hyacinth: Characterization of products, yields and biomass interaction effect.* Biomass and Bioenergy, 2019. **127**: p. 105281.
28. Li, S., et al., *Study on co-pyrolysis characteristics of rice straw and Shenfu bituminous coal blends in a fixed bed reactor.* Bioresource technology, 2014. **155C**: p. 252-257.
29. Hassan, H., J.K. Lim, and B.H. Hameed, *Recent progress on biomass co-pyrolysis conversion into high-quality bio-oil.* Bioresource Technology, 2016. **221**: p. 645-655.
30. Vuthaluru, H.B., *Thermal behaviour of coal/biomass blends during co-pyrolysis.* Fuel Processing Technology, 2004. **85**(2): p. 141-155.
31. Sonobe, T., N. Worasuwannarak, and S. Pipatmanomai, *Synergies in co-pyrolysis of Thai lignite and corncob.* Fuel Processing Technology, 2008. **89**(12): p. 1371-1378.
32. Zhang, L., et al., *Influence of woody biomass (cedar chip) addition on the emissions of PM10 from pulverised coal combustion.* Fuel, 2011. **90**(1): p. 77-86.
33. Onay, Ö., E. Bayram, and Ö.M. Koçkar, *Copyrolysis of seyitömer− lignite and safflower seed: influence of the blending ratio and pyrolysis temperature on product yields and oil characterization.* Energy & fuels, 2007. **21**(5): p. 3049-3056.
34. Chen, C., X. Ma, and Y. He, *Co-pyrolysis characteristics of microalgae Chlorella vulgaris and coal through TGA.* Bioresource technology, 2012. **117**: p. 264-273.
35. Shui, H., et al., *Co-liquefaction behavior of a sub-bituminous coal and sawdust.* Energy, 2011. **36**(11): p. 6645-6650.
36. Zhang, L., et al., *Co-pyrolysis of biomass and coal in a free fall reactor.* Fuel, 2007. **86**(3): p. 353-359.
37. Yuan, S., et al., *Rapid co-pyrolysis of rice straw and a bituminous coal in a high-frequency furnace and gasification of the residual char.* Bioresource Technology, 2012. **109**: p. 188-197.
38. Li, S., et al., *Co-pyrolysis characteristic of biomass and bituminous coal.* Bioresource Technology, 2015. **179**: p. 414-420.
39. Li, S., et al., *Co-pyrolysis behaviors of saw dust and Shenfu coal in drop tube furnace and fixed bed reactor.* Bioresource Technology, 2013. **148**: p. 24-29.
40. Quan, C., et al., *Co-pyrolysis of biomass and coal blend by TG and in a free fall reactor.* Journal of Thermal Analysis and Calorimetry, 2014. **117**(2): p. 817-823.

41. Chen, X., et al., *Thermogravimetric analysis and kinetics of the co-pyrolysis of coal blends with corn stalks.* Thermochimica Acta, 2018. **659**: p. 59-65.
42. Tauseef, M., et al., *Thermokinetics synergistic effects on co-pyrolysis of coal and rice husk blends for bioenergy production.* Fuel, 2022. **318**: p. 123685.
43. Gohar, H., et al., *Investigating the characterisation, kinetic mechanism, and thermodynamic behaviour of coal-biomass blends in co-pyrolysis process.* Process Safety and Environmental Protection, 2022. **163**: p. 645-658.
44. Pan, Y.G., E. Velo, and L. Puigjaner, *Pyrolysis of blends of biomass with poor coals.* Fuel, 1996. **75**(4): p. 412-418.
45. Kastanaki, E., et al., *Thermogravimetric studies of the behavior of lignite–biomass blends during devolatilization.* Fuel processing technology, 2002. **77**: p. 159-166.
46. Aboyade, A.O., et al., *Thermogravimetric study of the pyrolysis characteristics and kinetics of coal blends with corn and sugarcane residues.* Fuel Processing Technology, 2013. **106**: p. 310-320.
47. Park, D.K., et al., *Co-pyrolysis characteristics of sawdust and coal blend in TGA and a fixed bed reactor.* Bioresource Technology, 2010. **101**(15): p. 6151-6156.
48. Moghtaderi, B., C. Meesri, and T.F. Wall, *Pyrolytic characteristics of blended coal and woody biomass.* Fuel, 2004. **83**(6): p. 745-750.
49. Aboyade, A.O., et al., *Slow and pressurized co-pyrolysis of coal and agricultural residues.* Energy Conversion and Management, 2013. **65**: p. 198-207.
50. Collard, F.-X. and J. Blin, *A review on pyrolysis of biomass constituents: Mechanisms and composition of the products obtained from the conversion of cellulose, hemicelluloses and lignin.* Renewable and Sustainable Energy Reviews, 2014. **38**: p. 594-608.
51. Lédé, J., *Cellulose pyrolysis kinetics: An historical review on the existence and role of intermediate active cellulose.* Journal of Analytical and Applied Pyrolysis, 2012. **94**: p. 17-32.
52. Quan, C. and N. Gao, *Copyrolysis of biomass and coal: a review of effects of copyrolysis parameters, product properties, and synergistic mechanisms.* BioMed research international, 2016. **2016**.
53. Haykiri-Acma, H. and S. Yaman, *Interaction between biomass and different rank coals during co-pyrolysis.* Renewable Energy, 2010. **35**(1): p. 288-292.
54. Lee, J.-Y., et al., *Comparison of several methods for effective lipid extraction from microalgae.* Bioresource Technology, 2010. **101**(1, Supplement): p. S75-S77.
55. Guo, M. and J.-C. Bi, *Characteristics and application of co-pyrolysis of coal/biomass blends with solid heat carrier.* Fuel Processing Technology, 2015. **138**: p. 743-749.
56. Wu, Z., et al., *Synergistic effect on thermal behavior during co-pyrolysis of lignocellulosic biomass model components blend with bituminous coal.* Bioresource Technology, 2014. **169**: p. 220-228.
57. Blesa, M.J., et al., *Low-temperature co-pyrolysis of a low-rank coal and biomass to prepare smokeless fuel briquettes.* Journal of Analytical and Applied Pyrolysis, 2003. **70**(2): p. 665-677.
58. Jones, J.M., et al., *Devolatilisation characteristics of coal and biomass blends.* Journal of Analytical and Applied Pyrolysis, 2005. **74**(1): p. 502-511.
59. Collot, A.G., et al., *Co-pyrolysis and co-gasification of coal and biomass in bench-scale fixed-bed and fluidised bed reactors.* Fuel, 1999. **78**(6): p. 667-679.
60. Yuan, S., et al., *Nitrogen conversion under rapid pyrolysis of two types of aquatic biomass and corresponding blends with coal.* Bioresource Technology, 2011. **102**(21): p. 10124-10130.

61. Jongwon Kim, S.B.L.C.B.M.B.A.A., *Coliquefaction of Coal and Black Liquor to Environmentally Acceptable Liquid Fuels.* Energy Sources, 1999. **21**(9): p. 839-847.
62. Lalvani, S.B., et al., *Coal liquefaction in lignin-derived liquids under low severity conditions.* Fuel, 1991. **70**(12): p. 1433-1438.
63. Haykiri-Acma, H. and S. Yaman, *Synergy in devolatilization characteristics of lignite and hazelnut shell during co-pyrolysis.* Fuel, 2007. **86**(3): p. 373-380.
64. Suelves, I., M.J. Lázaro, and R. Moliner, *Synergetic effects in the co-pyrolysis of samca coal and a model aliphatic compound studied by analytical pyrolysis.* Journal of Analytical and Applied Pyrolysis, 2002. **65**(2): p. 197-206.
65. Kastanaki, E. and D. Vamvuka, *A comparative reactivity and kinetic study on the combustion of coal–biomass char blends.* Fuel, 2006. **85**(9): p. 1186-1193.
66. Kidena, K., S. Murata, and M. Nomura, *Studies on the Chemical Structural Change during Carbonization Process.* Energy & Fuels, 1996. **10**(3): p. 672-678.
67. Meng, H., et al., *Thermal behavior and the evolution of char structure during co-pyrolysis of platanus wood blends with different rank coals from northern China.* Fuel, 2015. **158**: p. 602-611.
68. Onay, Ö., E. Bayram, and Ö.M. Koçkar, *Copyrolysis of Seyitömer−Lignite and Safflower Seed: Influence of the Blending Ratio and Pyrolysis Temperature on Product Yields and Oil Characterization.* Energy & Fuels, 2007. **21**(5): p. 3049-3056.
69. Aboyade, A.O., et al., *Model fitting kinetic analysis and characterisation of the devolatilization of coal blends with corn and sugarcane residues.* Thermochimica Acta, 2012. **530**: p. 95-106.
70. Yangali, P., A.M. Celaya, and J.L. Goldfarb, *Co-pyrolysis reaction rates and activation energies of West Virginia coal and cherry pit blends.* Journal of Analytical and Applied Pyrolysis, 2014. **108**: p. 203-211.
71. Ulloa, C.A., A.L. Gordon, and X.A. García, *Thermogravimetric study of interactions in the pyrolysis of blends of coal with radiata pine sawdust.* Fuel Processing Technology, 2009. **90**(4): p. 583-590.
72. Meesri, C. and B. Moghtaderi, *Lack of synergetic effects in the pyrolytic characteristics of woody biomass/coal blends under low and high heating rate regimes.* Biomass and Bioenergy, 2002. **23**(1): p. 55-66.
73. Biagini, E., et al., *Devolatilization rate of biomasses and coal–biomass blends: an experimental investigation.* Fuel, 2002. **81**(8): p. 1041-1050.
74. Yuan, S., et al., *HCN and NH3 Released from Biomass and Soybean Cake under Rapid Pyrolysis.* Energy & Fuels, 2010. **24**(11): p. 6166-6171.
75. Weiland, N.T., N.C. Means, and B.D. Morreale, *Product distributions from isothermal co-pyrolysis of coal and biomass.* Fuel, 2012. **94**: p. 563-570.
76. Wang, M., et al., *Interactions between corncob and lignite during temperature-programmed co-pyrolysis.* Fuel, 2015. **142**: p. 102-108.
77. Mohan, D., C.U. Pittman, and P.H. Steele, *Pyrolysis of Wood/Biomass for Bio-oil: A Critical Review.* Energy & Fuels, 2006. **20**(3): p. 848-889.
78. Zhu, W., W. Song, and W. Lin, *Catalytic gasification of char from co-pyrolysis of coal and biomass.* Fuel Processing Technology, 2008. **89**(9): p. 890-896.
79. Kastanaki, E., et al., *Thermogravimetric studies of the behavior of lignite–biomass blends during devolatilization.* Fuel Processing Technology, 2002. **77-78**: p. 159-166.
80. Vamvuka, D., et al., *Pyrolysis characteristics and kinetics of biomass residuals mixtures with lignite☆.* Fuel, 2003. **82**(15): p. 1949-1960.
81. Song, Y., A. Tahmasebi, and J. Yu, *Co-pyrolysis of pine sawdust and lignite in a thermogravimetric analyzer and a fixed-bed reactor.* Bioresource Technology, 2014. **174**: p. 204-211.

82. Fei, J., et al., *Synergistic effects on co-pyrolysis of lignite and high-sulfur swelling coal.* Journal of Analytical and Applied Pyrolysis, 2012. **95**: p. 61-67.
83. Wan, K., et al., *Experimental and modeling study of pyrolysis of coal, biomass and blended coal–biomass particles.* Fuel, 2015. **139**: p. 356-364.
84. Yang, X., et al., *Co-pyrolysis of Chinese lignite and biomass in a vacuum reactor.* Bioresource Technology, 2014. **173**: p. 1-5.
85. Mok, W.S.L. and M.J. Antal, *Effects of pressure on biomass pyrolysis. I. Cellulose pyrolysis products.* Thermochimica Acta, 1983. **68**(2): p. 155-164.
86. Mao, Y., et al., *Fast co-pyrolysis of biomass and lignite in a micro fluidized bed reactor analyzer.* Bioresource Technology, 2015. **181**: p. 155-162.
87. Zhang, Y., et al., *Effect of fuel origin on synergy during co-gasification of biomass and coal in CO2.* Bioresource Technology, 2016. **200**: p. 789-794.
88. Collins, S. and P. Ghodke, *Kinetic parameter evaluation of groundnut shell pyrolysis through use of thermogravimetric analysis.* Journal of environmental chemical engineering, 2018. **6**(4): p. 4736-4742.
89. Ghodke, P. and R.N. Mandapati, *Kinetic modeling of Indian rice husk pyrolysis.* International Journal of Chemical Reactor Engineering, 2018. **16**(2).
90. Mandapati, R.N. and P.K. Ghodke, *Kinetics of pyrolysis of cotton stalk using model-fitting and model-free methods.* Fuel, 2021. **303**: p. 121285.
91. Galwey, A.K. and M.E. Brown, *Kinetic background to thermal analysis and calorimetry*, in *Handbook of thermal analysis and calorimetry*. 1998, Elsevier. p. 147-224.
92. Helsen, L. and E. Van den Bulck, *Kinetics of the low-temperature pyrolysis of chromated copper arsenate-treated wood.* Journal of Analytical and Applied Pyrolysis, 2000. **53**(1): p. 51-79.
93. White, J.E., W.J. Catallo, and B.L. Legendre, *Biomass pyrolysis kinetics: A comparative critical review with relevant agricultural residue case studies.* Journal of Analytical and Applied Pyrolysis, 2011. **91**(1): p. 1-33.
94. Flynn, J.H., *Temperature dependence of the rate of reaction in thermal analysis: the Arrhenius equation in condensed phase kinetics.* Journal of Thermal Analysis and Calorimetry, 1990. **36**(4): p. 1579-1593.
95. Ma, Z., et al., *Comparison of the thermal degradation behaviors and kinetics of palm oil waste under nitrogen and air atmosphere in TGA-FTIR with a complementary use of model-free and model-fitting approaches.* Journal of Analytical and Applied Pyrolysis, 2018. **134**: p. 12-24.
96. Akahira, T. and T. Sunose, *Method of determining activation deterioration constant of electrical insulating materials.* Res Rep Chiba Inst Technol (Sci Technol), 1971. **16**(1971): p. 22-31.
97. Flynn, J.H. and L.A. Wall, *A quick, direct method for the determination of activation energy from thermogravimetric data.* Journal of Polymer Science Part B: Polymer Letters, 1966. **4**(5): p. 323-328.
98. Varma, A.K., et al., *Thermal, kinetic and thermodynamic study for co-pyrolysis of pine needles and styrofoam using thermogravimetric analysis.* Energy, 2021. **218**: p. 119404.
99. Özsin, G., et al., *A thermo-kinetic study on co-pyrolysis of oil shale and polyethylene terephthalate using TGA/FT-IR.* Korean Journal of Chemical Engineering, 2020. **37**(11): p. 1888-1898.
100. Vyazovkin, S., et al., *ICTAC Kinetics Committee recommendations for performing kinetic computations on thermal analysis data.* Thermochimica acta, 2011. **520**(1-2): p. 1-19.

101. Soria-Verdugo, A., et al., *Comparison of wood pyrolysis kinetic data derived from thermogravimetric experiments by model-fitting and model-free methods.* Energy Conversion and Management, 2020. **212**: p. 112818.
102. Li, B., et al., *Study of combustion behaviour and kinetics modelling of Chinese Gongwusu coal gangue: Model-fitting and model-free approaches.* Fuel, 2020. **268**: p. 117284.
103. Parthasarathy, P., et al., *Thermal degradation characteristics and gasification kinetics of camel manure using thermogravimetric analysis.* Journal of Environmental Management, 2021. **287**: p. 112345.
104. Wen, Y., et al., *Synergistic effect of the co-pyrolysis of cardboard and polyethylene: A kinetic and thermodynamic study.* Energy, 2021. **229**: p. 120693.
105. Çepelioğullar, Ö., H. Haykırı-Açma, and S. Yaman, *Kinetic modelling of RDF pyrolysis: Model-fitting and model-free approaches.* Waste Management, 2016. **48**: p. 275-284.
106. Singh, S., et al., *Insights into kinetic and thermodynamic analyses of co-pyrolysis of wheat straw and plastic waste via thermogravimetric analysis.* Bioresource Technology, 2022. **356**: p. 127332.
107. Gupta, A., S.K. Thengane, and S. Mahajani, *Kinetics of pyrolysis and gasification of cotton stalk in the central parts of India.* Fuel, 2020. **263**: p. 116752.
108. Ghodke, P. and R.N. Mandapati, *Investigation of particle level kinetic modeling for babul wood pyrolysis.* Fuel, 2019. **236**: p. 1008-1017.
109. Anca-Couce, A., *Reaction mechanisms and multi-scale modelling of lignocellulosic biomass pyrolysis.* Progress in Energy and Combustion Science, 2016. **53**: p. 41-79.
110. Vyazovkin, S., *Modification of the integral isoconversional method to account for variation in the activation energy.* Journal of Computational Chemistry, 2001. **22**(2): p. 178-183.
111. Hu, Z., et al., *Characteristics and kinetic studies of Hydrilla verticillata pyrolysis via thermogravimetric analysis.* Bioresource Technology, 2015. **194**: p. 364-372.
112. Coats, A.W. and J.P. Redfern, *Kinetic parameters from thermogravimetric data.* Nature, 1964. **201**(4914): p. 68-69.
113. Maurya, R., et al., *Non-isothermal pyrolysis of de-oiled microalgal biomass: kinetics and evolved gas analysis.* Bioresource technology, 2016. **221**: p. 251-261.
114. Hu, J., et al., *Effectiveness of wind turbine blades waste combined with the sewage sludge for enriched carbon preparation through the co-pyrolysis processes.* Journal of Cleaner Production, 2018. **174**: p. 780-787.
115. Jayaraman, K., M.V. Kok, and I. Gokalp, *Thermogravimetric and mass spectrometric (TG-MS) analysis and kinetics of coal-biomass blends.* Renewable Energy, 2017. **101**: p. 293-300.
116. Zakrzewski, R., *Pyrolysis kinetics of wood comparison of iso and polythermal thermogravimetric methods.* Electronic Journal of Polish Agricultural Universities, 2003. **6**(2).
117. Reina, J., E. Velo, and L. Puigjaner, *Thermogravimetric study of the pyrolysis of waste wood.* Thermochimica acta, 1998. **320**(1-2): p. 161-167.
118. Wang, J., et al., *Thermal Behaviors and Kinetics of Pingshuo Coal/Biomass Blends during Copyrolysis and Cocombustion.* Energy & Fuels, 2012. **26**(12): p. 7120-7126.
119. Florentino-Madiedo, L., et al., *Evaluation of synergy during co-pyrolysis of torrefied sawdust, coal and paraffin. A kinetic and thermodynamic study.* Fuel, 2021. **292**: p. 120305.
120. Masnadi, M.S., et al., *Fuel characterization and co-pyrolysis kinetics of biomass and fossil fuels.* Fuel, 2014. **117**: p. 1204-1214.

121. Naqvi, S.R., et al., *Synergistic effect on co-pyrolysis of rice husk and sewage sludge by thermal behavior, kinetics, thermodynamic parameters and artificial neural network.* Waste Management, 2019. **85**: p. 131-140.
122. Özsin, G. and A.E. Pütün, *Co-pyrolytic behaviors of biomass and polystyrene: Kinetics, thermodynamics and evolved gas analysis.* Korean Journal of Chemical Engineering, 2018. **35**(2): p. 428-437.
123. Muigai, H.H., et al., *Co–pyrolysis of biomass blends: Characterization, kinetic and thermodynamic analysis.* Biomass and Bioenergy, 2020. **143**: p. 105839.
124. Turmanova, S.C., et al., *Non-isothermal degradation kinetics of filled with rise husk ash polypropene composites.* Express Polym Lett, 2008. **2**(2): p. 133-146.
125. Xu, Y. and B. Chen, *Investigation of thermodynamic parameters in the pyrolysis conversion of biomass and manure to biochars using thermogravimetric analysis.* Bioresource technology, 2013. **146**: p. 485-493.
126. Santos, V.O., et al., *Pyrolysis of acai seed biomass: Kinetics and thermodynamic parameters using thermogravimetric analysis.* Bioresource Technology Reports, 2020. **12**: p. 100553.
127. Zaker, A., et al., *Co-pyrolysis of sewage sludge and low-density polyethylene – A thermogravimetric study of thermo-kinetics and thermodynamic parameters.* Journal of Environmental Chemical Engineering, 2021. **9**(1): p. 104554.
128. Hassan, H., J.K. Lim, and B.H. Hameed, *Recent progress on biomass co-pyrolysis conversion into high-quality bio-oil.* Bioresour Technol, 2016. **221**: p. 645-655.
129. Kim, Y.-M., et al., *Catalytic co-pyrolysis of polypropylene and Laminaria japonica over zeolitic materials.* International Journal of Hydrogen Energy, 2017. **42**(29): p. 18434-18441.
130. Lee, X.J., et al., *State of art review on conventional and advanced pyrolysis of macroalgae and microalgae for biochar, bio-oil and bio-syngas production.* Energy Conversion and Management, 2020. **210**: p. 112707.
131. Shafaghat, H., et al., *In-situ and ex-situ catalytic pyrolysis/co-pyrolysis of empty fruit bunches using mesostructured aluminosilicate catalysts.* Chemical Engineering Journal, 2019. **366**.
132. Lee, J., E.E. Kwon, and Y.-K. Park, *Recent advances in the catalytic pyrolysis of microalgae.* Catalysis Today, 2020. **355**: p. 263-271.
133. Aysu, T., J. Fermoso, and A. Sanna, *Ceria on alumina support for catalytic pyrolysis of Pavlova sp. microalgae to high-quality bio-oils.* Journal of energy chemistry, 2018. **27**(3): p. 874-882.
134. Aysu, T., M.M. Maroto-Valer, and A. Sanna, *Ceria promoted deoxygenation and denitrogenation of Thalassiosira weissflogii and its model compounds by catalytic in-situ pyrolysis.* Bioresource technology, 2016. **208**: p. 140-148.
135. Balasundram, V., et al., *Thermogravimetric catalytic pyrolysis and kinetic studies of coconut copra and rice husk for possible maximum production of pyrolysis oil.* Journal of Cleaner Production, 2017. **167**: p. 218-228.
136. Ma, C., et al., *Non-catalytic and catalytic pyrolysis of Ulva prolifera macroalgae for production of quality bio-oil.* Journal of the Energy Institute, 2020. **93**(1): p. 303-311.
137. Wang, L., et al., *Thermal decomposition behavior and kinetics for pyrolysis and catalytic pyrolysis of Douglas fir.* RSC advances, 2018. **8**(4): p. 2196-2202.
138. Lee, H.W., et al., *Pyrolysis and co-pyrolysis of Laminaria japonica and polypropylene over mesoporous Al-SBA-15 catalyst.* Nanoscale research letters, 2014. **9**(1): p. 1-8.
139. Qi, P., et al., *Production of aromatic hydrocarbons by catalytic co-pyrolysis of microalgae and polypropylene using HZSM-5.* Journal of Analytical and Applied Pyrolysis, 2018. **136**: p. 178-185.

140. Rahman, M.H., et al., *Thermo-catalytic co-pyrolysis of biomass and high-density polyethylene for improving the yield and quality of pyrolysis liquid.* Energy, 2021. **225**: p. 120231.
141. Xu, S., et al., *Synergistic effects of catalytic co-pyrolysis of macroalgae with waste plastics.* Process Safety and Environmental Protection, 2020. **137**: p. 34-48.
142. Zhang, X., et al., *Thermal behavior and kinetic study for catalytic co-pyrolysis of biomass with plastics.* Bioresource technology, 2016. **220**: p. 233-238.
143. Zheng, Y., et al., *Insights into pyrolysis and catalytic co-pyrolysis upgrading of biomass and waste rubber seed oil to promote the formation of aromatics hydrocarbon.* International Journal of Hydrogen Energy, 2018. **43**(34): p. 16479-16496.
144. Dai, M., et al., *Behaviors, product characteristics and kinetics of catalytic co-pyrolysis spirulina and oil shale.* Energy conversion and Management, 2019. **192**: p. 1-10.
145. Wang, Y., et al., *Hydrogen-rich syngas production from biomass pyrolysis and catalytic reforming using biochar-based catalysts.* Fuel, 2022. **313**: p. 123006.
146. Bhoi, P., et al., *Recent advances on catalysts for improving hydrocarbon compounds in bio-oil of biomass catalytic pyrolysis.* Renewable and Sustainable Energy Reviews, 2020. **121**: p. 109676.
147. Raza, J., et al., *Methane decomposition for hydrogen production over biomass fly ash-based CeO2 nanowires promoted cobalt catalyst.* Journal of Environmental Chemical Engineering, 2021. **9**(5): p. 105816.
148. Das, P., et al., *Recent advances in thermochemical methods for the conversion of algal biomass to energy.* Science of The Total Environment, 2021. **766**: p. 144608.

Chapter 3 Material and Methods

3.1 Materials Preparation

In this study, 100% Bituminous Coal (100%BC) was collected from D.G. Cement, Dera ghazi khan, and 100% Algae Consortium (100%AC) were collected locally from wastewater pond in Bajaur agency. 100%BC and 100%AC samples were dried in an oven in the presence of air at 105°C for about 12-24 h to remove moisture before use. The samples were then crushed using the hammer to a size where it is easy to grind. Furthermore, both materials were grounded in a Hard Grove Grindability Index Tester (USA) which was then followed by sieving using a laboratory test sieve WS Tyler RX-29-10 (USA) having obtained a fine particle size of 0.2 mm. Then the Sieved 100%BC and 100%AC were poured into the plastic bag for further use as illustrated in Fig. 3.1. The weight of the 100%BC and 100%AC samples prepared is 10 grams.

The blends of 100% Bituminous Coal (100%BC) and 100% Algae Consortium (100%AC) were prepared on weight basis of 80%Bituminous Coal-20%Algae Consortium (80BC-20AC), 60%Bituminous Coal-40%Algae Consortium (60BC-40AC), 40%Bituminous Coal-60%Algae Consortium (40BC-60AC), 20%Bituminous Coal-80%Algae Consortium (20BC-80AC). The four (BC-AC) Blends were weighted by using the Digital GSM Balance to ensure the blending accuracy in (BC-AC) blends as shown in Fig. 3.1. Then the four blended samples were homogenized using a vortex mixer. The blended samples were put in a vial for mixing and were mixed using a Vortex mixer (F20220176, VELP SCIENTIFICA, EUROPE) for about 5 minutes [1, 2]. The weight of the blended samples prepared is 8 grams each.

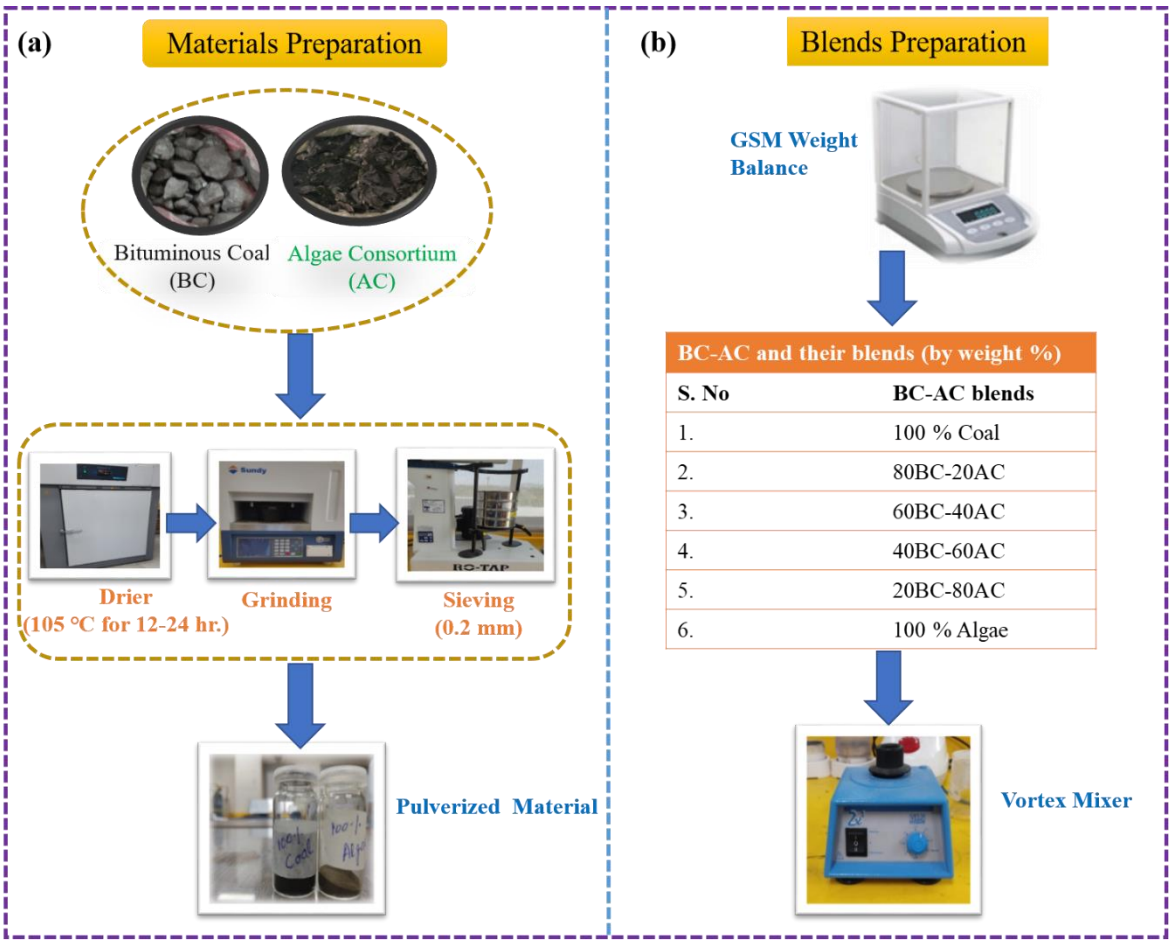

Fig. 3.1 Pure and Blend Samples Preparation (a) Material preparation (b) Blends preparation

3.1.1 Catalyst Synthesis

The 10%CeO_2@MNA synthesis method is reported elsewhere [3]. Briefly, the MNA is synthesized co-precipitation method using nitrate solutions. While the CeO_2 is prepared using the modified hydrothermal method as reported in [4]. Furthermore, the 10%CeO_2@MNA is prepared using the wetness impregnation method. The catalyst dried and calcined at 850 °C before being applied in catalytic co-pyrolysis.

3.1.2 Catalytic co-pyrolysis sample preparation

For the catalytic co-pyrolysis, the sample was prepared using the in-situ method, in which the catalyst was mixed with the optimum blend directly. The catalyst CeO_2@MNA was mixed with the optimum blend of 100%BC and 100%AC directly and was ground using hand-mortar. They were mixed in two different proportions of 3wt.% and 5wt.% of a CeO_2@MNA catalyst with the optimum blend of 100%BC and 100%AC to make a 1 g sample each. Then the new blend for the catalytic co-pyrolysis was prepared at catalyst mass loading and the

optimum blend loading ratio was referred to as, 0wt.% (0.00:1.00), 3wt.% (0.03:0.97), and 5 wt.% (0.05:0.95) respectively [5]. The samples were weighed using a Digital GSM Balance to ensure the blending accuracy, then the samples were put into the vial and mixed using a Vortex mixer (F20220176, VELP SCIENTIFICA, EUROPE) for about 5 minutes.

3.2 Materials Characterization

The ultimate analysis is carried out using CHN Analyzer (5ECHN2200, CKIC, China) to analyze the percentage of C, H, and N in 100%BC, 100%AC, and their four (BC-AC) blends by comparing them with the standard values. Sulfur Analyzer 5E-IRS II (CKIC, China) was used to determine the S content in pure 100%BC, 100%AC, and their four (BC-AC) blends. For ultimate analysis, each sample is weighing 80 mg with a particle size of 0.2 mm. A weight of 300 mg is taken with a particle size of 0.2 mm for the Sulfur analyzer.

The gross calorific value (GCV) of 100%BC, 100%AC, and their four (BC-AC) blends were also obtained from the analysis through a Parr 6200 oxygen bomb calorimeter by following the standard procedure (ASTM D5865-13). The weight of each sample taken for finding GCV is 1 gram.

FTIR was performed using Cary 630 (Agilent Technologies, USA) to analyze the functional groups in 100%BC, 100%AC, and their four (BC-AC) Blends. The absorption of infrared spectra ranging from 4000 to 650 cm^{-1} with a resolution of 2 cm^{-1} was scanned. The measurements were done by employing the Diamond ATR module. The weight of the sample taken is 0.4 grams.

Thermal stability of the 100%BC, 100%AC, and their four (BC-AC) Blends was performed on thermo-gravimetric analysis (TGA) 5500 (TA Instruments, USA). The experiments were performed in an inert atmosphere i.e. Nitrogen (N_2) gas, having a flow rate of 50 mL min^{-1}. Then the samples were heated from an ambient temperature of 25 °C to 900 °C with a heating rate of 10 °C/min. The weight of each of the six samples taken for TGA/DTG analysis was 10 mg with a particle size of 0.2 mm using a platinum pan. Before experimenting, each sample was purged at N_2 for 30 min having a flow rate of 50 mL min^{-1}.

3.3 Synergistic effect analysis

The experimentally derived parameters from TGA/DTG should be compared to the calculated ones to explore the synergistic effect in the four (BC-AC) blends. The synergistic effect is used to assess how 100%BC and 100%AC biomass interact during co-pyrolysis. For positive synergistic effects, the value is greater than zero, which indicates the promoting effect of co-pyrolysis and for negative synergistic effects a value less than zero would be noticed and indicates the inhibiting effect of co-pyrolysis, therefore the experimental value will be greater than the calculated values [6, 7]. During co-processing, the additive model assumed that there are no interactions observed so that the calculated values are the sum of the values of individual samples proportional to their blending weight ratio [8]. An equation has been derived to find the calculated values of the BC-AC blends as given in Eq. 3.1:

$$Y_C = X_{c.m.r}(Y_{exp.C}) + X_{b.m.r}(Y_{exp.B}) \quad (3.1)$$

Where $X_{c.m.r}$ and $X_{b.m.r}$ represents the mass ratio of 100%BC and 100%AC biomass in mixture samples respectively. $Y_{exp.C}$ And $Y_{exp.B}$ represents the experimental results of 100%BC and 100%AC biomass.

The deviation between the experimental and calculated values of weight loss (WL%), the residue left (RL%), and ($(DTG)_{max}$ %) was determined by using an equation given below in Eq. 3.2 will highlight the presence or absence of synergistic effects in the four (BC-AC) blends during co-pyrolysis. The positive value of the synergistic effect indicates its existence, whereas the negative value indicates no synergistic effect [9].

$$\text{Deviation (\%)} = \frac{Y_E - Y_C}{Y_C} \times 100 \quad (3.2)$$

Where Y_E denotes the experimental values obtained during TGA/DTG analysis while Y_C denotes the calculated values found through Eq. 3.1. The greater the deviation between theoretical and experimental values, the significantly larger the synergistic effects [10].

3.4 Kinetic Models

To first understand the mechanism of kinetics, a kinetic equation of a solid-state reaction is formulated which is then solved using non-linear optimization to get effective kinetic parameters i.e. Activation Energy (E_a), Pre-exponential factor (A), Linear Regression

(R^2). Kinetic analysis of 100%BC, 100%AC, and the four (BC-AC) blends are done by the non-isothermal Coats-Redfern integral method. Almost eighteen reaction models as mentioned in Table 3.1, are used to establish the kinetic parameters of the co-pyrolysis process. It is a significant method because in this model the exact reaction mechanism is not required [11]. This method was applied to the TGA in this study to obtain the total volatile release kinetics for co-pyrolysis [12]. To calculate the E_a and A more precisely, the decomposition of 100%BC, and 100%AC was explained in a single stage namely the first stage. While the four blends were divided into two stages [13]. Moisture content stages were not included in the calculation of kinetics parameters.

3.4.1 Theory

The conversion of 100%BC, 100%AC, and their four (BC-AC) blends into products through co-pyrolysis is an important process. The study of pyrolytic kinetics is useful in designing, operating, and optimizing the process [14]. The thermal degradation of 100%BC, 100%AC, and their four blends can be described by a single reaction as Eq. 3.3:

$$A \rightarrow B + C \tag{3.3}$$

Where A = BC, AC and blends, B = Biochar and C = volatile matter. The rate equation of a solid-state reaction can be described by Eq. 3.4:

$$\frac{d\alpha}{dt} = k(T) \cdot f(\alpha) \tag{3.4}$$

Where α represents the conversion rate whose value is in the range of (0-1), k (T) is the rate constant and f(α) is the reaction mechanism. During the TG experiment, the mass of the sample is continuously measured as a function of temperature and time. The fraction of material converted (α) at any time (t) during co-pyrolysis into volatile components can be determined by Eq. 3.5, calculated with mass range:

$$\alpha = \frac{m_i - m_{ins}}{m_i - m_f} \tag{3.5}$$

Where m_o is the initial mass of the sample before undergoing decomposition (kg), m_{ins} is the instantaneous mass of the sample at time t (kg), and m_f is the final mass of the sample after decomposition (kg). Eq. 3.6 represents the heating rate equation, where β represents the heating rate, while dT is the derivative of temperature while dt represents the derivative of time.

$$\beta = \frac{dT}{dt} \tag{3.6}$$

Furthermore, the rate constant k can be calculated by the Arrhenius equation as shown in Eq. 3.7:

$$k(T) = A \cdot \exp\left(-\frac{E_a}{RT}\right) \quad (3.7)$$

Where A is the pre-exponential factor (min^{-1}) in the Arrhenius equation; R is the universal gas constant (*8.314 J.K^{-1}.mol^{-1}*), E_a is the activation energy (kJ/mol) and T is the absolute temperature (K). The differential of conversion with respect to time is known as the rate of a reaction [14]. Incorporating Eq. 3.7 in Eq. 3.4, under a constant heating rate β, temperature dependence from Arrhenius law, the fundamental Arrhenius rate expression can be rearranged to in the form of Eq. 3.8:

$$\frac{d\alpha}{dt} = A \cdot \exp\left(-\frac{E_a}{RT}\right) \cdot f(\alpha) \quad (3.8)$$

For a constant heating rate, by incorporating Eq. 3.6 in Eq. 3.8, it can be rearranged in the form of Eq. 3.9:

$$\frac{d\alpha}{dT} = \frac{A}{\beta} \cdot \exp\left(-\frac{E_a}{RT}\right) \cdot f(\alpha) \quad (3.9)$$

The model $f(\alpha)$ used here is expressed as in Eq. 3.10, where n is the order of the reaction.

$$f(\alpha) = (1-\alpha)^n \quad (3.10)$$

In many applications, it is thought that the pyrolysis of fuels is a first-order reaction (n = 1) that is exclusively related to decomposition reactions. Assuming n = 1, Eq. 3.10 can be rearranged under a constant heating rate β to give Eq. 3.11:

$$\frac{d\alpha}{dT} = \frac{A}{\beta} \cdot \exp\left(-\frac{E_a}{RT}\right) \cdot (1-\alpha) \quad (3.11)$$

Integrating the above equation, we obtain the following form as in Eq. 3.12:

$$g(\alpha) = \int_0^\alpha \frac{d\alpha}{f(\alpha)} = \frac{A}{\beta}\int_{T_0}^{T} exp\left(-\frac{E_a}{RT}\right) dT \quad (3.12)$$

$g(\alpha)$ represents the integrated form of the reaction model in Eq. 3.4.

Coats-Redfern is a model-fitting method that is a traditional kinetic analysis method. This model is extensively used for kinetic investigation of coal and biomass [15], thus, accurately describing the entire decomposition process of a sample assuming it as a single, self-contained reaction with first-order kinetics. The model's advantage is that it may be used to estimate the kinetic parameters of a decomposition process even when only one heating rate is used. The

Coats-Redfern integral method in Eq. 3.11 uses a Taylor series expansion to yield the following expression in Eq. 3.13:

$$ln\left[\frac{g(\alpha)}{T^2}\right] = ln\left[\frac{AR}{\beta E_a}\left(1 - \frac{2RT}{E_a}\right)\right] - \frac{E_a}{RT} \quad (3.13)$$

For a first-order reaction $f(\alpha) = (1-\alpha)$ and $g(\alpha) = -\ln(1-\alpha)$ as shown in Eq. 3.14 and the equation for a second-order reaction is given in Eq. 3.15 respectively [15, 16].

$$ln\left[\frac{-\ln(1-\alpha)}{T^2}\right] = ln\left[\frac{AR}{\beta E_a}\left(1 - \frac{2RT}{E_a}\right)\right] - \frac{E_a}{RT} \quad (3.14)$$

$$ln\left[\frac{(1-\alpha)^{-1}-1}{T^2}\right] = ln\left[\frac{AR}{\beta E_a}\left(1 - \frac{2RT}{E_a}\right)\right] - \frac{E_a}{RT} \quad (3.15)$$

Where $\left(1 - \frac{2RT}{E_a}\right)$ is assumed to be small and can be neglected from Eq. 3.13. Hence, it can be written as presented in Eq. 3.16;

$$ln\left[\frac{g(\alpha)}{T^2}\right] = ln\left[\frac{AR}{\beta E_a}\right] - \frac{E_a}{RT} \quad (3.16)$$

The E_a and A represent activation energy and pre-exponential factor respectively, which can be obtained from the slope of the line and A can be obtained from its intercept by sketching a graphical curve drawn between $ln\left[\frac{-\ln(1-\alpha)}{T^2}\right]$ and $\frac{1}{T}$. For n = 1 this plot becomes a linear line [17]. Eq. 3.16 is of the form given below in Eq. 3.17:

$$y = mx + c \quad (3.17)$$

The parameters y, x indicate (Y-axis), (X-axis), while m, c indicate (slope) and (intercept) in Eq. 3.17. These are defined in Eq. (3.18-3.22) [5, 10].

$$y = ln\left[\frac{g(\alpha)}{T^2}\right] \quad (3.18)$$

$$x = \frac{1}{T} \quad (3.19)$$

$$m = \frac{E_a}{R} \quad (3.20)$$

$$c = ln\left[\frac{AR}{\beta E_a}\right] \quad (3.21)$$

For the calculation of the pre-exponential factor, Eq. 3.21 can be simplified to the following Eq. 3.22:

$$A = \frac{\exp(c)\,\beta E_a}{R} \qquad (3.22)$$

Table 3.1 represents $f(\alpha)$ and $g(\alpha)$ of common reaction models used in the Coats-Redfern integral method [11, 18-20]. $g(\alpha)$ with the highest R^2 will be considered as the most fitting model that best describes the data of reaction kinetics of weight loss at a specific stage.

Table 3.1 Represents the algebraic expression of the commonly used reaction models

Reaction Model	**Symbols**	**Reaction Mechanism**	**Differential form** $f(\alpha) = \frac{1}{k}\frac{d\alpha}{dt}$	**Integral form** $g(\alpha) = kt$
Reaction Order Models	F1/3	One-third order	$(1-\alpha)^{\frac{1}{3}}$	$-\frac{3}{2}\left[(1-\alpha)^{\frac{2}{3}}-1\right]$
	F1	First-order	$(1-\alpha)$	$-\ln(1-\alpha)$
	F3/2	One and a half order	$(1-\alpha)^{\frac{3}{2}}$	$2\left[(1-\alpha)^{-\frac{1}{2}}-1\right]$
	F2	Second-order	$(1-\alpha)^2$	$(1-\alpha)^{-1}-1$
	F3	Third-order	$(1-\alpha)^3$	$\frac{1}{2}[(1-\alpha)^{-2}-1]$
	F4	Fourth-order	$(1-\alpha)^4$	$\frac{1}{4}[(1-\alpha)^{-3}-1]$
Geometric Contraction Models	R1	Contracting disk	1	α
	R2	Contracting cylinder	$2(1-\alpha)^{\frac{1}{2}}$	$1-(1-\alpha)^{\frac{1}{2}}$
	R3	Contracting sphere	$3(1-\alpha)^{\frac{2}{3}}$	$1-(1-\alpha)^{\frac{1}{3}}$
Power Law	P2	Power law; P2	$2(\alpha)^{\frac{1}{2}}$	$(\alpha)^{\frac{1}{2}}$
	P3	Power law; P3	$3(\alpha)^{\frac{2}{3}}$	$(\alpha)^{\frac{1}{3}}$
	P4	Power law; P4	$4(\alpha)^{\frac{3}{4}}$	$(\alpha)^{\frac{1}{4}}$
Diffusivity Models	D1	Parabolic law	$\frac{1}{2}\alpha$	α^2
	D2	Valansi equation	$-[\ln(1-\alpha)]^{-1}$	$\alpha+[(1-\alpha)\ln(1-\alpha)]$
	D3	Jander equation	$2(1-\alpha)^{\frac{2}{3}}\left[1-(1-\alpha)^{\frac{1}{3}}\right]^{-1}$	$\left[1-(1-\alpha)^{\frac{1}{3}}\right]^2$
	D4	Ginstling Brounstein equation	$\frac{3}{2}\left[(1-\alpha)^{-\frac{1}{3}}-1\right]^{-1}$	$1-\frac{2}{3}\alpha-(1-\alpha)^{\frac{2}{3}}$
Nucleation Models	A2	Avarami-Erofe'ev for n = 2	$2(1-\alpha)[-\ln(1-\alpha)]^{\frac{1}{2}}$	$[-\ln(1-\alpha)]^{\frac{1}{2}}$
	A3	Avarami-Erofe'ev for n = 3	$3(1-\alpha)[-\ln(1-\alpha)]^{\frac{1}{3}}$	$[-\ln(1-\alpha)]^{\frac{1}{3}}$

3.4.2 Thermodynamic Parameters

The quantity of heat transmitted during a chemical reaction under isobaric conditions is called enthalpy. ΔH (kJ/mol) stands for the change in enthalpy of a system. The quantity of heat energy transmitted during a chemical reaction is measured by entropy, which is commonly referred to as a measure of randomness. The change in entropy is expressed as ΔS (kJ/mol K). Gibbs free energy is the maximum quantity of work that a closed system can produce. In a completely reversible process, this maximum work can be achieved. . The ΔG (kJ/mol), or change in Gibbs free energy, is a measurement of a system's energy content that can be used to analyze energy generation [21]. From the values of kinetic parameters, the thermodynamic properties such as Gibbs free energy (ΔG), enthalpy (ΔH), and entropy (ΔS) can be determined. The values of the thermodynamic properties are estimated using Eq. 3.23 and Eq. 3.24 given below [22]:

$$\Delta H = E_a - R \cdot T_p \tag{3.23}$$

$$\Delta G = E_a + R \cdot T_p \ \ln\left(\frac{k_b T_p}{hA}\right) \tag{3.24}$$

Where k_b denotes the Boltzmann constant (1.38×10^{-23} J/K), R is the universal gas constant, h represents the Planck constant (6.63×10^{-34} Js) and T_p is the DTG peak decomposition temperature, in kelvin K. The entropy is determined using Eq. (3.25):

$$\Delta S = \frac{\Delta H - \Delta G}{T_p} \tag{3.25}$$

The values of ΔG, ΔH, and ΔS were determined from the values of the activation energy obtained through kinetic parameters from the analysis of the Coats-Redfern integral method.

3.5 Catalytic co-pyrolysis

The catalytic co-pyrolysis of the optimum blend over the catalyst was performed using a TGA 5500 (TA Instruments, USA). The samples were loaded into a platinum crucible pan and heated from 25 – 900 °C in an inert atmosphere at a constant heating rate of 20 °C/min with a nitrogen flow rate of 40 mL min^{-1}. The weight of the sample loaded was 10 mg. Before experimenting, each sample was purged at N_2 for 30 minutes having a flow rate of 50 mL min^{-1}.

References

1. Gohar, H., et al., *Investigating the characterisation, kinetic mechanism, and thermodynamic behaviour of coal-biomass blends in co-pyrolysis process.* Process Safety and Environmental Protection, 2022. **163**: p. 645-658.
2. Tauseef, M., et al., *Thermokinetics synergistic effects on co-pyrolysis of coal and rice husk blends for bioenergy production.* Fuel, 2022. **318**: p. 123685.
3. Raza, J., et al., *Methane decomposition for hydrogen production over biomass fly ash-based CeO2 nanowires promoted cobalt catalyst.* Journal of Environmental Chemical Engineering, 2021. **9**(5): p. 105816.
4. Ul Hasnain, M.A., et al., *Partial oxidation of methane over CeO2 loaded hydrotalcite (MgNiAl) catalyst for the production of hydrogen rich syngas (H2, CO).* International Journal of Hydrogen Energy, 2021. **46**(74): p. 36663-36677.
5. Balasundram, V., et al., *Thermogravimetric catalytic pyrolysis and kinetic studies of coconut copra and rice husk for possible maximum production of pyrolysis oil.* Journal of Cleaner Production, 2017. **167**: p. 218-228.
6. Wu, Z., et al., *Synergistic effects from co-pyrolysis of low-rank coal and model components of microalgae biomass.* Energy Conversion and Management, 2017. **135**: p. 212-225.
7. Wu, Z., et al., *Synergistic effects from co-pyrolysis of lignocellulosic biomass main component with low-rank coal: Online and offline analysis on products distribution and kinetic characteristics.* Applied Energy, 2020. **276**: p. 115461.
8. Park, D.K., et al., *Co-pyrolysis characteristics of sawdust and coal blend in TGA and a fixed bed reactor.* Bioresource Technology, 2010. **101**(15): p. 6151-6156.
9. Merdun, H. and Z.B. Laougé, *Kinetic and thermodynamic analyses during co-pyrolysis of greenhouse wastes and coal by TGA.* Renewable Energy, 2021. **163**: p. 453-464.
10. Ding, G., et al., *Synergistic effect, kinetic and thermodynamics parameters analyses of co-gasification of municipal solid waste and bituminous coal with CO2.* Waste Management, 2021. **119**: p. 342-355.
11. Hameed, Z., et al., *Kinetic and Thermodynamic Analyses of Sugar Cane Bagasse and Sewage Sludge Co-pyrolysis Process.* Energy & Fuels, 2018. **32**(9): p. 9551-9558.
12. Zhou, L., et al., *Effects of Contact Conditions between Particles and Volatiles during Co-Pyrolysis of Brown Coal and Wheat Straw in a Thermogravimetric Analyzer and Fixed-Bed Reactor.* Processes, 2019. **7**(4): p. 179.
13. Liu, X., M. Chen, and Y. Wei, *Kinetics based on two-stage scheme for co-combustion of herbaceous biomass and bituminous coal.* Fuel, 2015. **143**: p. 577-585.
14. Ali, I., S.R. Naqvi, and A. Bahadar, *Kinetic analysis of Botryococcus braunii pyrolysis using model-free and model fitting methods.* Fuel, 2018. **214**: p. 369-380.
15. Ashraf, A., H. Sattar, and S. Munir, *A comparative applicability study of model-fitting and model-free kinetic analysis approaches to non-isothermal pyrolysis of coal and agricultural residues.* Fuel, 2019. **240**: p. 326-333.
16. Nyoni, B., et al., *Co-pyrolysis of South African bituminous coal and Scenedesmus microalgae: Kinetics and synergistic effects study.* International Journal of Coal Science & Technology, 2020. **7**(4): p. 807-815.
17. Lu, K.-M., et al., *Thermogravimetric analysis and kinetics of co-pyrolysis of raw/torrefied wood and coal blends.* Applied Energy, 2013. **105**: p. 57-65.
18. Ali, I., et al., *Kinetic and thermodynamic analyses of dried oily sludge pyrolysis.* Journal of the Energy Institute, 2021. **95**: p. 30-40.

19. Naqvi, S.R., et al., *Synergistic effect on co-pyrolysis of rice husk and sewage sludge by thermal behavior, kinetics, thermodynamic parameters and artificial neural network.* Waste Management, 2019. **85**: p. 131-140.
20. Vasilopoulos, Y., E. Skořepová, and M. Šoóš, *COMF: Comprehensive Model-Fitting Method for Simulating Isothermal and Single-Step Solid-State Reactions.* Crystals, 2020. **10**(2): p. 139.
21. Parthasarathy, P., et al., *Thermal degradation characteristics and gasification kinetics of camel manure using thermogravimetric analysis.* Journal of Environmental Management, 2021. **287**: p. 112345.
22. Vasudev, V., X. Ku, and J. Lin, *Pyrolysis of algal biomass: Determination of the kinetic triplet and thermodynamic analysis.* Bioresource Technology, 2020. **317**: p. 124007.

Chapter 4 Results and Discussion

4.1 Physiochemical properties of individual BC and AC and their blends

4.1.1 Ultimate Analysis (CHN-S)

The Ultimate analysis of 100%BC, 100%AC, and the four (BC-AC) blends are shown in Fig. 4.1(a-d). The ultimate analysis showed that the carbon content of 100%AC was approximately 26.5% which was two and half times lower than the carbon content of 100%BC which was 68.08%, thus the sample coal lies in the category of bituminous coal as shown in Fig. 4.1(a). In the research literature, a similar carbon composition for 100%BC has been reported [1]. In this study, almost the same amount of carbon in both samples of algae has been detected [2]. The hydrogen content of the 100%BC and 100%AC samples were 3.85% and 5.55% respectively, therefore showing that they are close to each other and that algal biomass has a higher hydrogen content as shown in Fig. 4.1(b). Similar findings have also been reported by Kirtania and Bhattacharya [3], as their algae sample had a similar hydrogen content. Although the nitrogen content of 100%BC was 1.28%, in some studies almost a similar amount of nitrogen in bituminous coal was reported, however, the nitrogen content of 100%AC which was 2.11% was higher than that of 100%BC as shown in Fig. 4.1(c) [4]. The sulfur content of 100%AC was 0.26% which was much lower than that of 100%BC, which was 0.48% as shown in Fig. 4.1(d). Some of the studies reported nearly the same amount of sulfur in their coal and a similar amount of sulfur and nitrogen in their Algae [5-7]. The presence of hydrogen, nitrogen, and sulfur together was higher in 100%AC as compared to the 100%BC because its culture medium carries these elements as nutrients whilst the presence of carbon in 100%BC was higher because it is its main constituent. The nearly same amount of elemental composition was also reported for algal biomass such as rhizoclonium riparium in the literature [8]. The low carbon content as compared to lignocellulosic biomass is common in most algal biomass and is due to the high ash content [9].

The ultimate analysis of the four blends shows that the percentage composition of carbon increases with the increasing ratio of BC in the blends as shown in Fig. 4.1(a). A similar trend of increasing the percentage of carbon in their coal has been reported by Anukam et al. [10]. The

hydrogen composition showed an increasing trend from 100%BC to 100%AC in the blends as the ratio of AC increased as depicted in Fig. 4.1(b). The nitrogen composition showed an increasing trend from 100%BC to 100%AC as the ratio of BC decreases along with the blends as depicted in Fig. 4.1(c). The composition of sulfur also showed an increasing trend from 100%AC to 100%BC as the ratio of the BC in the blends increased as illustrated in Fig. 4.1(d).

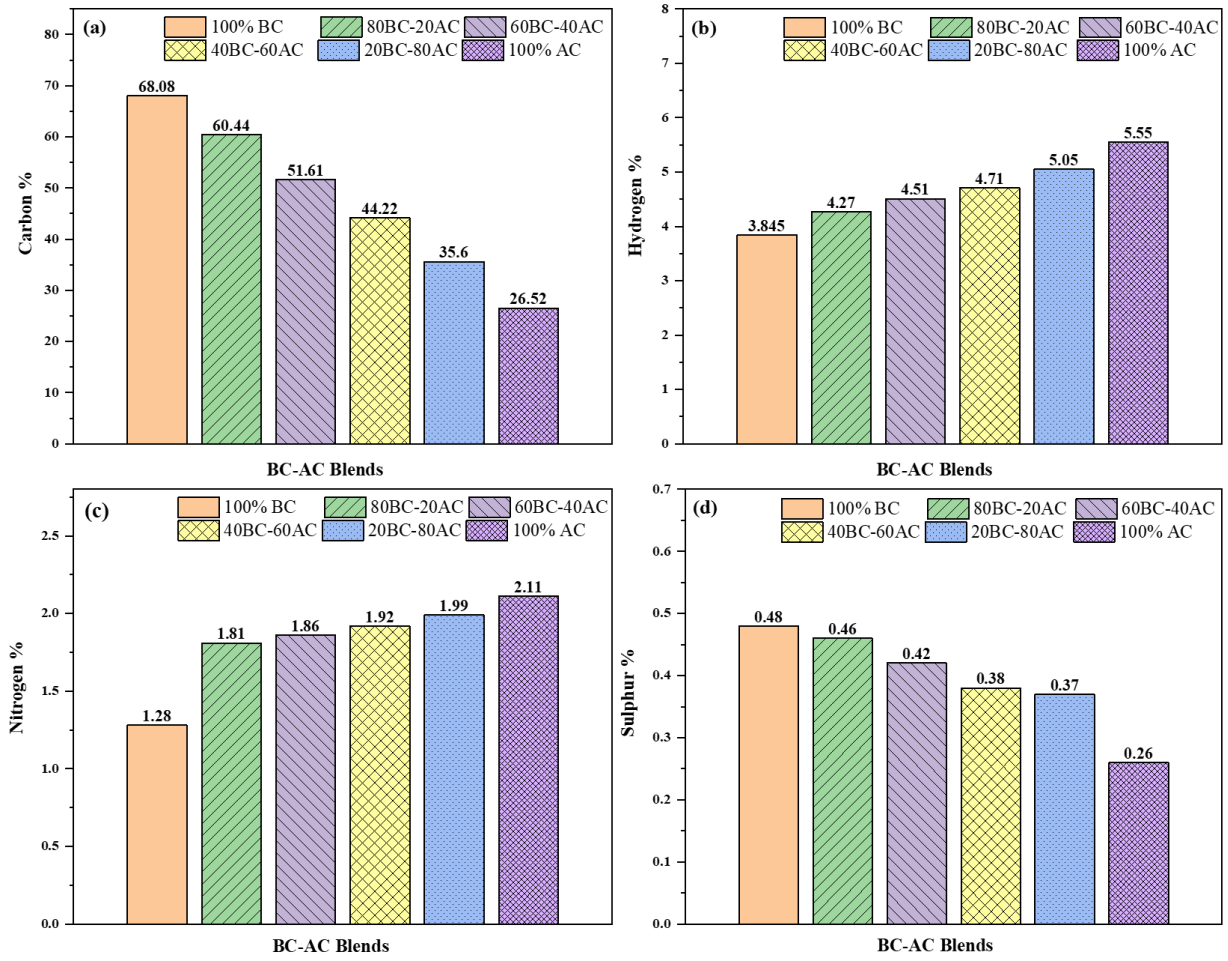

Fig. 4.1 CHN-S of bituminous coal and algae consortium and their four blends (a) Carbon, (b) Hydrogen, (c) Nitrogen, and (d) Sulfur.

4.1.2 Gross Calorific Value (GCV)

The GCV of 100%BC, 100%AC, and their four (BC-AC) blends were determined by a Parr 6200 oxygen bomb calorimeter, which was used to specifically determine the heat of combustion of the samples as shown in Fig. 4.2. GCV is an important property of a fuel that makes

it easier to define the energy content in a fuel [11]. GCV of a fuel is an essential factor because it indicates how much chemical energy is contained in a given amount of fuel [12]. In Fig. 4.2 it is shown that the GCV of 100%BC was 28.5 MJ kg^{-1} indicating its suitable use for power generation. Similar GCV values are reported in the research literature for low-volatile bituminous coal [13]. The GCV of 100%AC was recorded as 10.1 MJ kg^{-1} as shown in Fig. 4.2, which was of the same magnitude reported in the research literature [14]. This low value of GCV for 100%AC can be explained by the high ash and moisture content as well as the low carbon content as shown in the ultimate analysis of 100%AC [15]. The GCV of the four (BC-AC) blends are also shown in Fig. 4.2, i.e. (80BC-20AC) was 25.32 MJ kg^{-1}, (60BC-40AC) was 21.22 MJ kg^{-1}, (40BC-60AC) was 17.23 MJ kg^{-1}, and (20BC-80AC) was 13.98 MJ kg^{-1}. These results showed a decreasing trend of GCV from 100% BC to 100% AC as the ratio of AC in the blends increases. The value of the four (BC-AC) blends lies in between the parent fuels. This decreasing trend is explainable by the fact that AC contains high moisture content, high ash content, high volatiles, and low carbon content.

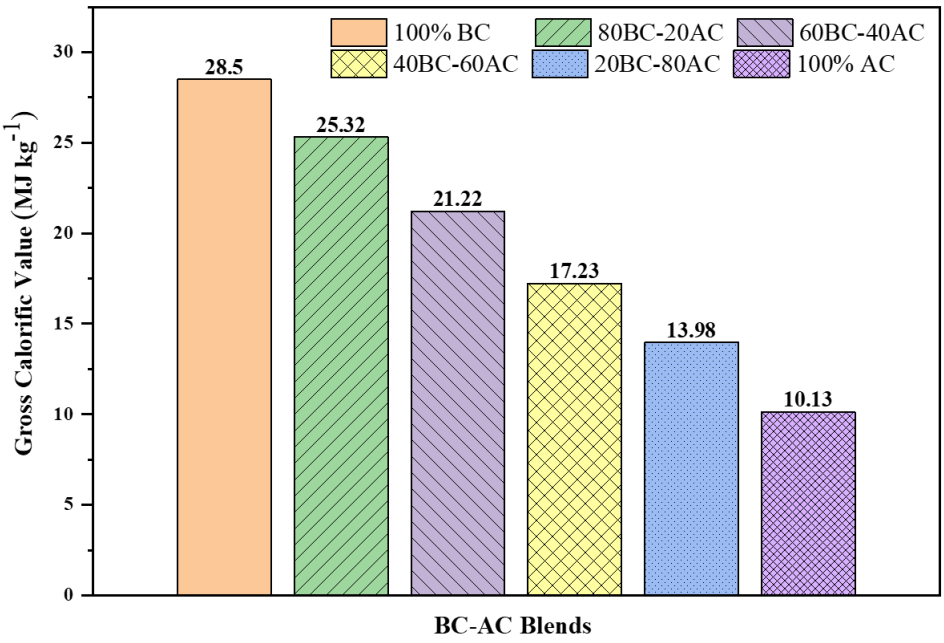

Fig. 4.2 Gross calorific value of bituminous coal and algae consortium and their four blends

4.1.3 Fourier transform infrared spectroscopy (FTIR)

The FTIR spectra of 100%BC, 100%AC, and the four (BC-AC) blends are presented in Fig. 4.3. While some significant differences between them can be seen in the main functional groups on the surface, it is one of the most versatile techniques for studying the structure and properties of materials, thus revealing crucial information about the chemical structure.

At first, examining the FTIR Spectra of 100%BC reveals the first absorption broadening peak was 3400 cm^{-1} which is found mostly in the range of (3700 – 3000 cm^{-1}) which occurs due to the absorption of hydroxyl stretching vibration groups (−OH−) such as phenolic or alcoholic compounds or which are linked to oxygen functional groups, such as carboxylic acid, as well as minerals, such as kaolin or halloysite, as shown in Fig. 4.3. In the research literature, similar peaks were reported for 100%BC [16, 17]. The stretching absorption peaks of 2920 cm^{-1} and 2850 cm^{-1} found in the range of (3000 – 2800 cm^{-1}) correspond to a methylene group (−CH_2−) present in a saturated aliphatic hydrocarbon as depicted in Fig. 4.3, with the same peaks observed in the literature [17]. However, the strong absorption peak which was abundantly found in 100%BC is 1600 cm^{-1} found in the range of (1640 – 1520 cm^{-1}) originates from the stretching vibration of

aromatic ring structure −C=C− groups in the benzene ring representing high carbon content in 100 %BC as indicated in Fig. 4.3, the similar peak was observed in the literature [18]. The broadening absorption peak of 1440 cm^{-1} found in the range of (1520 – 1320 cm^{-1}) corresponds to the methyl ($-CH_3$) stretching deformation vibration which indicates aliphatic moieties, the same peak was reported in the literature [19]. The broadening absorption peak of 1015 cm^{-1} represented the plane deformation structures of C−C and C−H in the aromatic structure as shown in Fig. 4.3 [20]. The narrow and broadening absorption peaks of 910 and 750 cm^{-1} respectively found in the range of (920 – 700 cm^{-1}) correspond to the out-of-plane deformation vibration of =C−H in aromatic structures [21].

Furthermore, Fig. 4.3 shows the FTIR spectra of 100%AC biomass and their respective absorption peaks. The first broadening absorption peak was in the range of (3700 – 3000 cm^{-1}) which is 3275 cm^{-1} as shown in Fig. 4.3 and is most abundantly found in 100%AC biomass which occurs due to the absorption of hydroxyl stretching vibration groups (−OH−) bonds [22]. The stretching absorption peak of 2916 cm^{-1} is found in the range of (3000 – 2800 cm^{-1}) which indicates the methylene stretching region ($-CH_2-$) also known as N–H stretching (protein) or =C−H and C–H stretching (lipid carbohydrate) [23]. A narrow absorption peak was observed at 1638 cm^{-1} and 1535 cm^{-1} found in the range of (1709–1500 cm^{-1}) which occurs due to the C=O stretching (protein amide I band), indicating low carbon content than 100%BC and symmetric deformation of N−H bending of amide II [24, 25]. The narrow and broadening absorption peaks of 1154 and 1010 cm^{-1} originate because of Carbohydrate C−O−C symmetric stretching of polysaccharides in 100%AC, the same peaks were observed in the literature [26]. The narrow absorption peak of 871 cm^{-1} was observed, which occurs due to C–O stretching as shown in Fig. 4.3 [27].

Thus, when 100%BC is merged with 100%AC, the intensity of the functional group changes, so BC-AC blends show the intermediary behavior in terms of band intensity. As shown in Fig. 4.3 the peaks existing in blends (80BC-20AC), (60BC-40AC), (40BC-60AC), (20BC-80AC) are discussed. The absorption peaks existing in the range of (3317–3275 cm^{-1}) occur due to the absorption of hydroxyl stretching vibration groups (−OH−) bonds such as phenolic or alcoholic compounds. This peak strengthens as the ratio of AC increases in the blends. The peak existing in the range of (2916–2914 cm^{-1}) corresponds to a methylene stretching group ($-CH_2-$) present in a saturated aliphatic hydrocarbon or also known as N–H stretching (protein) or =C−H

and C–H stretching (lipid carbohydrate). Another visible absorption peak was also observed in the range of (1620–1583 cm^{-1}) originating from the stretching vibration of aromatic ring structure −C=C− groups in the benzene ring, also due to the C=O stretching (protein amide I band) and symmetric deformation of N−H bending of amide II, both of them were observed due to the presence of both 100%BC and 100%AC in the blends as the ratio of AC in the blends increases, the peak shortens. However, 100%AC has less aromatic ring stretching indicating that the 100%AC has lower carbon content than 100%BC. Furthermore, two more peaks were found in the range of (1433–1412 cm^{-1}) which corresponds to the methyl ($-CH_3$) stretching deformation vibration indicating aliphatic moieties, and another peak found was in the range of (1013–1008 cm^{-1}) representing the plane deformation structures of C−C and C−H in the aromatic structure and carbohydrate C−O−C symmetric stretching of polysaccharides. The peak mentioned in this region strengthens as the ratio of AC increases in the blends. In both the parent fuels and their four blends the determination of carbon content, lipids, carbohydrates, and protein content using FTIR has been well documented in the literature [63]. It is also observed that the bandwidth also changes as the blending ratio varies. So, the bandwidth of the four blends lies in between the parent bandwidth of both 100%BC and 100%AC.

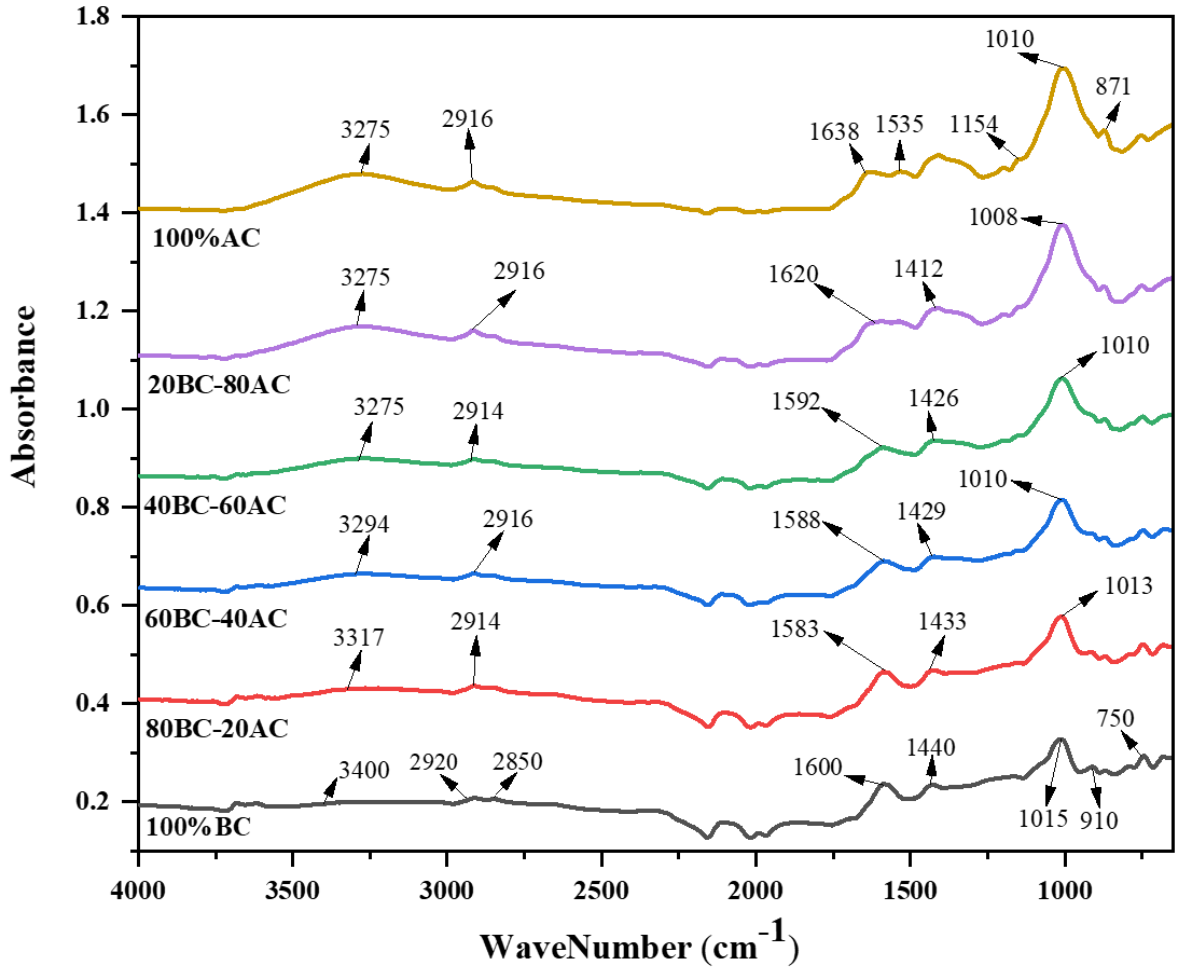

Fig. 4.3 FTIR of pure bituminous coal and algae consortium and their four blends

4.1.4 Thermo-gravimetric analysis (TGA)

The WL% of 100%BC, 100%AC, and their four (BC-AC) blends with respect to temperature and (DTG) in terms of (wt. %/min) were analyzed by the TGA as shown in Fig. 4.4(a-d) and Fig. 4.5(a, b). TGA provides helpful information about the WL% and decomposition rate, and the TGA measurements provide a suitable estimation for the kinetic parameters of co-pyrolysis [28].

The WL% behavior of 100%BC and 100%AC are characterized by a three-stage thermal reaction regardless of their type [29]. A slight WL% in 100%BC was observed in the first stage in the range of 25 – 400 °C, which was due to the removal of moisture content from 100%BC as

shown in Fig. 4.4(a), there was no significant peak in this stage. In the second stage, the decomposition of fuels mainly takes place, this stage develops at 400 – 600 °C, in which significant WL% occurs and can be seen in Fig. 4.4(a), the T_p of 100%BC is 455 °C, and the wt. %/min is found to be (-1.66%/min), and similar readings for the second stage have been found in the literature. Additionally, the 100%BC has a high carbon content of almost 68%, delaying the pyrolysis reaction, also the high WL% in this stage is mainly due to its high reactivity [30]. In the third stage starting at 600 – 900 °C, slow decomposition occurs, and the WL% and the decomposition of the solid residue are small as shown in Fig. 4.4(a) [12]. With the formation of char and H_2, CO_2, and CO generation, the reactions will take place [31]. The main components of algal biomass are proteins, carbohydrates, and lipids, because of this reason it is different from lignocellulosic biomass and the WL% in 100%AC is as depicted in Fig. 4.4(b), which shows that it starts earlier than 100%BC, and is also characterized by a three-stage thermal reaction. A slight WL% in 100%AC was also observed in the first stage which occurs in the range of 25 – 240 °C, in which the removal of moisture and some light volatile matters happens, similar readings were found in the literature [32]. In the second stage, the thermal decomposition of the organic phase (carbohydrates, proteins, and lipids) occurs which is also known as the active pyrolysis zone [33], develops in the range of 240 – 520 °C where significant WL% can be seen. Multiple peaks were observed during the WL% of 100%AC in this stage between the ranges of 270 – 350 °C, 370 – 450 °C, and 450 – 520 °C which is attributed to the decomposition of carbohydrates, proteins, and a weak WL% peak exists for lipids as shown in Fig. 4.4(b), almost similar results were reported in the literature [34]. In the third stage also known as the secondary pyrolysis zone, the reaction occurred at a high temperature, between 520 – 900 °C, and slow decomposition occurs, attributed to the carbonaceous residues and the naturally existing minerals, which have a more complicated structure and are more difficult to break down such as bio-char which decomposes at a very slow rate [25].

The temperature at which the maximum rate of the WL% occurs during the process, the maximum reactivity temperature, is indicated as the peak in the DTG curve. The T_p at which maximum WL% occurs in the second stage reaction for 100%BC is 455 °C and (wt. %/min) is found to be -1.66%/min. The peak DTG curve exhibited for 100%BC in Fig. 4.4(c) is attributed to the release of volatile matter during the pyrolysis process [29]. The T_p at which maximum WL% occurs in the second stage reaction for 100%AC is 301 °C and (wt. %/min) is -3.8%/min. The peak

DTG curve exhibited for 100%AC in Fig. 4.4(d) is attributed to the thermal decomposition of soluble polysaccharides, amino acids, and other compounds [27]. A small peak was also indicated in the third stage at 640 °C which is attributed to the carbonaceous residues and the naturally existing minerals in 100%AC [25]. The T_p of 100%BC was greater than the 100 %AC. The most reactive fuel is the one with the highest rate of WL% and eventually has the lower T_p [29]. The overall WL% at the end of the reaction was 27% for 100%BC and 100%AC was 56.8% and the RL% at the end of the reaction was 73% for 100%BC, 43.2% for 100%AC.

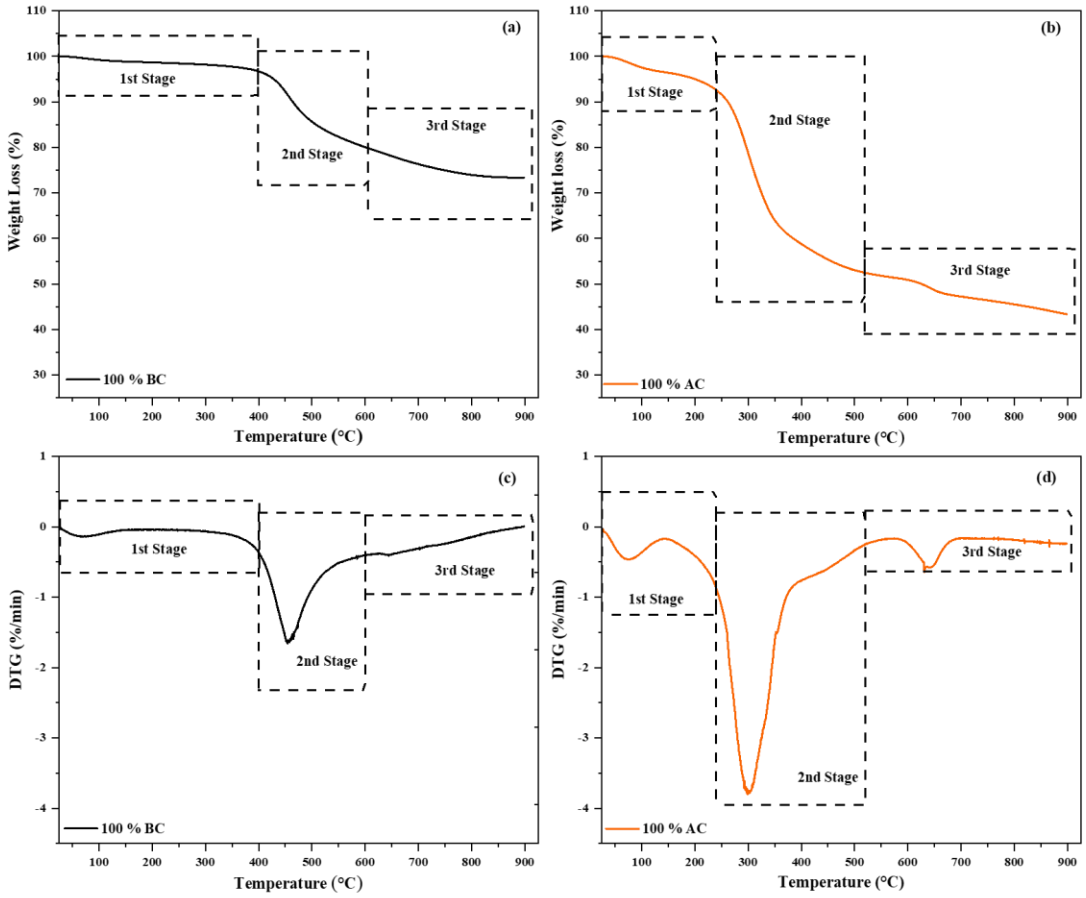

Fig. 4.4 Pure TGA of bituminous coal and algae consortium (a) TGA of 100%BC (b) TGA of 100%AC (c) DTG of 100%BC (d) DTG of 100%AC

The four (BC-AC) blends (80BC-20AC), (60BC-40AC), (40BC-60AC), (20BC-80AC) as shown in Fig. 4.5(a) displayed four stages of thermal reaction [29]. The temperature range for the first stage was 25 – 130 °C, where slight WL% occurs due to moisture evaporation with no

significant differences due to blending. The temperature range for the second stage was 130 – 400 °C where significant WL% can be seen indicating the decomposition of the fundamental constituents of AC in the blends and the peak strengthens which reflects the increase in the ratio of AC present in the blends. The temperature range for the third stage was 400 – 590 °C and significant WL% can be seen due to the decomposition of the constituents of BC in the blends which represents a decrease in the ratio of BC in the blends as the peak shortens. A small peak was also indicated in the fourth stage in the temperature range of 590 – 900 °C which is mainly attributed to the decomposition of carbonaceous residues mostly biochar which is formed in the previous steps and the naturally existing minerals [25]. Depending on the blending ratios, the WL% behavior of the blends mirrors the behavior of the constituent materials during co-pyrolysis. The WL% was reduced as the quantity of BC was increased in the blends, suggesting that the low-volatile content of BC had an impact on the blends' WL% [12].

The four (BC-AC) blends as shown in Fig. 4.5(b) showed two peaks in two stages in the DTG curve. The T_p at which the maximum rate of WL% occurs in the second and third reaction stage for (80BC-20AC) was 305 °C and 459 °C respectively and (wt. %/min) was -0.69%/min and -1.07%/min. The T_p for (60BC-40AC) at which maximum WL% occurs in the second and third stage was 304 °C and 456 °C while (wt. %/min) was -1.54%/min and -1.20%/min respectively. The T_p at which maximum WL% occurs was in the second and third stage for (40BC-60AC), which was 303 °C and 455 °C respectively and the (wt. %/min) was -2.17%/min and -0.71%/min. The T_p for (20BC-80AC) at which maximum WL% occurs was in the second and third reaction stage which was 302 °C and 454 °C while the (wt. %/min) was found to be -3.04%/min and -0.64%/min. The peak intensity in the third stage was lower than that of the second stage. Fig. 4.5(b) shows that as the ratio of AC increases in the blends, the T_p decreases gradually in both the second and third stages of the process which shows the reactivity dominance of algae in the blends. The second peak decreases with the decrease in the ratio of AC, while the third peak increases with an increase in the ratio of BC. The overall WL% at the end was 33.5% for (80BC-20AC), 39% for (60BC-40AC), 43.9% for (40BC-60AC) and 52.5% for (20BC-80AC) and the RL% at the end of reaction was 66.5% for (80BC-20AC), 61% for (60BC-40AC), 56.1% for (40BC-60AC) and 47.5% for (20BC-80AC).

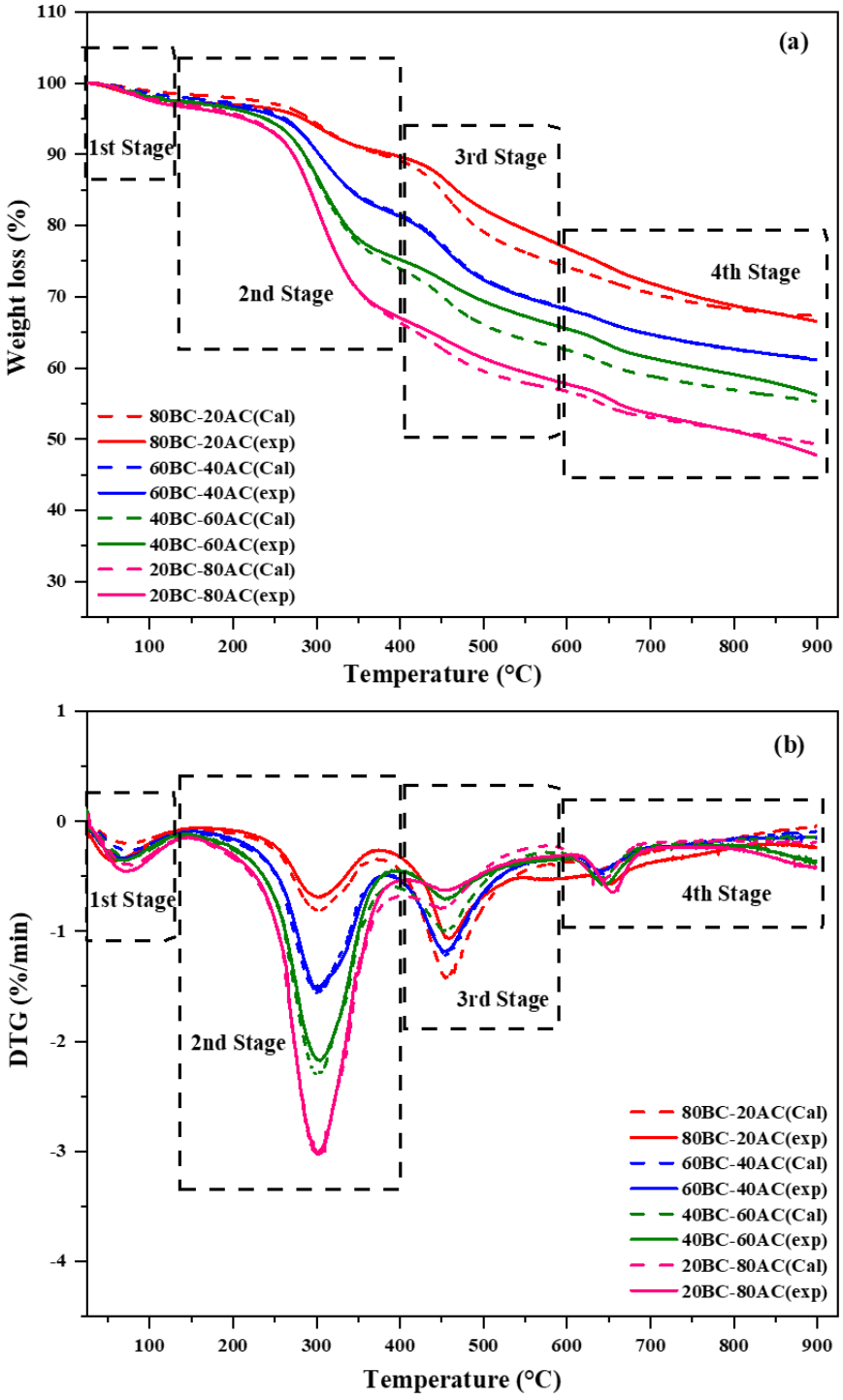

Fig. 4.5 TGA of bituminous coal and algae consortium four blends (a) TGA with synergy (b) DTG with synergy

4.1.5 Synergistic effect of co-pyrolysis

To investigate the synergistic effects between 100%BC and 100%AC during Co-Pyrolysis in TGA, the thermal decomposition of (BC-AC) blends was observed. The experimental and calculated TGA and DTG curves of the blends are plotted in Fig. 4.5(a-b). The maximum relative errors between the experimental and calculated TGA curves of blends are further examined in Table 4.1. A positive synergistic effect value demonstrates that co-pyrolysis can yield more volatiles than individual pyrolysis [35]. The importance of synergistic effects in modifying the existing pyrolysis process and improving the properties of bio-oil cannot be ignored. A large number of research groups have investigated the phenomenon, focusing particularly on the mechanism of synergistic effects and the enhancement of the target product during co-pyrolysis [36]. Heat transfer during co-pyrolysis also contributes to the synergistic effect [37]. The free-radical mechanisms in the co-pyrolysis process contribute to the synergistic effects, thus producing improved bio-fuels with high GCV [38].

In Fig. 4.5(a-b) for 80BC-20AC, it can be seen from the TG curve that in the first stage there was minimal difference between the experimental and the theoretical value. The difference between the experimental and theoretical values seen in the second, third, and fourth stages from which the first two stages are the main pyrolysis zones, shows that there was a certain synergy between 100%BC and 100%AC. The percentage deviation values in terms of WL% of 80BC-20AC were 2.13%, while the negative synergistic effects of - 1.04% in terms of RL%. In the case of 60BC-40AC, in the first and second stages, no significant difference between the experimental and the theoretical value appeared due to their overlapping as shown. The difference between the experimental and theoretical values can only be seen in the third and four stages out of which the third stage was the main pyrolysis zone indicating slight synergy between 100%BC and 100%AC. The percentage deviation values in terms of WL% of 60BC-40AC were 1.03%, while the negative synergistic effects of - 0.65% in terms of RL%. In the case of 40BC-60AC and 20BC-80AC, in the first and second stages, no significant difference between the experimental and the theoretical value could be seen. A slight difference between the experimental and theoretical values can only be seen in the third and four stages out of which the third stage was the main pyrolysis zone, indicating a certain synergy between 100%BC and 100%AC. For 40BC-60AC the percentage deviation value in terms of WL% was - 1.79% which was a negative synergistic effect while the

positive synergistic effects of 1.45% can be seen in terms of RL%, which implies that there were possibly slight synergistic effects that contributed to the production of char [39]. The percentage deviation values in terms of WL% of 20BC-80AC were 3.55%, while the negative synergistic effects of - 3.65% in terms of RL%. The percentage deviation values in terms of $(DTG)_{max}$ showed negative synergistic effects for all four blends. Synergistic effects in all blends were strongly observed after 400 °C in the third and fourth stages when the pyrolysis of BC starts in the blends as shown in Fig. 4.5(a). From the product's point of view, the positive synergistic effects in terms of WL% suggest that they were all preferable for bio-oil and biogas yield due to the release of volatiles along with the negative synergistic effects in terms of RL% [35]. Positive synergistic effects in terms of RL% indicate that the given sample is suitable for bio-char yield, along with a negative value in WL%. It is thus concluded that the synergistic effects between 100%BC and 100%AC are considered slightly significant at some points when they are co-pyrolyzed. The deviation in the values is higher in terms of WL% for both 80BC-20AC and 20BC-80AC out of all the four blends, so based on synergistic effects 20BC-80AC is considered an optimum blend.

Table 4.1 Synergistic effects calculation during co-pyrolysis of (BC – AC) Blends

Sample	Experimental Value (Y_E)			Calculated Value (Y_C)			Deviation (%)		
	WL%	RL%	$(DTG)_{max}$ (wt. %/min)	WL%	RL%	$(DTG)_{max}$ (wt. %/min)	WL%	RL%	$(DTG)_{max}$ (wt. %/min)
100%BC	27.00	73.00	-1.66	Nil	Nil	Nil	Nil	Nil	Nil
80BC-20AC	33.50	66.50	-1.07	32.80	67.20	-1.44	2.13	-1.04	-25.70
60BC-40AC	39.00	61.00	-1.54	38.60	61.40	-1.56	1.03	-0.65	-1.28
40BC-60AC	43.90	56.10	-2.17	44.70	55.30	-2.31	-1.79	1.45	-6.06
20BC-80AC	52.50	47.50	-3.04	50.70	49.30	-3.06	3.55	-3.65	-0.65
100%AC	56.80	43.20	-3.80	Nil	Nil	Nil	Nil	Nil	Nil

4.2 Kinetics and thermodynamics behavior

4.2.1 Kinetic Analysis

The kinetic triplet's i.e. activation energy (E_a), linear regression (R^2), and pre-exponential factor (A) were calculated based on the data obtained from the co-pyrolysis of 100%BC, 100%AC, and the four (BC-AC) blends in TGA as displayed in Table 4.2 and Table 4.3. R^2 was used to calculate E_a and A for certain reaction mechanisms using the TGA data from the co-pyrolysis process and the precision of fitting data was based on R^2 with the specified range from 0.90 to 0.99 [40, 41]. To assess the impact of blending ratio on co-pyrolysis features and kinetics, the Coats-Redfern integral method was used to get an in-depth approach to the kinetic profiles. To calculate the kinetic parameters, eighteen reaction mechanisms were investigated and plotted between $ln\left[\frac{g(\alpha)}{T^2}\right]$ and $\frac{1}{T}$ at a constant heating rate of 10 °C/min. The slope of the plot was used to calculate the E_a. The kinetic study was performed on the active pyrolysis region because a greater percentage of WL% occurs in this zone [42]. The E_a is the minimum amount of energy required to initiate a reaction, whereas the A is the quantity of colliding molecules in the direction required to initiate the reaction [43]. The E_a determines the reactivity of samples, whereas the A is more related to the material structure [29].

The WL% in the pyrolysis of 100%BC and 100%AC can be regarded as a single-stage process with individual E_a, R^2, and A. This rapid decomposition zone is considered the active pyrolysis stage, furthermore, for 100%BC, while for 100%AC, which lies in a temperature range of 338 – 600 °C. For both stages, usually, 100%BC has the highest E_a and A than that of 100%AC for all the eighteen reaction mechanisms. The results for the parent sample kinetic analysis are displayed in Table 4.2.

For 100%BC the best model with the highest R^2 value of 0.975 was the F3 model having an E_a of 85.04 kJ/mol with an A of 138638.36 min^{-1}, so this model was the most probable mechanism of 100%BC thermal decomposition as shown in Fig. 4.6. The D3 model was the best with the highest R^2 value of 0.979 having an E_a of 78.22 kJ/mol with an A of 46116.20 min^{-1}, and considered the most feasible mechanism of 100%AC thermal decomposition as shown in Fig. 4.6.

Table 4.2 Represents the Kinetic parameters of Pure BC and AC at different temperature stages

		Temperature Range		Kinetic Parameters		
Symbols	**Sample Name**	**1st Stage**	**T_P (°C)**	**E_a (kJ/mol)**	**A (min^{-1})**	**R^2**
F1/3	100%BC	(338 – 600 °C)	455.0	46.16	55.98	0.942
	100%AC	(145 – 425.8 °C)	301.0	32.47	31.74	0.968
F1	100%BC	(338 – 600 °C)	455.0	54.17	292.12	0.959
	100%AC	(145 – 425.8 °C)	301.0	36.94	114.40	0.975
F3/2	100%BC	(338 – 600 °C)	455.0	60.95	1156.75	0.968
	100%AC	(145 – 425.8 °C)	301.0	40.74	334.49	0.976
F2	100%BC	(338 – 600 °C)	455.0	68.38	5136.23	0.973
	100%AC	(145 – 425.8 °C)	301.0	44.91	1072.85	0.974
F3	100%BC	(338 – 600 °C)	455.0	85.04	138638.36	0.975
	100%AC	(145 – 425.8 °C)	301.0	54.25	14167.10	0.962
F4	100%BC	(338 – 600 °C)	455.0	103.74	5312075.13	0.970
	100%AC	(145 – 425.8 °C)	301.0	64.73	245316.09	0.946
R1	100%BC	(338 – 600 °C)	455.0	42.58	26.48	0.931
	100%AC	(145 – 425.8 °C)	301.0	30.48	17.81	0.962
R2	100%BC	(338 – 600 °C)	455.0	48.05	41.49	0.947
	100%AC	(145 – 425.8 °C)	301.0	33.53	21.52	0.970
R3	100%BC	(338 – 600 °C)	455.0	50.02	41.53	0.951
	100%AC	(145 – 425.8 °C)	301.0	34.62	19.67	0.972
P2	100%BC	(338 – 600 °C)	455.0	15.23	0.21	0.866
	100%AC	(145 – 425.8 °C)	301.0	10.75	0.19	0.920
P3	100%BC	(338 – 600 °C)	455.0	6.10	0.02	0.688

	100%AC	(145 – 425.8 °C)	301.0	4.18	0.02	0.780
P4	100%BC	(338 – 600 °C)	455.0	1.54	0.003	0.190
	100%AC	(145 – 425.8 °C)	301.0	0.89	0.003	0.204
D1	100%BC	(338 – 600 °C)	455.0	97.32	124456.69	0.948
	100%AC	(145 – 425.8 °C)	301.0	69.94	43629.61	0.972
D2	100%BC	(338 – 600 °C)	455.0	104.22	242502.18	0.955
	100%AC	(145 – 425.8 °C)	301.0	73.77	62224.70	0.976
D3	100%BC	(338 – 600 °C)	455.0	112.20	255840.60	0.962
	100%AC	(145 – 425.8 °C)	301.0	78.22	46116.20	0.979
D4	100%BC	(338 – 600 °C)	455.0	106.86	90408.92	0.957
	100%AC	(145 – 425.8 °C)	301.0	75.25	20623.52	0.977
A2	100%BC	(338 – 600 °C)	455.0	21.02	0.85	0.931
	100%AC	(145 – 425.8 °C)	301.0	13.99	0.58	0.956
A3	100%BC	(338 – 600 °C)	455.0	9.97	0.078	0.868
	100%AC	(145 – 425.8 °C)	301.0	6.33	0.061	0.907

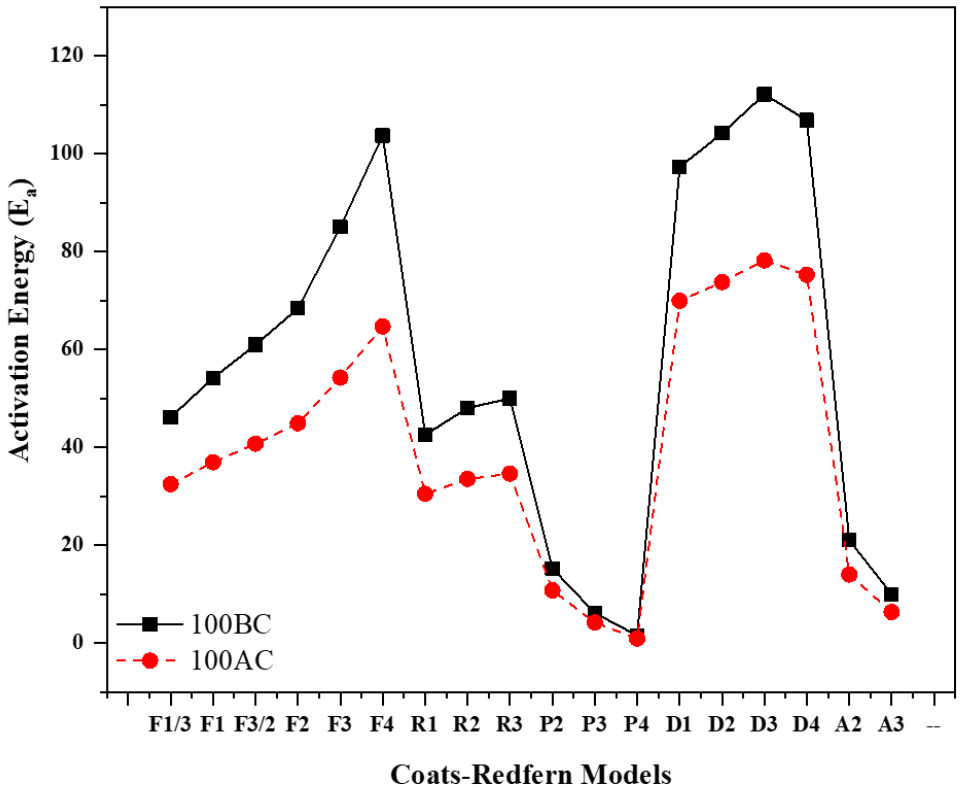

Fig. 4.6 Activation energy (Ea) of different models for pure bituminous coal and algae consortium

The WL% in the co-pyrolysis of the four (BC-AC) blends can be considered as a two-stage process with individual E_a, R^2, and A for each stage. The first and second stages are considered the active pyrolysis stages in all of the four blends, the first stage corresponds to the decomposition of the organic phase of algal biomass which lies in a temperature range of 145 – 400 °C, while the second stage indicates the release of volatile matters which occurs in the temperature range of 400 – 610 °C. The results for the four (BC-AC) blends kinetic analysis are displayed in Table 4.3.

In the first stage from 145 – 400 °C, for (80BC-20AC) the model with the highest R^2 value of 0.977 was the D1 model having an E_a of 62.79 kJ/mol with an A of 1628.24 min^{-1}, so this was the most likely mechanism of (80BC-20AC) thermal decomposition as shown in Fig. 4.7(a). For the (60BC-40AC) blend, the D1 model was the best with the highest R^2 value of 0.980 with an E_a of 68.64 kJ/mol and A of 15328.85 min^{-1} considered as the most probable mechanism as shown in

Fig. 4.7(a). The model with the highest R^2 value of 0.982 was the D1 model having an E_a of 71.58 kJ/mol with an A of 45613.99 min^{-1}, so this model is the most likely mechanism for the (40BC-60AC) blend as shown in Fig. 4.7(a). The D2 model was the best with the highest R^2 value of 0.981 having an E_a of 76.35 kJ/mol and A of 93579.64 min^{-1}, regarded as the most feasible mechanism of (20BC-80AC) blend as shown in Fig. 4.7(a).

In the second stage from 400 – 610 °C, the D4 model with the highest R^2 value of 0.979 was the best with an E_a of 47.75 kJ/mol and A of 6.21 min^{-1}, considered the most possible mechanism for (80BC-20AC) blend as shown in Fig. 4.7(b). For the (60BC-40AC) blend, the best model with the highest R^2 value of 0.989 was the F3 model which had an E_a of 54.81 kJ/mol with an A of 3084.78 min^{-1}, being the most likely mechanism as shown in Fig. 4.7(b). For the (40BC-60AC) blend, the F2 model was the best with the highest R^2 value of 0.996 having an E_a of 19.20 kJ/mol with an A of 2.05 min^{-1}, regarded as the most feasible mechanism as shown in Fig. 4.7(b). The F2 model was the best with the highest R^2 value of 0.997 having an E_a of 15.33 kJ/mol with an A of 1.13 min^{-1}, so this was the most probable mechanism for (20BC-80AC) as shown in Fig. 4.7(b).

The E_a for (BC-AC) blends in the first stage increases as the ratio of 100%AC increases, whereas in the second stage the E_a decreases as the percentage of 100%AC increases in (BC-AC) blends. This shows that co-pyrolysis reduces the E_a of 100%AC biomass [44]. The value of the pre-exponential factor increases in the first stage as the ratio of 100%AC increases in (BC-AC) blends, whereas in the second stage the value of A decreases as the ratio of 100%AC increases in the blend. This also suggests that the structure of 100%AC has an impact on the pyrolysis of 100%BC, which was a similar trend reported in the research literature [29]. The larger the value of A, the reaction will be more complicated [45]. It can be seen from the data displayed in tables Table 4.2 and Table 4.3, that by increasing the 100%AC ratio in blends, the E_a and A of the blends also increases under 400 °C temperature, and similar results were reported [46]. The E_a and A of the optimum blend (20BC-80AC) were also discussed above, and showed a reduction in the E_a of both 100%BC and 100%AC, thus showing agreement with our selection of the optimum blend. Kinetic parameters are another important aspect of thermal behavior from the co-pyrolysis process contributing to the design of the reactor. The study revealed that kinetic characteristics may be used to show the blends' co-pyrolysis process [34].

Table 4.3 Represents the Kinetic parameters of the four (BC–AC) Blends at different temperature stages

		1st Stage (145 – 400 °C)				2nd Stage (400 – 610 °C)			
Symbols	**Sample Name**	**E_a (kJ/mol)**	**A (min^{-1})**	**R^2**	**T_P (°C)**	**E_a (kJ/mol)**	**A (min^{-1})**	**R^2**	**T_P (°C)**
F1/3	80BC–20AC	27.52	3.83	0.970	305.0	16.90	0.27	0.961	459.0
	60BC–40AC	30.88	14.15	0.974	304.0	6.19	0.03	0.793	453.2
	40BC–60AC	32.72	27.93	0.977	303.0	- 1.37	- 0.002	0.539	455.0
	20BC–80AC	33.81	40.31	0.976	302.0	- 3.86	- 0.004	0.939	454.0
F1	80BC–20AC	28.58	5.26	0.969	305.0	22.91	1.17	0.968	459.0
	60BC–40AC	32.83	25.03	0.971	304.0	14.81	0.36	0.952	453.2
	40BC–60AC	35.66	64.91	0.978	303.0	5.21	0.03	0.963	455.0
	20BC–80AC	37.19	106.42	0.976	302.0	2.13	0.009	0.876	454.0
F3/2	80BC–20AC	29.41	6.71	0.968	305.0	28.00	3.81	0.969	459.0
	60BC–40AC	34.38	39.10	0.968	304.0	22.92	2.72	0.977	453.2
	40BC–60AC	38.03	127.50	0.977	303.0	11.60	0.26	0.995	455.0
	20BC–80AC	39.95	233.87	0.974	302.0	8.12	0.13	0.994	454.0
F2	80BC–20AC	30.26	8.60	0.966	305.0	33.55	13.28	0.968	459.0
	60BC–40AC	35.98	62.05	0.965	304.0	32.40	24.29	0.985	453.2
	40BC–60AC	40.54	259.50	0.975	303.0	19.20	2.05	0.996	455.0
	20BC–80AC	42.92	540.32	0.971	302.0	15.33	1.13	0.997	454.0
F3	80BC–20AC	32.01	14.29	0.963	305.0	46.02	197.51	0.965	459.0
	60BC–40AC	39.38	163.59	0.958	304.0	54.81	3084.78	0.989	453.2
	40BC–60AC	45.99	1191.19	0.968	303.0	37.33	160.10	0.994	455.0
	20BC–80AC	49.41	3320.23	0.960	302.0	32.66	97.55	0.996	454.0
F4	80BC–20AC	33.83	24.14	0.960	305.0	60.12	3755.94	0.962	459.0
	60BC–40AC	43.02	457.37	0.949	304.0	80.50	624778.90	0.988	453.2

	40BC–60AC	51.95	6203.30	0.959	303.0	58.08	16666.15	0.993	455.0
	20BC–80AC	56.59	24120.40	0.946	302.0	52.36	10360.43	0.996	454.0
R1	80BC–20AC	26.97	3.28	0.971	305.0	14.20	0.13	0.954	459.0
	60BC–40AC	29.94	10.75	0.975	304.0	2.78	0.006	0.454	453.2
	40BC–60AC	31.35	18.77	0.976	303.0	- 3.87	- 0.003	0.897	455.0
	20BC–80AC	32.25	25.66	0.975	302.0	- 6.05	- 0.004	0.973	454.0
R2	80BC–20AC	27.77	2.07	0.970	305.0	18.32	0.19	0.964	459.0
	60BC–40AC	31.36	8.14	0.973	304.0	8.11	0.03	0.865	453.2
	40BC–60AC	33.43	17.14	0.978	303.0	0.07	6.58×10^{-5}	0.003	455.0
	20BC–80AC	34.62	25.48	0.976	302.0	- 2.57	- 0.002	0.879	454.0
R3	80BC–20AC	28.04	1.50	0.969	305.0	19.79	0.18	0.966	459.0
	60BC–40AC	31.84	6.25	0.973	304.0	10.19	0.03	0.908	453.2
	40BC–60AC	34.16	14.08	0.978	303.0	1.64	0.001	0.665	455.0
	20BC–80AC	35.45	21.59	0.976	302.0	- 1.15	- 0.0007	0.613	454.0
P2	80BC–20AC	9.07	0.08	0.943	305.0	1.02	0.002	0.296	459.0
	60BC–40AC	10.59	0.15	0.955	304.0	- 4.89	- 0.004	0.889	453.2
	40BC–60AC	11.24	0.21	0.951	303.0	- 8.34	- 0.004	0.989	455.0
	20BC–80AC	11.72	0.25	0.952	302.0	- 9.40	- 0.004	0.994	454.0
P3	80BC–20AC	3.10	0.01	0.826	305.0	- 3.38	- 0.003	0.909	459.0
	60BC–40AC	4.14	0.02	0.887	304.0	- 7.44	- 0.004	0.971	453.2
	40BC–60AC	4.54	0.03	0.870	303.0	- 9.83	- 0.004	0.995	455.0
	20BC–80AC	4.88	0.03	0.879	302.0	- 10.52	- 0.004	0.997	454.0
P4	80BC–20AC	0.12	0.0002	0.013	305.0	- 5.57	- 0.004	0.978	459.0
	60BC–40AC	0.92	0.003	0.418	304.0	- 8.72	- 0.004	0.985	453.2
	40BC–60AC	1.19	0.004	0.430	303.0	- 10.58	- 0.004	0.996	455.0
	20BC–80AC	1.45	0.005	0.518	302.0	- 11.07	- 0.004	0.997	454.0

D1	80BC–20AC	62.79	1628.24	0.977	305.0	40.56	11.55	0.977	459.0
	60BC–40AC	68.64	15328.85	0.980	304.0	18.12	0.29	0.910	453.2
	40BC–60AC	71.58	45613.99	0.982	303.0	5.08	0.01	0.842	455.0
	20BC–80AC	73.32	81632.48	0.980	302.0	0.65	0.0008	0.145	454.0
D2	80BC–20AC	63.83	1085.64	0.977	305.0	45.76	18.16	0.978	459.0
	60BC–40AC	70.48	12731.96	0.979	304.0	24.50	0.72	0.943	453.2
	40BC–60AC	74.26	47402.30	0.982	303.0	9.67	0.03	0.952	455.0
	20BC–80AC	76.35	93579.64	0.981	302.0	4.63	0.008	0.894	454.0
D3	80BC–20AC	64.91	324.34	0.976	305.0	51.75	14.69	0.979	459.0
	60BC–40AC	72.44	4834.10	0.978	304.0	32.93	1.18	0.966	453.2
	40BC–60AC	77.19	23316.25	0.982	303.0	16.10	0.05	0.986	455.0
	20BC–80AC	79.72	51974.59	0.981	302.0	10.45	0.02	0.982	454.0
D4	80BC–20AC	64.19	266.28	0.976	305.0	47.75	6.21	0.979	459.0
	60BC–40AC	71.13	3382.17	0.978	304.0	27.24	0.31	0.953	453.2
	40BC–60AC	75.23	13723.45	0.982	303.0	11.77	0.01	0.969	455.0
	20BC–80AC	77.47	28203.93	0.981	302.0	6.52	0.004	0.947	454.0
A2	80BC–20AC	9.87	0.10	0.943	305.0	5.37	0.02	0.876	459.0
	60BC–40AC	12.04	0.25	0.953	304.0	1.13	0.003	0.278	453.2
	40BC–60AC	13.40	0.43	0.963	303.0	- 3.80	- 0.005	0.967	455.0
	20BC–80AC	14.19	0.57	0.961	302.0	- 5.31	- 0.006	0.987	454.0
A3	80BC–20AC	3.64	0.01	0.847	305.0	- 0.47	- 0.0008	0.114	459.0
	60BC–40AC	5.11	0.03	0.901	304.0	- 3.43	- 0.004	0.870	453.2
	40BC–60AC	5.98	0.05	0.921	303.0	- 6.81	- 0.005	0.992	455.0
	20BC–80AC	6.52	0.06	0.924	302.0	- 7.80	- 0.005	0.995	454.0

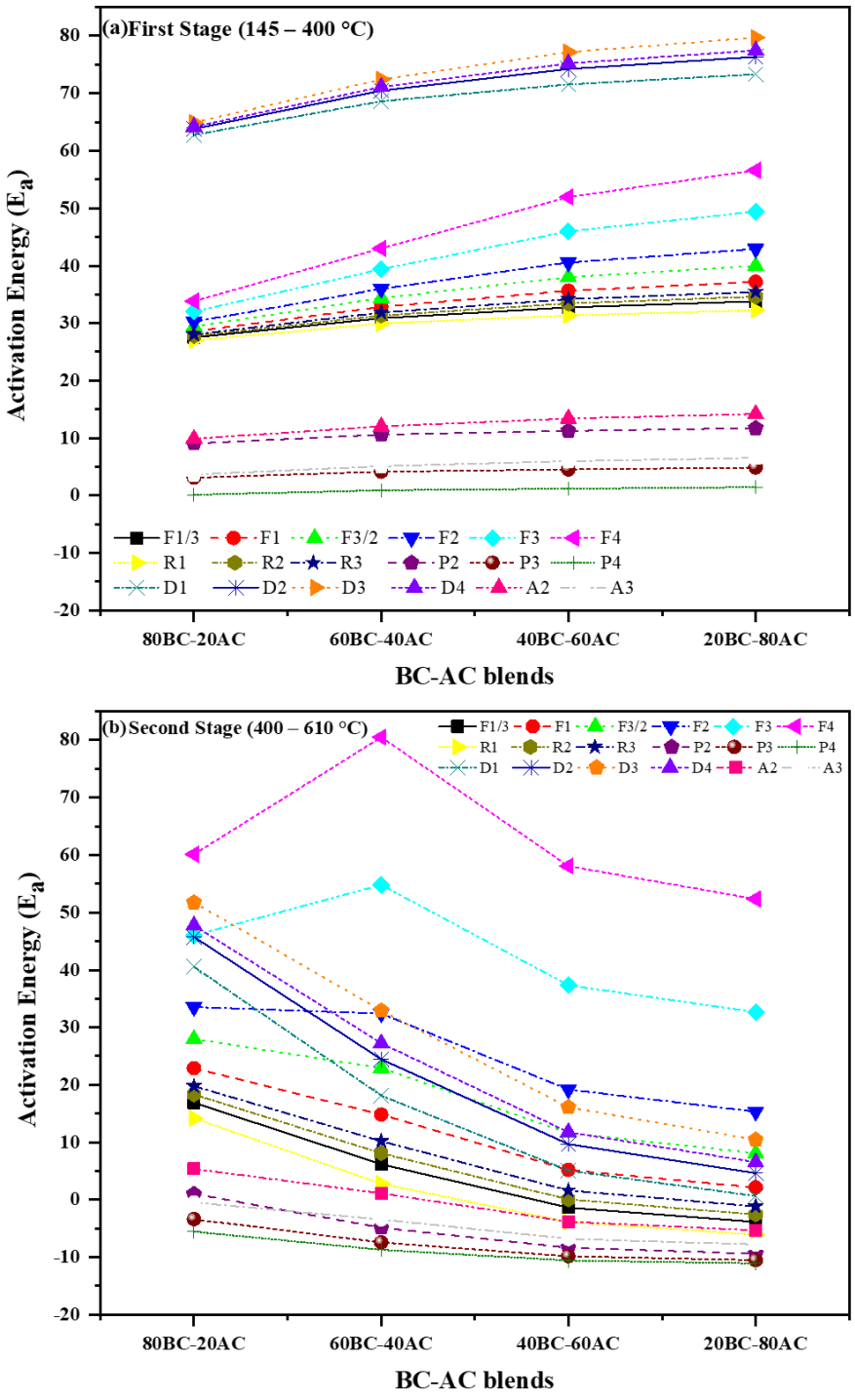

Fig. 4.7 Activation energy (Ea) for different models of BC-AC blends (a) First Stage (b) Second Stage

4.2.2 Thermodynamic parameters

The thermodynamic parameters such as the change in enthalpy (ΔH), change in Gibbs free energy (ΔG), and change in entropy (ΔS) are important factors for establishing the engineering tools for the co-pyrolysis of 100%BC, 100%AC, and their blends. These parameters were measured through T_p obtained from DTG analysis for each stage as displayed in Table 4.4 and Table 4.5. The thermodynamic parameters provide important information about the conversion of biomass into biofuels [33]. ΔH depicted endothermic and exothermic behavior of reaction mechanisms. ΔG provides information about the increase in the overall energy of the system as the reactants are consumed and activated complexes are created. The low ΔS indicated that the solid material was subjected to a variety of chemical and physical processes while in its thermodynamic equilibrium condition. [47]. The thermodynamic parameters of 100%BC and 100%AC as a single-stage process with an individual ΔH, ΔG, and ΔS for all the eighteen reaction mechanisms. The results for the parent sample's thermodynamic parameters are displayed in Table 4.4.

For 100%BC, from 338 – 600 °C the values of ΔH were positive for all the reaction mechanisms. The best model was the F3 model having an enthalpy of 78.99 $\mathrm{kJ/mol}$ as shown in Fig. 4.8(a). For 100%AC, from 145 – 425.8 °C the values of ΔH were also positive. The D3 was the best model having an enthalpy of 73.44 $\mathrm{kJ/mol}$ as shown in Fig. 4.8(a). The positive values of ΔH show that the entire co-pyrolysis process is endothermic [33]. However, the variation between E_a and ΔH was in the range of 4-6.5 $\mathrm{kJ/mol}$ for both 100%BC and 100%AC in the single stage which indicates the reaction was possible to produce because of the small potential energy barrier [48, 49]. For 100%BC the values of ΔH were higher than that of 100%AC. A higher value of ΔH indicates that decomposition process requires a higher amount of energy to break the bonds of the reactant sample [50].

For 100%BC, from 338 – 600 °C the values of ΔG were positive for all the reaction mechanisms. The best model was the F3 model having ΔG of 197.10 $\mathrm{kJ/mol}$ as shown in Fig. 4.8(b). For 100%AC, from 145 – 425.8 °C the values of ΔG were positive. The best model was D3 having ΔG of 170.70 $\mathrm{kJ/mol}$ as shown in Fig. 4.8(b). ΔG always has a positive value during the whole process for both 100%BC and 100%AC in the single-stage, indicating that the reaction is non-spontaneous and so requires external heat [51].

For 100%BC, from 338 – 600 °C the values of ΔS were negative for all the reaction mechanisms. The best model was the F3 model having an entropy of $-0.16\,\mathrm{kJ/mol.k}$. For 100%AC, from 145 – 425.8 °C the values of ΔS were negative. D3 was the best model having an entropy of $-0.17\,\mathrm{kJ/mol.k}$. When compared to the preliminary constituent, the activated complex of 100%BC and 100%AC had a more ordered structure, and the co-pyrolysis process involved chaotic structure to a well-ordered structure, furthermore, this indicated that the samples had undergone decomposition and will soon reach their thermodynamic equilibrium [50].

Table 4.4 Represents the Thermodynamic parameters of Pure BC and AC at different temperature stages

		Temperature Range		Thermodynamic Parameters		
Symbols	**Sample Name**	**1st Stage**	**T_P (°C)**	**ΔH (kJ/mol)**	**ΔG (kJ/mol)**	**ΔS (kJ/mol K)**
F1/3	100%BC	(338 – 600 °C)	455.0	40.11	205.53	- 0.23
	100%AC	(145 – 425.8 °C)	301.0	27.70	159.71	- 0.23
F1	100%BC	(338 – 600 °C)	455.0	48.12	203.54	- 0.21
	100%AC	(145 – 425.8 °C)	301.0	32.17	158.06	- 0.22
F3/2	100%BC	(338 – 600 °C)	455.0	54.90	201.99	- 0.20
	100%AC	(145 – 425.8 °C)	301.0	35.97	156.74	- 0.21
F2	100%BC	(338 – 600 °C)	455.0	62.33	200.39	- 0.19
	100%AC	(145 – 425.8 °C)	301.0	40.13	155.34	- 0.20
F3	100%BC	(338 – 600 °C)	455.0	78.99	197.10	- 0.16
	100%AC	(145 – 425.8 °C)	301.0	49.48	152.37	- 0.18
F4	100%BC	(338 – 600 °C)	455.0	97.69	193.73	- 0.13
	100%AC	(145 – 425.8 °C)	301.0	59.96	149.23	- 0.16
R1	100%BC	(338 – 600 °C)	455.0	36.53	206.50	- 0.23
	100%AC	(145 – 425.8 °C)	301.0	25.71	160.45	- 0.23
R2	100%BC	(338 – 600 °C)	455.0	42.00	209.24	- 0.23
	100%AC	(145 – 425.8 °C)	301.0	28.75	162.62	- 0.23
R3	100%BC	(338 – 600 °C)	455.0	43.97	211.20	- 0.23
	100%AC	(145 – 425.8 °C)	301.0	29.85	164.15	- 0.23
P2	100%BC	(338 – 600 °C)	455.0	9.17	208.45	- 0.27
	100%AC	(145 – 425.8 °C)	301.0	5.98	162.37	- 0.27
P3	100%BC	(338 – 600 °C)	455.0	0.05	212.56	- 0.29

	100%AC	(145 – 425.8 °C)	301.0	-0.59	165.85	- 0.29
P4	100%BC	(338 – 600 °C)	455.0	-4.51	220.17	- 0.31
	100%AC	(145 – 425.8 °C)	301.0	-3.88	172.71	- 0.31
D1	100%BC	(338 – 600 °C)	455.0	91.30	210.03	- 0.16
	100%AC	(145 – 425.8 °C)	301.0	65.16	162.68	- 0.17
D2	100%BC	(338 – 600 °C)	455.0	98.16	212.90	- 0.16
	100%AC	(145 – 425.8 °C)	301.0	69.00	164.83	- 0.16
D3	100%BC	(338 – 600 °C)	455.0	106.13	220.53	- 0.16
	100%AC	(145 – 425.8 °C)	301.0	73.44	170.70	- 0.17
D4	100%BC	(338 – 600 °C)	455.0	100.80	221.51	- 0.17
	100%AC	(145 – 425.8 °C)	301.0	70.47	171.60	- 0.18
A2	100%BC	(338 – 600 °C)	455.0	14.96	205.75	- 0.26
	100%AC	(145 – 425.8 °C)	301.0	9.21	160.37	- 0.26
A3	100%BC	(338 – 600 °C)	455.0	3.91	209.10	- 0.28
	100%AC	(145 – 425.8 °C)	301.0	1.56	163.40	- 0.28

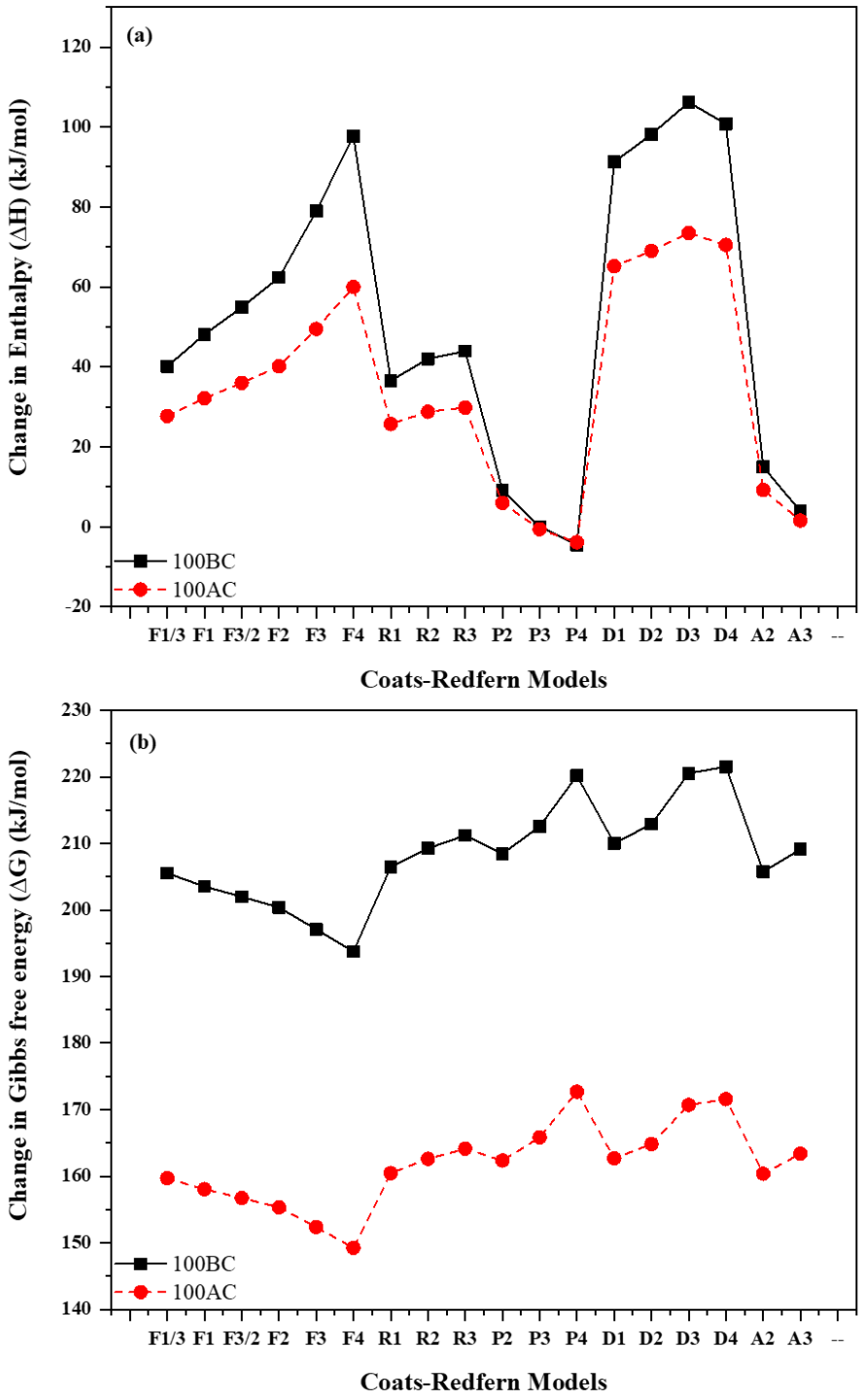

Fig. 4.8 Thermodynamic parameters for different models of pure bituminous coal and algae consortium (a) change in enthalpy (ΔH) (b) change in Gibbs free energy (ΔG)

The thermodynamic parameters of the four (BC-AC) blends can be considered as a two-stage process with an individual ΔH,ΔG, and ΔS for all the eighteen reaction mechanisms. The temperature ranges for the two stages were 145 – 400 °C for the first stage and from 400 – 610 °C for the second stage. The results for the four (BC-AC) blend thermodynamic parameters are displayed in Table 4.5.

In the first stage from 145 – 400 °C, for the (80BC-20AC) blend, the values of ΔH and ΔG were positive and the values of ΔS were negative for all the reaction mechanisms. The best model was the D1 model having an enthalpy of 57.98 kJ/mol as shown in Fig. 4.9(a). The value of ΔG for the best model was 172.02 kJ/mol as depicted in Fig. 4.10(a). The value of ΔS for the best model D1 was -0.20 kJ/mol. k. The values of ΔH and ΔG were positive and the values of ΔS were negative for all the reaction mechanisms of (60BC-40AC) blend. The best model D1 had an enthalpy of 63.84 kJ/mol as shown in Fig. 4.9(a) and the value of ΔG was 166.92 kJ/mol as depicted in Fig. 4.10(a). The value of ΔS for the best model D1 was -0.18 kJ/mol. k. For (40BC-60AC), ΔH and ΔG values were positive and the values of ΔS were negative for all the reaction mechanisms. The D1 model was the best having an enthalpy of 66.79 kJ/mol as shown in Fig. 4.9(a). The value of ΔG for the best model D1 was 164.50 kJ/mol as depicted in Fig. 4.10(a) and the value of ΔS was -0.17 kJ/mol. k. For (20BC-80AC) the values of ΔH and ΔG were positive while the values of ΔS were negative for all the reaction mechanisms. The best model for (20BC-80AC) was D2 with an enthalpy of 71.57 kJ/mol as shown in Fig. 4.9(a) and the value of ΔG was 165.62 kJ/mol as depicted in Fig. 4.10(a). The value of ΔS was found to be -0.16 kJ/mol. k.

In the second stage from 400 – 610 °C, for (80BC-20AC) the values of ΔH and ΔG were positive and the values of ΔS were negative for all the reaction mechanisms. The best model was the D4 model having an enthalpy of 41.66 kJ/mol as shown in Fig. 4.9(b). The value of ΔG was 221.41 kJ/mol as depicted in Fig. 4.10(b) and the value of ΔS was -0.25 kJ/mol. k. For (60BC-40AC) the values of ΔH were positive for all the reaction mechanisms and the best model was F3 having an enthalpy of 48.77 kJ/mol as shown in Fig. 4.9(b). The values of ΔG were positive and the value of ΔG for the best model was 189.60 kJ/mol as depicted in Fig. 4.10(b). The values of ΔS were negative. The value of ΔS for the best model F3 was -0.19 kJ/mol. k. The values of ΔH and ΔG were positive while the values of ΔS were negative for all the reaction mechanisms of

(40BC-60AC). The best model was the F2 model having an enthalpy of 13.14 $\mathrm{kJ/mol}$ as shown in Fig. 4.9(b) and the value of ΔG for the best model was 198.60 $\mathrm{kJ/mol}$ as depicted in Fig. 4.10(b). The value of ΔS was found to be $-0.25\ \mathrm{kJ/mol.k}$. ΔH and ΔG values were positive and the values of ΔS were negative for all the reaction mechanisms of (20BC-80AC). The best model was F2 with an enthalpy of 9.29 $\mathrm{kJ/mol}$ as shown in Fig. 4.9(b). The value of ΔG was found to be 198.06 $\mathrm{kJ/mol}$ as depicted in Fig. 4.10(b). The value of ΔS was $(-0.26\ \mathrm{kJ/mol.k})$.

The positive value of ΔH for the four blends showed that the entire co-pyrolysis process was endothermic, requiring external heat to convert them into valuable bio-energy [33, 48]. The ΔH followed the same pattern as E_a increased by increasing the ratio of AC in the blends during the first stage, while for the second stage ΔH decreased by increasing the ratio of AC in the blends except for F3 and F4 models. However, the variation between E_a and ΔH was in the range of 4-6.5 $\mathrm{kJ/mol}$ for all the blends in both the first and second stage indicating the reaction was likely to produce because of the small potential energy barrier [48, 49]. A higher value of ΔH indicates that the decomposition process requires a higher amount of energy to break the bonds of the reactant sample [50]. ΔG always has a positive value during the whole process for all the four blends in both stages, indicating that the reaction is non-spontaneous and complex requiring external heat to speed up the reaction [51]. In the first stage the values of ΔG decrease for all the blends as the ratio of AC increases, whereas in the second stage the value of ΔG increases and decreases both for some models applied on the (BC-AC) blends. The activated complex can be classified by a highly developed "degree of arrangement," as indicated by the negative values of ΔS of the formation [49]. The positive value of ΔS indicated that the system's active complex was in a disordered state, departing from thermodynamic equilibrium, and the negative value of ΔS shows how close the system is to reaching its thermodynamic equilibrium, indicating that a thermal product is produced [52]. The Optimum blend (20BC-80AC) showed lowest values of ΔH and ΔG thus lowering it for 100%BC and 100%AC, lower the value of ΔG so it requires less energy to form an activated complex, also the negative value of ΔS for optimum blend is higher.

Table 4.5 Represents the Thermodynamic parameters of the four (BC–AC) Blends at different temperature stages

		1st Stage (145 – 400 °C)			2nd Stage (400 – 610 °C)		
Symbols	**Sample Name**	ΔH (kJ/mol)	ΔG (kJ/mol)	ΔS (kJ/mol K)	ΔH (kJ/mol)	ΔG (kJ/mol)	ΔS (kJ/mol K)
F1/3	80BC–20AC	22.70	165.83	- 0.25	10.80	209.73	- 0.27
	60BC–40AC	26.10	162.70	- 0.24	0.15	211.41	- 0.29
	40BC–60AC	27.93	161.04	- 0.23	- 7.43	Nil	Nil
	20BC–80AC	29.03	160.14	- 0.23	- 9.91	Nil	Nil
F1	80BC–20AC	23.78	165.40	- 0.24	16.82	206.75	- 0.26
	60BC–40AC	28.04	161.90	- 0.23	8.77	204.31	- 0.27
	40BC–60AC	30.87	159.93	- 0.22	- 0.85	210.13	- 0.29
	20BC–80AC	32.40	158.87	- 0.22	- 3.92	214.30	- 0.30
F3/2	80BC–20AC	24.61	165.04	- 0.24	21.90	204.63	- 0.25
	60BC–40AC	29.58	161.31	- 0.23	16.88	200.15	- 0.25
	40BC–60AC	33.24	159.07	- 0.22	5.55	203.54	- 0.27
	20BC–80AC	35.17	157.87	- 0.21	2.07	204.15	- 0.28
F2	80BC–20AC	25.46	164.70	- 0.24	27.46	202.58	- 0.24
	60BC–40AC	31.18	160.70	- 0.22	26.36	196.40	- 0.23
	40BC–60AC	35.75	158.18	- 0.21	13.14	198.60	- 0.25
	20BC–80AC	38.13	156.83	- 0.21	9.29	198.06	- 0.26
F3	80BC–20AC	27.21	164.00	- 0.24	39.93	198.63	- 0.22
	60BC–40AC	34.58	159.44	- 0.22	48.77	189.60	- 0.19
	40BC–60AC	41.20	156.32	- 0.20	31.28	190.35	- 0.22
	20BC–80AC	44.63	154.65	- 0.19	26.62	188.45	- 0.22
F4	80BC–20AC	29.02	163.31	- 0.23	54.03	194.80	- 0.19

	60BC–40AC	38.22	158.14	- 0.21	74.46	183.20	- 0.15
	40BC–60AC	47.16	154.38	- 0.19	52.02	182.96	- 0.18
	20BC–80AC	51.81	152.34	- 0.17	46.31	179.94	- 0.18
R1	80BC–20AC	22.17	166.05	- 0.25	8.11	211.31	- 0.28
	60BC–40AC	25.14	163.10	- 0.24	- 3.26	217.10	- 0.30
	40BC–60AC	26.56	161.57	- 0.23	- 9.92	Nil	Nil
	20BC–80AC	27.47	160.74	- 0.23	- 12.10	Nil	Nil
R2	80BC–20AC	22.96	169.05	- 0.25	12.23	213.18	- 0.27
	60BC–40AC	26.60	165.82	- 0.24	2.07	213.52	- 0.29
	40BC–60AC	28.64	164.09	- 0.24	- 5.98	242.10	- 0.34
	20BC–80AC	29.84	163.14	- 0.23	- 8 .62	Nil	Nil
R3	80BC–20AC	23.23	170.88	- 0.26	13.71	214.90	- 0.27
	60BC–40AC	27.04	167.60	- 0.24	4.15	214.15	- 0.29
	40BC–60AC	29.37	165.75	- 0.24	- 4.41	224.84	- 0.31
	20BC–80AC	30.67	164.77	- 0.23	- 7.20	Nil	Nil
P2	80BC–20AC	4.26	166.30	- 0.28	- 5.07	224.60	- 0.31
	60BC–40AC	5.79	164.13	- 0.27	- 10.92	Nil	Nil
	40BC–60AC	6.45	163.07	- 0.27	- 14.40	Nil	Nil
	20BC–80AC	6.94	162.37	- 0.27	- 15.44	Nil	Nil
P3	80BC–20AC	- 1.70	169.80	- 0.30	- 9.46	Nil	Nil
	60BC–40AC	- 0.66	167.33	- 0.29	- 13.50	Nil	Nil
	40BC–60AC	- 0.25	166.30	- 0.29	- 15.89	Nil	Nil
	20BC–80AC	0.09	165.49	- 0.29	- 16.60	Nil	Nil
P4	80BC–20AC	- 4.69	184.60	- 0.33	- 11.66	Nil	Nil
	60BC–40AC	- 3.88	173.91	- 0.31	- 14.76	Nil	Nil
	40BC–60AC	- 3.60	172.12	- 0.31	- 16.63	Nil	Nil

	20BC–80AC	- 3.33	170.74	- 0.30	- 17.12	Nil	Nil
D1	80BC–20AC	57.98	172.02	- 0.20	34.48	210.50	- 0.24
	60BC–40AC	63.84	166.92	- 0.18	12.08	208.96	- 0.27
	40BC–60AC	66.79	164.50	- 0.17	- 0.97	215.83	- 0.30
	20BC–80AC	68.54	163.24	- 0.16	- 5.40	226.91	- 0.32
D2	80BC–20AC	59.02	175.01	- 0.20	39.67	212.90	- 0.24
	60BC–40AC	65.68	169.65	- 0.18	18.42	209.72	- 0.26
	40BC–60AC	69.47	166.95	- 0.17	3.62	214.31	- 0.29
	20BC–80AC	71.57	165.62	- 0.16	- 1.42	217.21	- 0.30
D3	80BC–20AC	60.10	181.90	- 0.21	45.66	220.18	- 0.24
	60BC–40AC	67.64	176.30	- 0.19	26.90	215.19	- 0.26
	40BC–60AC	72.40	173.30	- 0.18	10.05	218.30	- 0.29
	20BC–80AC	74.94	171.80	- 0.17	4.40	219.00	- 0.30
D4	80BC–20AC	59.38	182.13	- 0.21	41.66	221.41	- 0.25
	60BC–40AC	66.34	176.66	- 0.19	21.20	217.55	- 0.27
	40BC–60AC	70.44	173.90	- 0.18	5.72	221.53	- 0.30
	20BC–80AC	72.69	172.48	- 0.17	0.48	223.44	- 0.31
A2	80BC–20AC	5.07	165.67	- 0.28	- 0.71	213.64	- 0.29
	60BC–40AC	7.24	163.20	- 0.27	- 4.91	219.58	- 0.31
	40BC–60AC	8.61	161.72	- 0.27	- 9.86	Nil	Nil
	20BC–80AC	9.41	160.86	- 0.26	- 11.36	Nil	Nil
A3	80BC–20AC	- 1.17	168.90	- 0.29	- 6.56	Nil	Nil
	60BC–40AC	0.31	166.10	- 0.29	- 9.47	Nil	Nil
	40BC–60AC	1.19	164.62	- 0.28	- 12.86	Nil	Nil
	20BC–80AC	1.74	163.70	- 0.28	- 13.84	Nil	Nil

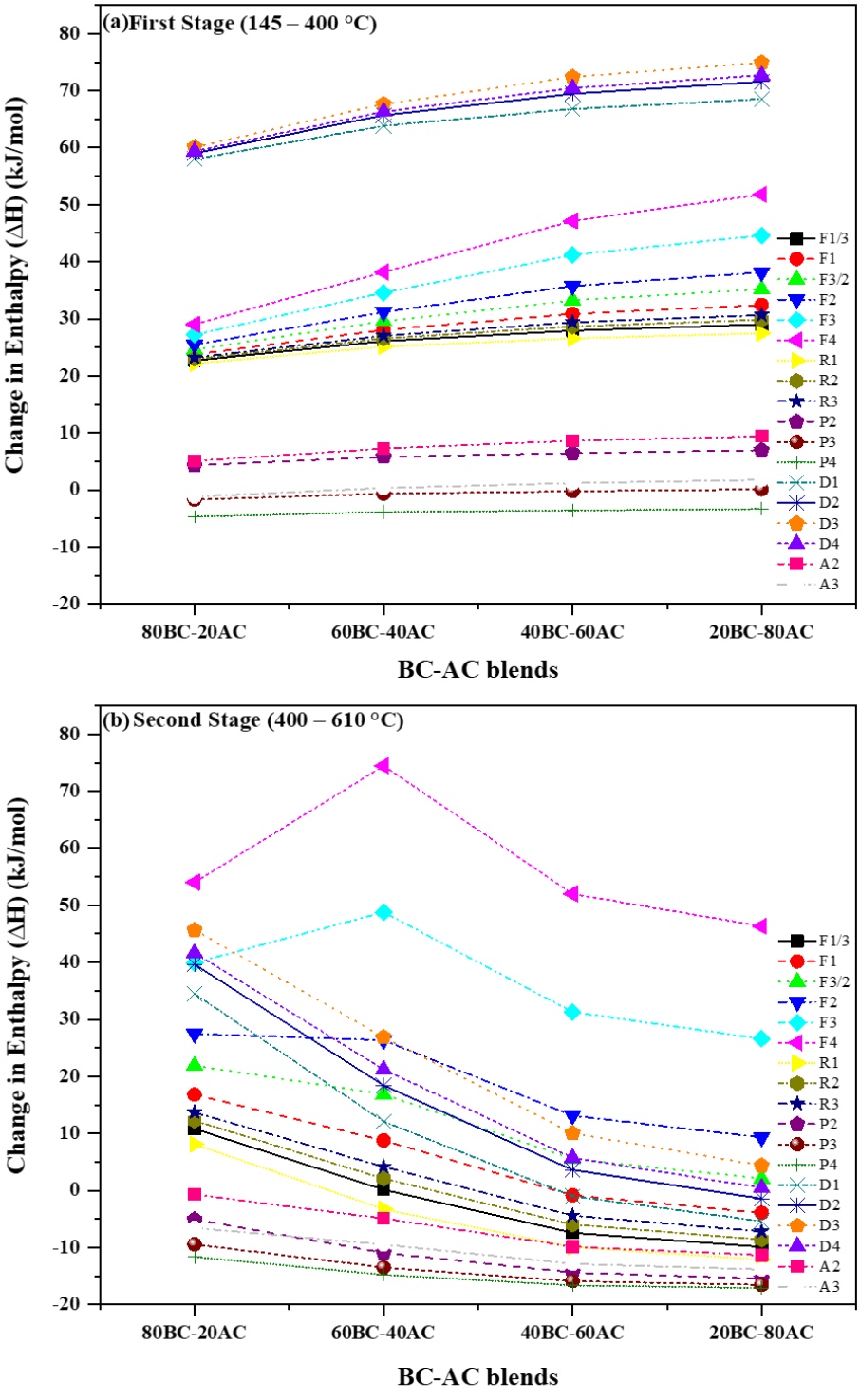

Fig. 4.9 Enthalpy for different models of blends (a) (ΔH) in the first stage and (b) (ΔH) in the second stage

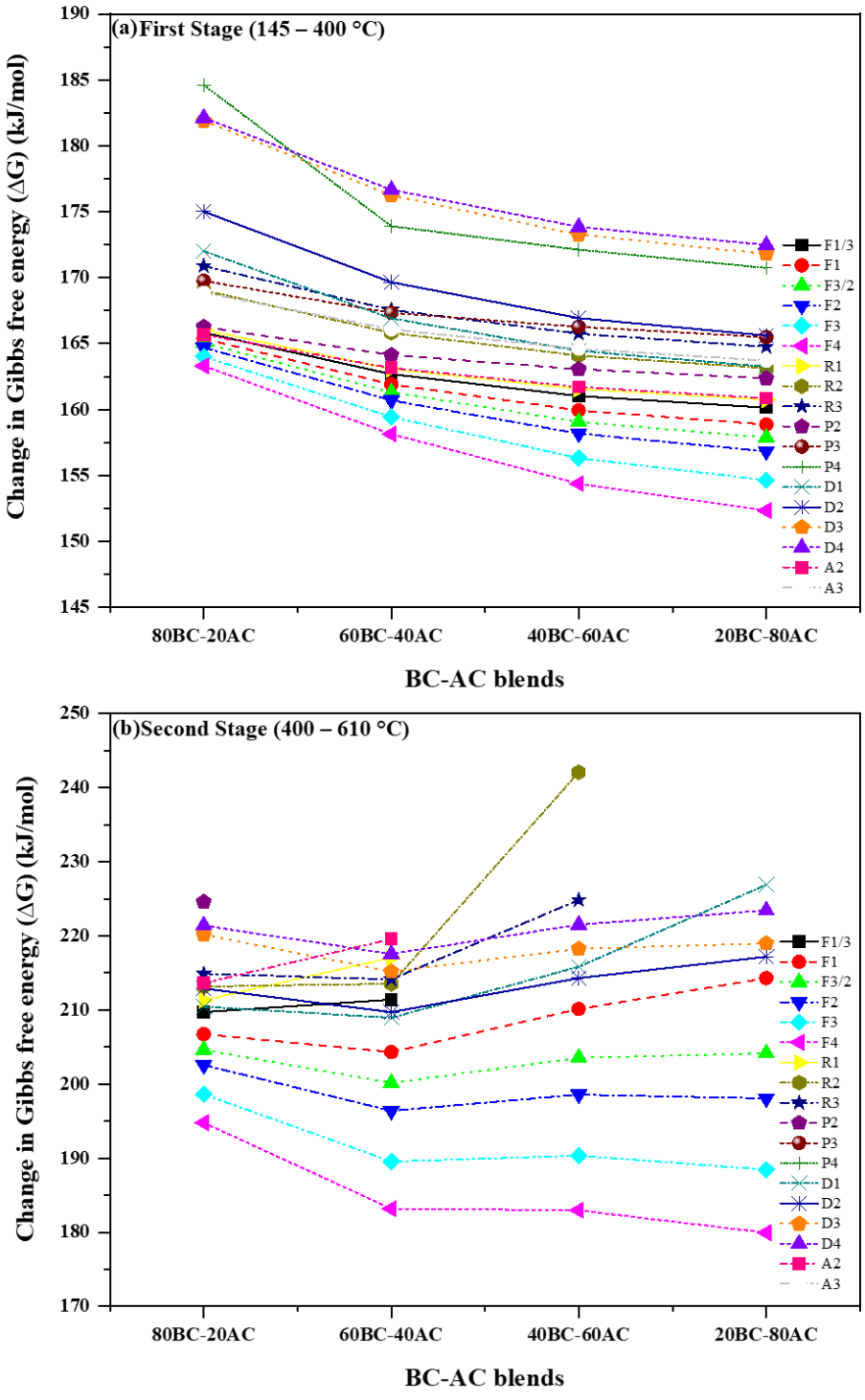

Fig. 4.10 Gibbs free energy for different models of BC-AC blends (a) (ΔG) in First Stage (b) (ΔG) in Second Stage

4.3 Catalytic co-pyrolysis

4.3.1 Characterization of CeO_2@MNA

The detailed characterization for 10%CeO_2@MNA is already reported in the research literature [53]. Briefly, the fully crystalline CeO_2 loaded MNA shows diffraction peaks for cubical structure $NiAl_2O_4$ (PDF# 10-0339), CeO_2 (PDF# 43-1002), $MgAl_2O_4$ (PDF# 21-1152), NiO (PDF# 44-1159) and $MgNiO_2$ (PDF#24-0712). The metal interaction was verified using FTIR spectra. The peaks in a range of 850–600 cm^{-1} are inferred as lattice vibrations of Mg-O, Ni-O, and Al-O. It depicts the interaction between metal and support is significant. The stability analysis shows the 10%CeO_2@MNA is stable up to 900 °C. The SEM micrographs show the interaction of CeO_2 over the coral surfaces of MNA maintaining the coral like structure of MNA.

4.3.2 TGA/DTG analysis in a catalytic environment

The catalytic co-pyrolysis of the optimum blend (20BC-80AC) over CeO_2@MNA catalyst was performed using TGA 5500 (TA Instruments, USA). The thermal decomposition behavior of the catalytic co-pyrolysis blends is represented as 0wt.%, 3wt.%, and 5wt.% CeO_2@MNA loading was examined in TG-DTG profiles as shown in Fig. 4.11(a,b) at a constant heating rate of 20 °C/min.

The TGA profile of optimum blend with 0wt.%, 3wt.%, and 5wt.% CeO_2@MNA loading was shown in Fig. 4.11(a), showing four stages of thermal reaction. The first stage represents dehydration, whereas the second and third stages depict devolatilization, and the fourth stage illustrates the slow decomposition of the solid residue. The temperature range for the first stage was 25 – 150 °C where slight WL% occurs due to moisture evaporation. The temperature range for the second stage was 150 – 430 °C where significant WL% can be seen indicating the decomposition of constituents of 100%AC. The temperature range for the third stage was 430 – 660 °C in which WL% was also seen indicating the decomposition of the primary constituents of 100%BC in the blend degrading into volatiles. A small peak was also specified in the fourth stage in the temperature range of 660 – 900 °C where the WL% was very low at a higher temperature, which is mainly attributed to the carbonaceous residues, the naturally existing minerals, and the line becomes straight.

In Fig. 4.11(b) the DTG profiles of optimum blend with various CeO_2@MNA loading were discussed illustrating a major DTG curve peak in each of the four stages for the catalytic co-pyrolysis. In co-pyrolysis without any catalyst loading or 0wt.% loading, the T_p in the first stage, at which maximum WL% occurs was 84.6 °C and (wt. %/min) observed was -0.83%/min. Whereas the T_p in the second and third stages was 309 °C and 466.3 °C and (wt. %/min) found was -4.96%/min and -1.04%/min respectively with multiple peaks representing the decomposition of low volatile components. A smaller peak was also observed in the fourth stage with T_p of 683.9 °C and (wt. %/min) was -1.52%/min. In comparison to the co-pyrolysis performed at a constant heating rate of 10 °C/min, the T_p shifted towards the right, and (wt. %/min) in all stages increased as the heating rate increased. The WL% for (20BC-80AC) at the end of the process was 45.9% and the RL% was 54.1%. In 3wt.% loading, the T_p in the first stage was 70.9 °C, and (wt. %/min) was -0.94%/min. The second and third stages are the main decomposition regions where the T_p was 302.3 °C and 526.9 °C and (wt. %/min) witnessed was -5.32%/min and -4.44%/min correspondingly with multiple peaks demonstrating the degradation of low volatile components. In the fourth stage, a smaller peak was found with a T_p of 676.5 °C, and (wt. %/min) was -1.32%/min. As it can be seen from the DTG graphs so in 3wt.% loading, the addition of catalyst loading to optimum blend the T_p in the second stage was slightly shifted to the left, thus lowering the T_p from 309 °C to 302 °C indicating the decomposition of 100%AC constituents including (carbohydrates, proteins, and lipids) at an earlier stage, whereas, in the third stage which depicts the decomposition of 100%BC, the T_p shifted towards right thus, catalyst addition increased drastically the temperature from 466.3 °C to 526.9 °C of the second pyrolysis region. Furthermore, in catalyst loading of 5wt.%, the T_p was 80 °C in the first stage, and (wt. %/min) was -0.84%/min. The T_p for the second and third stages was 311 °C and 467.5 °C and (wt. %/min) observed was -4.91%/min and -0.94%/min respectively, having multiple peaks representing the devolatilization of low volatile components. In the fourth stage, a smaller peak was also detected with a T_p of 688°C and (wt. %/min) was -1.72%/min, so the addition of 5% catalyst loading to optimum blend the T_p in the second and third stage slightly shifted towards the right, thus increasing the T_p from 309 °C to 311 °C and 466.3 °C to 467.5 °C respectively, indicating that the addition of an increased amount of catalyst the decomposition of 100%AC and 100%BC constituents occurs at a delayed temperature.

The excellent performance of the catalyst loading was observed for 3wt.%, which achieved the highest WL% of 68.7% compared to that of 46.7% in 5wt.%, and the WL% of 45.9% in 0wt.%. Thus, improving the bio-oil yield of the optimum blend. The RL% for 3wt.%, and 5wt.%, loading at the end was 31.3% and 53.3% respectively, improving the biochar yield for 5wt.%, The reduction in the T_p of the optimum blend for 3wt.% catalyst, could be attributed to the better dispersion of the catalyst. The addition of catalysts can increase product selectivity, reduce the requirements of reaction conditions, and improve the quality and characteristics of liquid fuel [54]. This highest WL% in 3wt.% may be attributed to the presence of CeO_2, which helps in breaking the constituents of 100%AC including (carbohydrates, proteins, and lipids) thus resulting in bio-oil containing low oxygen content [55], and on 100%BC is very complex because it helps in promoting the bond-breaking reaction of side-chain functional groups to generate hydrocarbons [56]. CeO_2 presence can help reduce the coke deposition by the decarbonylation reaction and consistently lower the nitrogen content of bio-oil [57]. On the other hand, the increased formation of hydrocarbons with reduced oxygenated and nitrogenous compounds is attributed to the presence of hydrotalcite (MNA), offering a lot of potential for catalytic co-pyrolysis since they have a lot of qualities including high dispersion, heat stability, and increased surface area which could be due to changes in the reaction kinetics, controlled by the catalytic activity of hydrotalcite [58]. Thus, with the addition of CeO_2 to hydrotalcite (MNA), the base to acid ratio was changed in the catalyst increasing the thermal stability of the catalyst used [53]. The reactivity of the catalyst starts to reduce when the percentage of the catalyst loading was further increased from 3wt.% to 5wt.% which is attributed to the higher catalyst mass loading that results in a high number of active acid sites on the catalyst which eventually results in catalyst deactivation and the formation of coke [59]. Based on the results of volatiles WL% from TGA profile and decomposition rate from DTG profiles, it can be concluded that the 3wt.% is the optimum catalytic blend ratio in achieving higher volatile yield in terms of bio-oil.

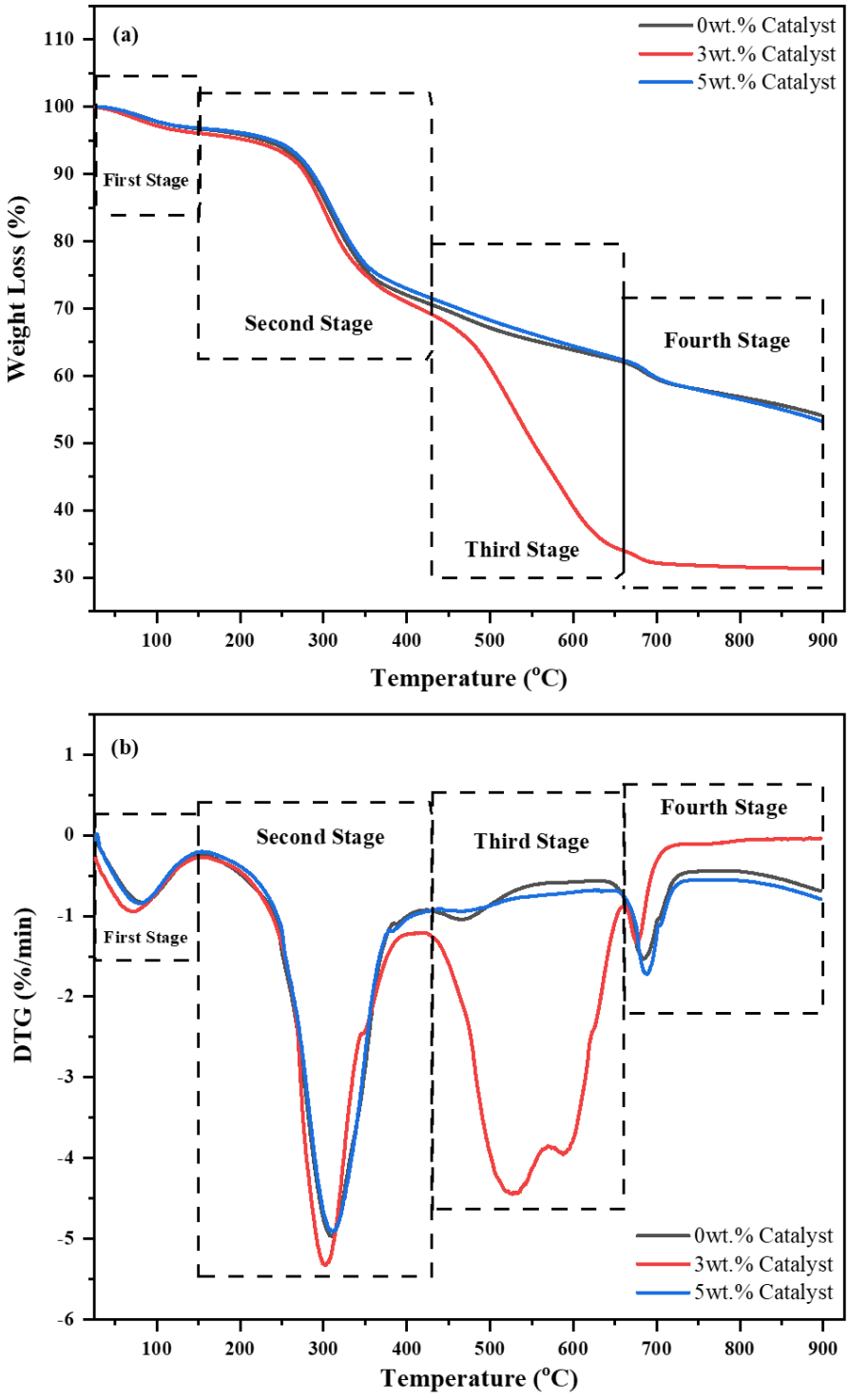

Fig. 4.11 TGA and DTG of catalytic co-pyrolysis of the optimum blend (a) TGA (b) DTG

4.3.3 Kinetics and thermodynamic parameters of catalytic co-pyrolysis

The kinetic and the thermodynamic analysis were calculated based on the data obtained from the TGA of the (0wt.%), (3wt.%), and (5wt.%) at a constant heating rate of 20 °C/min as displayed in Table 4.6 and Table 4.7. The precision of the fitting data was based on R^2 and the specified range was 0.90 to 0.99 as previously discussed.

The WL% in the process was considered as a two-stage process with individual kinetic parameters i.e. E_a, R^2, and A, and individual thermodynamic parameters i.e. ΔH, ΔG, and ΔS for all the eighteen reaction mechanisms in each stage. The first and second stages were the rapid decomposition zones, the first stage lies in a temperature range of 150 – 420 °C, while the second stage occurs in a temperature range of 420 – 660 °C. The results of the kinetic and thermodynamic analysis are displayed in Fig. 4.12(a, b), Fig. 4.13(a, b), and Fig. 4.14(a, b).

In the first stage from 150 – 420 °C, for (0wt.%), the best model was D4 with the highest R^2 value of 0.975 having an E_a of 72.48 kJ/mol and A of 14461.45 min^{-1} as shown in Fig. 4.12(a). The values of ΔH and ΔG were positive and the values of ΔS were negative for all the reaction mechanisms. The best model D4 had an enthalpy of 67.63 kJ/mol as shown in Fig. 4.13(a) and the value of ΔG was 172.11 kJ/mol as depicted in Fig. 4.14(a). The value of ΔS for the best model was $-0.18\ kJ/mol.\,k$. The best model was D2 in (3wt.%) with the highest R^2 value of 0.968 having an E_a of 67.82 kJ/mol with an A of 8736.33 min^{-1} as shown in Fig. 4.12(a). The values of ΔH and ΔG were positive while the values of ΔS were negative for all the reaction mechanisms. The best model had an enthalpy of 63.04 kJ/mol as shown in Fig. 4.13(a). The value of ΔG was found to be 168.48 kJ/mol as depicted in Fig. 4.14(a) and the value of ΔS for D2 was $-0.18\ kJ/mol.\,k$. In (5wt.%) the model with the highest R^2 value of 0.972 was D2 having an E_a of 75.23 kJ/mol and A of 91206.20 min^{-1} as shown in Fig. 4.12(a). ΔH and ΔG values were positive, while values of ΔS were negative for all the reaction mechanisms. The best model D2 with an enthalpy of 70.37 kJ/mol as shown in Fig. 4.13(a) and the value of ΔG was 166.10 kJ/mol as depicted in Fig. 4.14(a). The value of ΔS was found to be $-0.16\ kJ/mol.\,k$.

In the second stage from 420 – 660 °C, the best model was F2 for the (0wt.%) blend with the highest R^2 value of 0.998 having an E_a of 13.76 kJ/mol with an A of 1.35 min^{-1} as shown in Fig. 4.12(b). ΔH and ΔG values were positive and the values of ΔS were negative for all the reaction

mechanisms. The best model F2 had an enthalpy of 7.61 $\mathrm{kJ/mol}$ as shown in Fig. 4.13(b). The value of ΔG was 198.73 $\mathrm{kJ/mol}$ as depicted in Fig. 4.14(b) while the value of ΔS was $-0.26\ \mathrm{kJ/mol.\,k}$. For (3wt.%) the best model with the highest R^2 value of 0.980 was D2 having an E_a of 41.21 kJ/mol and A of 21.08 $\mathrm{min^{-1}}$ as shown in Fig. 4.12(b). The values of ΔH and ΔG were positive while the values ΔS were negative for all the reaction mechanisms. The best model D2 with an enthalpy of 34.56 $\mathrm{kJ/mol}$ as shown in Fig. 4.13(b) and the value of ΔG observed was 223.44 $\mathrm{kJ/mol}$ as depicted in Fig. 4.14(b). The value of ΔS was found to be $-0.24\ \mathrm{kJ/mol.\,k}$. In (5wt.%) the best model was D3 with the highest R^2 value of 0.999 having an E_a of 10.52 kJ/mol with an A of 0.02 $\mathrm{min^{-1}}$ as shown in Fig. 4.12(b). Positive values of ΔH and ΔG were observed and negative values for ΔS were detected for all the reaction mechanisms. An enthalpy of 4.36 $\mathrm{kJ/mol}$ was observed for the best model as shown in Fig. 4.13(b) and the value of ΔG was 130.65 $\mathrm{kJ/mol}$ as depicted in Fig. 4.14(b). The value of ΔS for the best model was $-0.17\ \mathrm{kJ/mol.\,k}$.

Table 4.6 Represents the Kinetic parameters of the Optimum Blend with two mass loadings at different temperature stages

		1st Stage (150 – 420 °C)				2nd Stage (420 – 660 °C)			
Symbols	**Sample Name**	**E_a (kJ/mol)**	**A (min^{-1})**	**R^2**	**T_P (°C)**	**E_a (kJ/mol)**	**A (min^{-1})**	**R^2**	**T_P (°C)**
F1/3	0wt.% Catalyst	31.22	38.23	0.967	310.0	- 4.32	- 0.008	0.951	466.8
	3wt.% Catalyst	29.43	15.64	0.957	302.3	14.47	0.36	0.961	526.9
	5wt.% Catalyst	33.15	54.40	0.964	311.0	- 3.77	- 0.007	0.985	467.5
F1	0wt.% Catalyst	34.60	100.58	0.969	310.0	1.37	0.009	0.739	466.8
	3wt.% Catalyst	31.24	26.54	0.959	302.3	31.01	13.76	0.942	526.9
	5wt.% Catalyst	36.28	132.50	0.966	311.0	1.66	0.011	0.995	467.5
F3/2	0wt.% Catalyst	37.36	220.24	0.968	310.0	7.00	0.16	0.993	466.8
	3wt.% Catalyst	32.67	40.10	0.960	302.3	48.07	396.23	0.914	526.9
	5wt.% Catalyst	38.82	271.50	0.965	311.0	6.93	0.14	0.991	467.5
F2	0wt.% Catalyst	40.32	506.62	0.966	310.0	13.76	1.35	0.998	466.8
	3wt.% Catalyst	34.15	61.42	0.960	302.3	68.78	19138.80	0.891	526.9
	5wt.% Catalyst	41.54	580.15	0.963	311.0	13.19	1.01	0.988	467.5
F3	0wt.% Catalyst	46.82	3079.50	0.958	310.0	29.98	90.43	0.998	466.8
	3wt.% Catalyst	37.28	150.02	0.959	302.3	117.95	1.34×10^8	0.864	526.9
	5wt.% Catalyst	47.45	2984.64	0.957	311.0	28.15	49.86	0.986	467.5
F4	0wt.% Catalyst	54.00	22073.82	0.946	310.0	48.46	7134.62	0.997	466.8
	3wt.% Catalyst	40.63	385.90	0.957	302.3	172.84	2.08×10^{12}	0.854	526.9
	5wt.% Catalyst	53.95	17731.88	0.947	311.0	45.27	2861.16	0.986	467.5
R1	0wt.% Catalyst	29.67	24.37	0.965	310.0	- 6.42	- 0.007	0.976	466.8
	3wt.% Catalyst	28.56	12.12	0.956	302.3	8.59	0.074	0.928	526.9

	5wt.% Catalyst	31.70	35.85	0.962	311.0	- 5.83	- 0.006	0.989	467.5
R2	0wt.% Catalyst	32.03	24.14	0.968	310.0	- 3.09	- 0.004	0.912	466.8
	3wt.% Catalyst	29.87	8.91	0.958	302.3	17.97	0.41	0.961	526.9
	5wt.% Catalyst	33.91	33.74	0.965	311.0	- 2.58	- 0.003	0.980	467.5
R3	0wt.% Catalyst	32.87	20.44	0.968	310.0	- 1.73	- 0.002	0.779	466.8
	3wt.% Catalyst	30.32	6.77	0.958	302.3	21.88	0.66	0.957	526.9
	5wt.% Catalyst	34.68	28.03	0.965	311.0	- 1.28	- 0.001	0.961	467.5
P2	0wt.% Catalyst	10.34	0.31	0.927	310.0	- 9.75	- 0.007	0.995	466.8
	3wt.% Catalyst	9.78	0.21	0.909	302.3	- 2.39	- 0.005	0.786	526.9
	5wt.% Catalyst	11.36	0.40	0.928	311.0	- 9.46	- 0.007	0.997	467.5
P3	0wt.% Catalyst	3.89	0.04	0.793	310.0	- 10.86	- 0.007	0.997	466.8
	3wt.% Catalyst	3.52	0.03	0.736	302.3	- 6.05	- 0.008	0.979	526.9
	5wt.% Catalyst	4.58	0.05	0.819	311.0	- 10.66	- 0.007	0.998	467.5
P4	0wt.% Catalyst	0.67	0.004	0.160	310.0	- 11.42	- 0.007	0.998	466.8
	3wt.% Catalyst	0.39	0.002	0.056	302.3	- 7.88	- 0.008	0.991	526.9
	5wt.% Catalyst	1.19	0.007	0.338	311.0	- 11.27	- 0.007	0.998	467.5
D1	0wt.% Catalyst	68.34	42277.84	0.973	310.0	0.25	0.0006	0.026	466.8
	3wt.% Catalyst	66.11	10920.30	0.967	302.3	30.56	4.56	0.976	526.9
	5wt.% Catalyst	72.40	84817.44	0.971	311.0	1.42	0.004	0.761	467.5
D2	0wt.% Catalyst	71.36	48108.04	0.974	310.0	4.08	0.012	0.870	466.8
	3wt.% Catalyst	67.82	8736.33	0.968	302.3	41.21	21.08	0.980	526.9
	5wt.% Catalyst	75.23	91206.20	0.972	311.0	5.21	0.02	0.988	467.5
D3	0wt.% Catalyst	74.72	26506.21	0.975	310.0	9.62	0.02	0.978	466.8
	3wt.% Catalyst	69.64	3184.46	0.968	302.3	57.13	105.40	0.972	526.9
	5wt.% Catalyst	78.35	46886.50	0.972	311.0	10.52	0.02	0.999	467.5

D4	0wt.% Catalyst	72.48	14461.45	0.975	310.0	5.89	0.006	0.936	466.8
	3wt.% Catalyst	68.43	2289.33	0.968	302.3	46.35	12.99	0.978	526.9
	5wt.% Catalyst	76.27	26792.20	0.972	311.0	6.94	0.007	0.996	467.5
A2	0wt.% Catalyst	12.80	0.72	0.946	310.0	- 5.86	- 0.01	0.989	466.8
	3wt.% Catalyst	11.13	0.34	0.922	302.3	8.82	0.13	0.856	526.9
	5wt.% Catalyst	13.65	0.86	0.942	311.0	- 5.71	- 0.01	0.998	467.5
A3	0wt.% Catalyst	5.54	0.08	0.881	310.0	- 8.27	- 0.01	0.996	466.8
	3wt.% Catalyst	4.42	0.04	0.807	302.3	1.42	0.007	0.287	526.9
	5wt.% Catalyst	6.10	0.09	0.882	311.0	- 8.17	- 0.009	0.998	467.5

Table 4.7 Represents the Thermodynamic parameters of the Optimum-Blend with two mass loadings at different temperature stages

		1st Stage (150 – 420 °C)			2nd Stage (420 – 660 °C)		
Symbols	**Sample Name**	ΔH (kJ/mol)	ΔG (kJ/mol)	ΔS (kJ/mol K)	ΔH (kJ/mol)	ΔG (kJ/mol)	ΔS (kJ/mol K)
F1/3	0wt.% Catalyst	26.38	159.63	- 0.23	- 10.47	Nil	Nil
	3wt.% Catalyst	24.64	160.34	- 0.24	7.82	223.80	- 0.27
	5wt.% Catalyst	28.30	160.08	- 0.23	- 9.93	160.50	- 0.23
F1	0wt.% Catalyst	29.75	158.31	- 0.22	- 4.78	217.10	- 0.30
	3wt.% Catalyst	26.46	159.63	- 0.23	24.36	216.10	- 0.24
	5wt.% Catalyst	31.42	158.88	- 0.22	- 4.50	159.91	- 0.22
F3/2	0wt.% Catalyst	32.51	157.30	- 0.21	0.85	205.10	- 0.28
	3wt.% Catalyst	27.89	159.08	- 0.23	41.41	210.78	- 0.21
	5wt.% Catalyst	33.97	157.94	- 0.21	0.77	160.34	- 0.22
F2	0wt.% Catalyst	35.47	156.20	- 0.21	7.61	198.73	- 0.26
	3wt.% Catalyst	29.37	158.52	- 0.22	62.13	205.70	- 0.18
	5wt.% Catalyst	36.68	156.96	- 0.21	7.03	161.44	- 0.21
F3	0wt.% Catalyst	41.97	153.95	- 0.19	23.83	189.10	- 0.22
	3wt.% Catalyst	32.50	157.38	- 0.22	111.30	196.00	- 0.11
	5wt.% Catalyst	42.59	154.92	- 0.19	21.99	165.22	- 0.19
F4	0wt.% Catalyst	49.15	151.58	- 0.18	42.31	180.70	- 0.19
	3wt.% Catalyst	35.84	156.21	- 0.21	166.20	186.68	- 0.03
	5wt.% Catalyst	49.09	152.77	- 0.18	39.12	170.13	- 0.18
R1	0wt.% Catalyst	24.82	160.30	- 0.23	- 12.57	Nil	Nil
	3wt.% Catalyst	23.77	160.70	- 0.24	1.94	228.40	- 0.28

	5wt.% Catalyst	26.85	160.65	- 0.23	- 12.00	161.18	- 0.23
R2	0wt.% Catalyst	27.18	162.67	- 0.23	- 9.24	Nil	Nil
	3wt.% Catalyst	25.10	163.48	- 0.24	11.32	226.36	- 0.27
	5wt.% Catalyst	29.05	163.15	- 0.23	- 8.74	164.48	- 0.23
R3	0wt.% Catalyst	28.02	164.31	- 0.23	- 7.88	Nil	Nil
	3wt.% Catalyst	25.54	165.24	- 0.24	15.23	227.10	- 0.26
	5wt.% Catalyst	29.82	164.82	- 0.23	- 7.44	166.80	- 0.24
P2	0wt.% Catalyst	5.49	162.10	- 0.27	- 15.90	Nil	Nil
	3wt.% Catalyst	5.00	161.31	- 0.27	- 9.04	Nil	Nil
	5wt.% Catalyst	6.50	162.15	- 0.27	- 15.61	186.10	- 0.27
P3	0wt.% Catalyst	- 0.95	165.74	- 0.29	- 17.01	Nil	Nil
	3wt.% Catalyst	- 1.26	164.69	- 0.29	- 12.70	Nil	Nil
	5wt.% Catalyst	- 0.28	165.40	- 0.28	- 16.82	197.72	- 0.29
P4	0wt.% Catalyst	- 4.18	173.71	- 0.31	- 17.57	Nil	Nil
	3wt.% Catalyst	- 4.39	174.41	- 0.31	- 14.53	Nil	Nil
	5wt.% Catalyst	- 3.67	171.40	- 0.30	- 17.43	208.30	- 0.30
D1	0wt.% Catalyst	63.49	162.77	- 0.17	- 5.90	232.97	- 0.32
	3wt.% Catalyst	61.33	165.70	- 0.18	23.91	222.97	- 0.25
	5wt.% Catalyst	67.54	163.62	- 0.16	- 4.74	118.77	- 0.17
D2	0wt.% Catalyst	66.51	165.16	- 0.17	- 2.07	218.15	- 0.30
	3wt.% Catalyst	63.04	168.48	- 0.18	34.56	223.44	- 0.24
	5wt.% Catalyst	70.37	166.10	- 0.16	- 0.95	121.72	- 0.17
D3	0wt.% Catalyst	69.87	171.42	- 0.17	3.47	219.81	- 0.29
	3wt.% Catalyst	64.85	175.12	- 0.19	50.48	228.65	- 0.22
	5wt.% Catalyst	73.49	172.44	- 0.17	4.36	130.65	- 0.17

D4	0wt.% Catalyst	67.63	172.11	- 0.18	- 0.27	224.38	- 0.30
	3wt.% Catalyst	63.64	175.49	- 0.19	39.70	231.80	- 0.24
	5wt.% Catalyst	71.41	173.08	- 0.17	0.79	130.84	- 0.18
A2	0wt.% Catalyst	7.95	160.50	- 0.26	- 12.00	Nil	Nil
	3wt.% Catalyst	6.34	160.38	- 0.27	2.17	224.82	- 0.28
	5wt.% Catalyst	8.79	160.70	- 0.26	- 11.87	184.72	- 0.27
A3	0wt.% Catalyst	0.69	163.63	- 0.28	- 14.42	Nil	Nil
	3wt.% Catalyst	- 0.36	163.40	- 0.28	- 5.23	237.09	- 0.30
	5wt.% Catalyst	1.25	163.63	- 0.28	- 14.33	195.80	- 0.28

The E_a and A in the first stage decrease for 3wt.%, therefore having a lower catalyst mass loading as compared to higher such as 5wt.%, thus indicating that by increasing the loading the E_a and A increase. In the second stage E_a and A increase for 3wt.% and then decreases for 5wt.% as compared to optimum blend as shown in Table 4.8. The kinetic analysis showed that the addition of the catalyst at 3wt.% loading to the optimum blend lowered the E_a and A of the optimum blend. It means that the CeO_2@MNA substantially increased the reaction rate, and reduced the E_a required for the decomposition process, thus inhibiting the formation of coke and deactivation of the catalyst. 3wt.% has lower E_a than 5wt.% and 0wt.% because in 5wt.% the E_a increases due to the accumulation of coke. This suggests that by further increasing the catalyst loading, the E_a will increase due to the increment of active acid sites. It was reaffirmed that the catalyst had a vital influence in decreasing these parameters. The decrease in E_a in the first and consequent increase in the second region could be attributed to the fact that at the final stage of catalytic co-pyrolysis, secondary cracking of intermediate compounds produced small molecules, leading to higher E_a in the later stages than in the first stage [60]. The ΔH followed the same pattern as for the E_a in the first stage it decreases for 3wt.% and then increases at a higher catalyst loading 5wt.%. However, the variation between E_a and ΔH was in the range of 4-6.8 $\mathrm{kJ/mol}$ in both the first and second stage, which indicates the reaction was possible to produce because of the small potential energy barrier [48, 49]. The values of ΔG in both stages follow the same pattern as ΔH for 3wt.% it increases and for 5wt.% it decreases. The positive values indicate that the reactions were complex

and that a suitable amount of external energy was required to speed up the reaction [45]. The negative values of ΔS indicate how close the system was to reaching its thermodynamic equilibrium. Low ΔS implies that the material has recently experienced some form of physical or chemical aging, bringing it to a state close to its thermodynamic equilibrium [37, 45]. In conclusion, the 3wt.% was the best combination through catalytic co-pyrolysis, which increases the WL% of the optimum blend (20BC-80AC) increasing its bio-oil yield.

Table 4.8 Comparison Table of co-pyrolysis and catalytic co-pyrolysis

	Co-pyrolysis		**Catalytic co-pyrolysis**			
	20BC-80AC/0wt.% catalyst		**3wt.% catalyst**		**5wt.% catalyst**	
	First Stage	**Second Stage**	**First Stage**	**Second Stage**	**First Stage**	**Second Stage**
Model Name	**D4**	**F2**	**D2**	**D2**	**D2**	**D3**
E_a	72.48 kJ/mol	13.76 kJ/mol	67.82 kJ/mol	41.21 kJ/mol	75.23 kJ/mol	10.52 kJ/mol
ΔH	67.63 kJ/mol	7.61 kJ/mol	63.04 kJ/mol	34.56 kJ/mol	70.37 kJ/mol	4.36 kJ/mol
ΔG	172.11 kJ/mol	198.73 kJ/mol	168.48 kJ/mol	223.44 kJ/mol	166.10 kJ/mol	130.65 kJ/mol
ΔS	−0.18 kJ/mol. k	−0.26 kJ/mol. k	−0.18 kJ/mol. k	−0.24 kJ/mol. k	−0.16 kJ/mol. k	−0.17 kJ/mol. k

A comparison of the previous studies on catalytic co-pyrolysis with the present study is presented in Table 4.9. The comparison of the blends along with a newly reported catalyst in the catalytic co-pyrolysis process with previously reported catalytic blends in the literature makes the competitiveness of the catalyst with the blends apparent in the process. The point-to-point comparison is not possible due to the different experimental and reactor configurations.

Table 4.9 Literature Comparison for Catalytic co-pyrolysis to the present study

Materials with Catalyst	**Catalytic Blends**	**Best Catalytic blend**	**Reaction Condition in TGA**	**Synergistic effects-Deviation (%)**	**Activation Energy-E_a (kJ/mol)**	**Ref.**
10%CeO_2@MNA / (20BC-80AC)	0wt.% 3wt.% 5wt.%	3wt.% with an increase in WL% from 45.9% to 68.7%	T = 25 – 900 °C Heating Rate = 20 °C/min	3.55%	67.82 kJ/ mol	Present work
Cellulose, Douglas Fir, and LDPE with HZSM-5	Ratio of 4:1	DF-LDPE-Catalyst	T = 25 – 600 °C, Heating Rate = 20 °C/min	NR	54.51 kJ/ mol	[61]
Seaweeds and HDPE with HZSM-5	Ratio of 1:1:2	Seaweeds-HDPE-HZSM-5,	T = 25 – 800 °C, Heating Rate = 10, 20, 30 and 40 °C/min	NR	(104.21-113.78) kJ/ mol	[62]
Microalgae and polypropylene with HZSM-5	Ratio of 1:1:1	NS and PP with HZSM-5	T = 25 – 900 °C, Heating Rate = 20 °C/min	NR	NR	[44]
Spirulina and oil shale with CaO and HZSM-5	3CaO1HZSM-5 1CaO1HZSM-5 1CaO3HZSM-5	SP and OS with 1CaO3HZSM-5	T = 25 – 900 °C, Heating Rate = 20 °C/min	NR	192.53 kJ/ mol	[54]
Kukersite oil shale and black pine wood with HZSM-5(23), HBETA(25), and HY(30)	(BPW/KOS: 1/1) and catalyst to sample weight ratio (3/1)	-	T = 25 – 800 °C Heating Rate = 10 °C/min	NR	22.8 kJ/mol 20.3 kJ/mol 22.2 kJ/mol	[63]

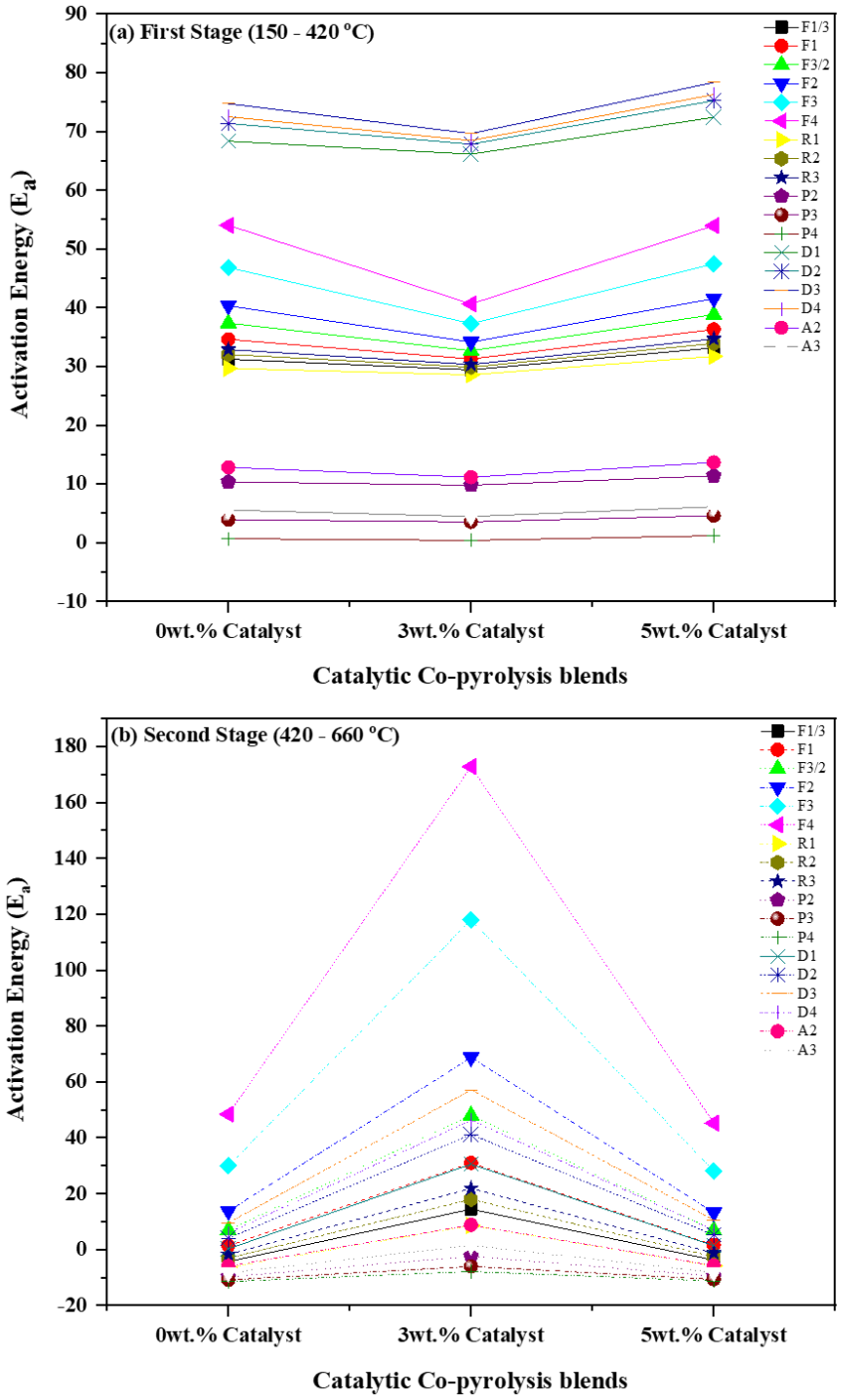

Fig. 4.12 E_a for different models of the optimum blend at two Catalyst Loadings (a) First stage (b) Second stage

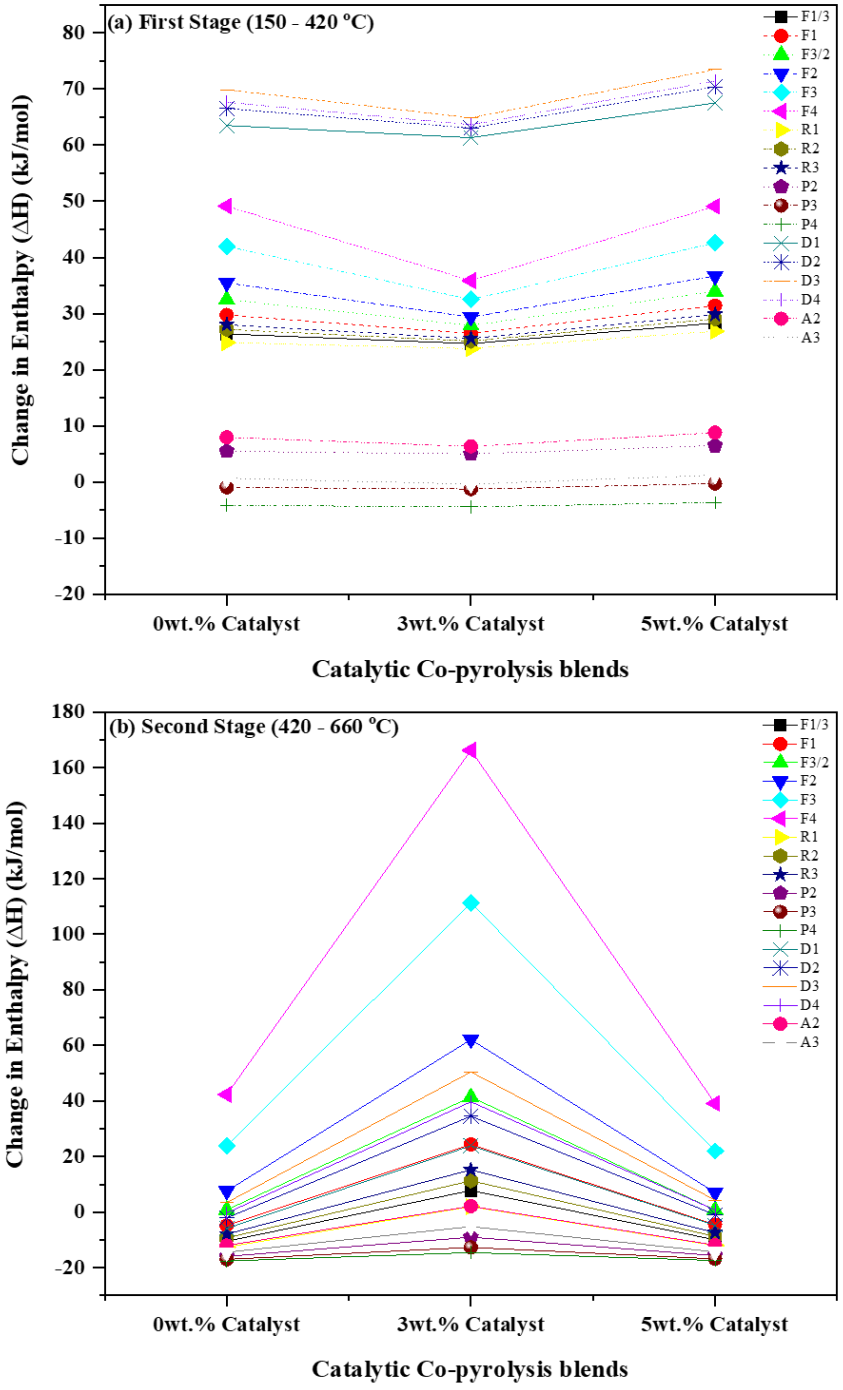

Fig. 4.13 Enthalpy for different models of the optimum blend at two catalyst loadings (a) (ΔH) in the First stage (b) (ΔH) in the Second stage

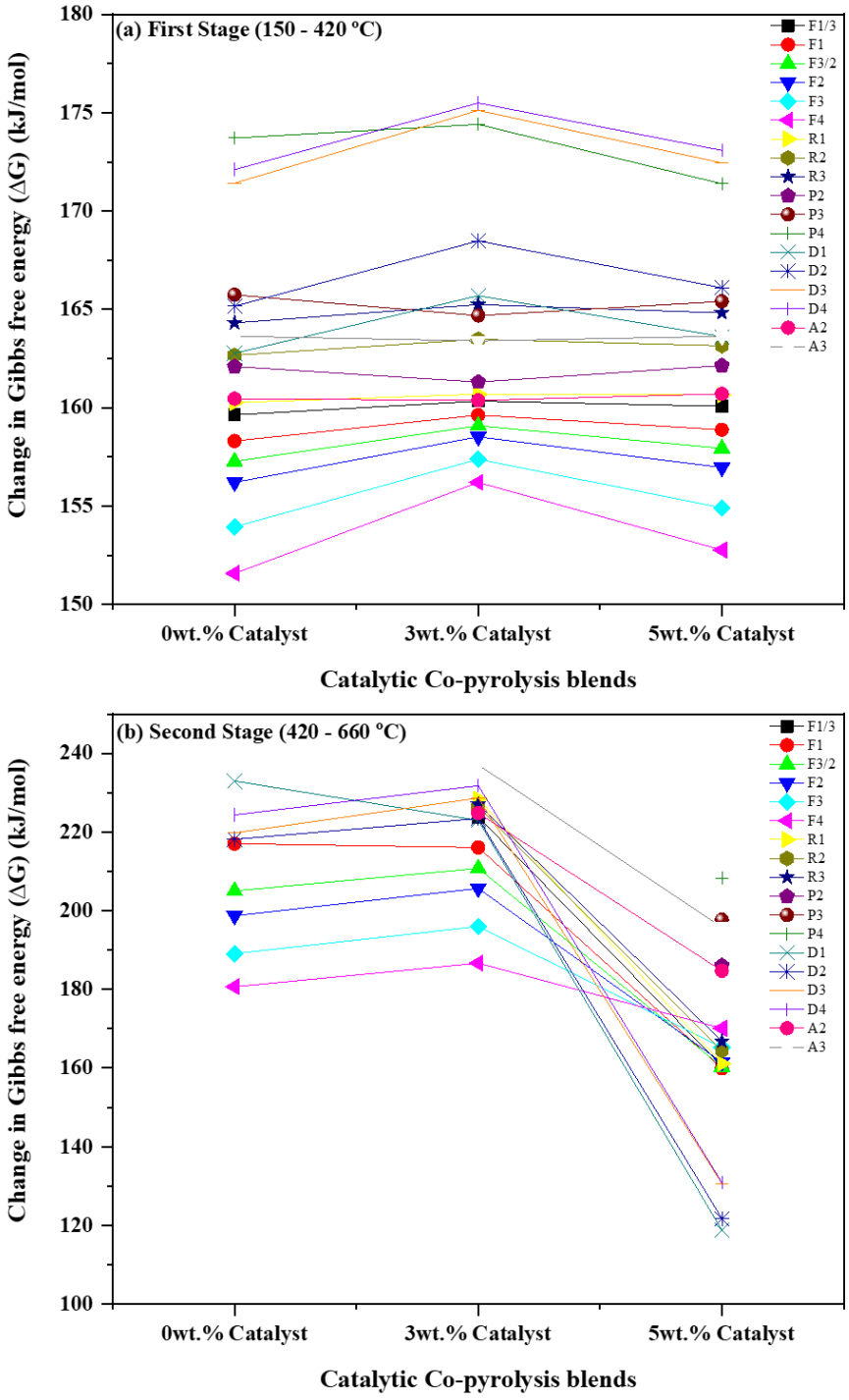

Fig. 4.14 Gibbs free energy for different models of the optimum blend at two catalyst loadings (a) (ΔG) in First Stage (b) (ΔG) in Second Stage

References

1. Coimbra, R.N., C. Escapa, and M. Otero, *Comparative Thermogravimetric Assessment on the Combustion of Coal, Microalgae Biomass and Their Blend.* Energies, 2019. **12**(15): p. 2962.
2. Sun, J., B. Zhao, and Y. Su, *Advanced control of NO emission from algal biomass combustion using loaded iron-based additives.* Energy, 2019. **185**: p. 229-238.
3. Kirtania, K. and S. Bhattacharya, *Pyrolysis kinetics and reactivity of algae–coal blends.* Biomass and Bioenergy, 2013. **55**: p. 291-298.
4. Geng, C., et al., *Pyrolysis characteristics of bituminous coal.* Journal of the Energy Institute, 2016. **89**(4): p. 725-730.
5. Chen, X., et al., *Pyrolysis Characteristics and Kinetics of Coal–Biomass Blends during Co-Pyrolysis.* Energy & Fuels, 2019. **33**(2): p. 1267-1278.
6. Erdogan, F.O. and T. Kopac, *Highly Effective Activated Carbons from Turkish–Kozlu Bituminous Coal by Physical and KOH Activation and Sorption Studies with Organic Vapors.* International Journal of Chemical Reactor Engineering, 2019. **17**(5).
7. Kawale, H.D. and N. Kishore, *Production of hydrocarbons from a green algae (Oscillatoria) with exploration of its fuel characteristics over different reaction atmospheres.* Energy, 2019. **178**: p. 344-355.
8. Chaiwong, K., et al., *Study of bio-oil and bio-char production from algae by slow pyrolysis.* Biomass and Bioenergy, 2013. **56**: p. 600-606.
9. Bird, M.I., et al., *Algal biochar – production and properties.* Bioresource Technology, 2011. **102**(2): p. 1886-1891.
10. Anukam, A.I., et al., *Blending Influence on the Conversion Efficiency of the Cogasification Process of Corn Stover and Coal.* Journal of Chemistry, 2016. **2016**: p. 3910986.
11. Channiwala, S.A. and P.P. Parikh, *A unified correlation for estimating HHV of solid, liquid and gaseous fuels.* Fuel, 2002. **81**(8): p. 1051-1063.
12. Vhathvarothai, N., J. Ness, and Q.J. Yu, *An investigation of thermal behaviour of biomass and coal during copyrolysis using thermogravimetric analysis.* International Journal of Energy Research, 2014. **38**(9): p. 1145-1154.
13. Bielowicz, B., *Petrographic Characteristics of Coal Gasification and Combustion by-Products from High Volatile Bituminous Coal.* Energies, 2020. **13**(17): p. 4374.
14. Gautam, R. and R. Vinu, *Reaction engineering and kinetics of algae conversion to biofuels and chemicals via pyrolysis and hydrothermal liquefaction.* Reaction Chemistry & Engineering, 2020. **5**(8): p. 1320-1373.
15. Raikova, S., et al., *Towards a marine biorefinery through the hydrothermal liquefaction of macroalgae native to the United Kingdom.* Biomass and Bioenergy, 2017. **107**: p. 244-253.
16. Zhou, Y., et al., *Surface hydrophobicity of sub-bituminous and meta-bituminous coal and their flotation kinetics.* Fuel, 2019. **242**: p. 416-424.
17. Shi, Q., et al., *An experimental study on the effect of igneous intrusions on chemical structure and combustion characteristics of coal in Daxing Mine, China.* Fuel, 2018. **226**: p. 307-315.
18. Liu, X., et al., *Oxidation reactivity and kinetic analysis of bituminous coal char from high-temperature pyrolysis: Effect of heating rate and pyrolysis temperature.* Thermochimica Acta, 2020. **690**: p. 178660.

19. Tian, B., et al., *Structural features and thermal degradation behaviors of extracts obtained by heat reflux extraction of low rank coals with cyclohexanone.* Journal of Analytical and Applied Pyrolysis, 2017. **124**: p. 266-275.
20. Zhang, T., et al., *Formation of carbon nanotubes from potassium catalyzed pyrolysis of bituminous coal.* Fuel, 2019. **239**: p. 230-238.
21. Gao, R., et al., *Effect of temperature and hydrogen on product distribution and evolution of char structure during pyrolysis of bituminous coal in a drop tube furnace.* Fuel, 2020. **267**: p. 117078.
22. Sharma, J., et al., *Enhancement of lipid production from algal biomass through various growth parameters.* Journal of Molecular Liquids, 2018. **269**: p. 712-720.
23. Ong, M.Y., et al., *Characterization and Analysis of Malaysian Macroalgae Biomass as Potential Feedstock for Bio-Oil Production.* Energies, 2019. **12**(18): p. 3509.
24. Zheng, S., et al., *Role of extracellular polymeric substances on the behavior and toxicity of silver nanoparticles and ions to green algae Chlorella vulgaris.* Science of The Total Environment, 2019. **660**: p. 1182-1190.
25. Carpio, R.B., et al., *Characterization and thermal decomposition of demineralized wastewater algae biomass.* Algal Research, 2019. **38**: p. 101399.
26. Fawzy, M.A., *Biosorption of copper ions from aqueous solution by Codium vermilara: Optimization, kinetic, isotherm and thermodynamic studies.* Advanced Powder Technology, 2020. **31**(9): p. 3724-3735.
27. Cao, B., et al., *Synergistic effects of co-pyrolysis of macroalgae and polyvinyl chloride on bio-oil/bio-char properties and transferring regularity of chlorine.* Fuel, 2019. **246**: p. 319-329.
28. Rasam, S., et al., *Insights into the co–pyrolysis of olive stone, waste polyvinyl chloride and Spirulina microalgae blends through thermogravimetric analysis.* Algal Research, 2022. **62**: p. 102635.
29. Adewole, B.Z., et al., *CO-pyrolysis of bituminous coal and coconut shell blends via thermogravimetric analysis.* Energy Sources, Part A: Recovery, Utilization, and Environmental Effects, 2020: p. 1-14.
30. Dwivedi, K.K., et al., *A comparative study on pyrolysis characteristics of bituminous coal and low-rank coal using thermogravimetric analysis (TGA).* International Journal of Coal Preparation and Utilization, 2019: p. 1-11.
31. Lin, Y., et al., *Thermogravimetric analysis of pyrolysis kinetics of Shenmu bituminous coal.* Reaction Kinetics, Mechanisms and Catalysis, 2014. **113**(1): p. 269-279.
32. Zhong, L., J. Zhang, and Y. Ding, *Energy Utilization of Algae Biomass Waste Enteromorpha Resulting in Green Tide in China: Pyrolysis Kinetic Parameters Estimation Based on Shuffled Complex Evolution.* Sustainability, 2020. **12**(5): p. 2086.
33. Badshah, S.L., et al., *Pyrolysis of the freshwater macroalgae Spirogyra crassa: Evaluating its bioenergy potential using kinetic triplet and thermodynamic parameters.* Renewable Energy, 2021. **179**: p. 1169-1178.
34. Gao, W., et al., *Thermal pyrolysis characteristics of macroalgae Cladophora glomerata.* Bioresource Technology, 2017. **243**: p. 212-217.
35. Yang, Z., et al., *Recent advances in co-thermochemical conversions of biomass with fossil fuels focusing on the synergistic effects.* Renewable and Sustainable Energy Reviews, 2019. **103**: p. 384-398.

36. Su, G., et al., *Co-pyrolysis of microalgae and other biomass wastes for the production of high-quality bio-oil: Progress and prospective.* Bioresource Technology, 2021: p. 126096.
37. Merdun, H. and Z.B. Laougé, *Kinetic and thermodynamic analyses during co-pyrolysis of greenhouse wastes and coal by TGA.* Renewable Energy, 2021. **163**: p. 453-464.
38. Alam, M., et al., *Co-pyrolysis of bamboo sawdust and plastic: Synergistic effects and kinetics.* Renewable Energy, 2020. **149**: p. 1133-1145.
39. Lin, B., et al., *Thermal behavior and gas evolution characteristics during co-pyrolysis of lignocellulosic biomass and coal: A TG-FTIR investigation.* Journal of Analytical and Applied Pyrolysis, 2019. **144**: p. 104718.
40. Hameed, Z., et al., *Kinetic and Thermodynamic Analyses of Sugar Cane Bagasse and Sewage Sludge Co-pyrolysis Process.* Energy & Fuels, 2018. **32**(9): p. 9551-9558.
41. Uzoejinwa, B.B., et al., *Co-pyrolysis of seaweeds with waste plastics: modeling and simulation of effects of co-pyrolysis parameters on yields, and optimization studies for maximum yield of enhanced biofuels.* Energy Sources, Part A: Recovery, Utilization, and Environmental Effects, 2020. **42**(8): p. 954-978.
42. Naqvi, S.R., et al., *Synergistic effect on co-pyrolysis of rice husk and sewage sludge by thermal behavior, kinetics, thermodynamic parameters and artificial neural network.* Waste Management, 2019. **85**: p. 131-140.
43. Naqvi, S.R., et al., *Assessment of agro-industrial residues for bioenergy potential by investigating thermo-kinetic behavior in a slow pyrolysis process.* Fuel, 2020. **278**: p. 118259.
44. Qi, P., et al., *Production of aromatic hydrocarbons by catalytic co-pyrolysis of microalgae and polypropylene using HZSM-5.* Journal of Analytical and Applied Pyrolysis, 2018. **136**: p. 178-185.
45. Ming, X., et al., *Thermal degradation of food waste by TG-FTIR and Py-GC/MS: Pyrolysis behaviors, products, kinetic and thermodynamic analysis.* Journal of Cleaner Production, 2020. **244**: p. 118713.
46. Tian, H., et al., *Co-pyrolysis of Miscanthus Sacchariflorus and coals: A systematic study on the synergies in thermal decomposition, kinetics and vapour phase products.* Fuel, 2020. **262**: p. 116603.
47. Saeed, S., et al., *Determination of Kinetic and Thermodynamic Parameters of Pyrolysis of Coal and Sugarcane Bagasse Blends Pretreated by Ionic Liquid: A Step towards Optimization of Energy Systems.* Energies, 2021. **14**(9): p. 2544.
48. Badshah, S.L., et al., *Kinetic and thermodynamics study of the pyrolytic process of the freshwater macroalga, Chara vulgaris.* Journal of Applied Phycology, 2021: p. 1-11.
49. Florentino-Madiedo, L., et al., *Evaluation of synergy during co-pyrolysis of torrefied sawdust, coal and paraffin. A kinetic and thermodynamic study.* Fuel, 2021. **292**: p. 120305.
50. Parthasarathy, P., et al., *Thermal degradation characteristics and gasification kinetics of camel manure using thermogravimetric analysis.* Journal of Environmental Management, 2021. **287**: p. 112345.
51. Vasudev, V., X. Ku, and J. Lin, *Pyrolysis of algal biomass: Determination of the kinetic triplet and thermodynamic analysis.* Bioresource Technology, 2020. **317**: p. 124007.
52. Ni, Z., et al., *Investigation of the co-pyrolysis of coal slime and coffee industry residue based on machine learning methods and TG-FTIR: Synergistic effect, kinetics and thermodynamic.* Fuel, 2021. **305**: p. 121527.

53. Ul Hasnain, M.A., et al., *Partial oxidation of methane over CeO2 loaded hydrotalcite (MgNiAl) catalyst for the production of hydrogen rich syngas (H2, CO).* International Journal of Hydrogen Energy, 2021. **46**(74): p. 36663-36677.
54. Dai, M., et al., *Behaviors, product characteristics and kinetics of catalytic co-pyrolysis spirulina and oil shale.* Energy conversion and Management, 2019. **192**: p. 1-10.
55. Bhoi, P., et al., *Recent advances on catalysts for improving hydrocarbon compounds in bio-oil of biomass catalytic pyrolysis.* Renewable and Sustainable Energy Reviews, 2020. **121**: p. 109676.
56. Rong, L., et al., *Effect of rare earth oxides on the formation of gaseous products from low rank coal pyrolysis.* Energy Sources, Part A: Recovery, Utilization, and Environmental Effects, 2021: p. 1-14.
57. Aysu, T., M.M. Maroto-Valer, and A. Sanna, *Ceria promoted deoxygenation and denitrogenation of Thalassiosira weissflogii and its model compounds by catalytic in-situ pyrolysis.* Bioresource technology, 2016. **208**: p. 140-148.
58. Andrade, L., et al., *Characterization and product formation during the catalytic and non-catalytic pyrolysis of the green microalgae Chlamydomonas reinhardtii.* Renewable Energy, 2018. **119**: p. 731-740.
59. Balasundram, V., et al., *Thermogravimetric catalytic pyrolysis and kinetic studies of coconut copra and rice husk for possible maximum production of pyrolysis oil.* Journal of Cleaner Production, 2017. **167**: p. 218-228.
60. Wang, L., et al., *Thermal decomposition behavior and kinetics for pyrolysis and catalytic pyrolysis of Douglas fir.* RSC advances, 2018. **8**(4): p. 2196-2202.
61. Zhang, X., et al., *Thermal behavior and kinetic study for catalytic co-pyrolysis of biomass with plastics.* Bioresource technology, 2016. **220**: p. 233-238.
62. Xu, S., et al., *Synergistic effects of catalytic co-pyrolysis of macroalgae with waste plastics.* Process Safety and Environmental Protection, 2020. **137**: p. 34-48.
63. Park, Y.-K., et al., *In-situ catalytic co-pyrolysis of kukersite oil shale with black pine wood over acid zeolites.* Journal of Analytical and Applied Pyrolysis, 2021. **155**: p. 105050.

Chapter 5 Conclusions and Recommendations

5.1 Conclusions

This study provides in-depth knowledge about the co-pyrolysis of BC-AC blends that were prepared in different ratios, they were evaluated through their Physiochemical characterization i.e. CHN-S, GCV, and FTIR which confirmed their potential for bioenergy production. The co-pyrolysis process on the blends was carried out in a thermo-gravimetric analyzer (TGA) at a heating rate of 10 °C/min to study their thermal decomposition behavior. Based on TGA analysis, synergistic effects of the blends were calculated. Co-pyrolysis results indicated slight interaction between the materials. The one having the best value of positive synergistic effects in terms of weight loss WL% was selected as an optimum blend i.e. (20BC-80AC) out of all the other blends. Kinetic parameters of all the blends were investigated from the TGA data by employing the model-fitting approach i.e. Coats-Redfern integral method through eighteen reaction mechanisms. For the optimum blend, the model with the highest value of linear regression (R^2) was selected in both decomposition stages, in the first stage D2 model was selected having activation energy (E_a) of (76.35 kJ/mol) with a pre-exponential factor (A) of (93579.64 min^{-1}) and in the second stage F2 model was selected with activation energy (E_a) of (15.33 kJ/mol) with a pre-exponential factor (A) of (1.13 min^{-1}) respectively. The addition of 100%AC to 100%BC appreciably decreases the activation energy (E_a) of 100%AC. The thermodynamic parameters were also calculated by the data of kinetics, the values of (ΔH) and (ΔG) showed positive values for BC-AC blends, while (ΔS) was negative for BC-AC blends. For the optimum blend the value of (ΔH), (ΔG), and (ΔS) in the first stage was (71.57 kJ/mol), (165.62 kJ/mol), and (-0.16 kJ/mol k), whereas for the second stage they were (9.29 kJ/mol), (198.06 kJ/mol) and (-0.26 kJ/mol k), which shows that the reaction is endothermic, non-spontaneous and a more organized structure compared to the initial substance, respectively. As the optimum blend produced more volatiles during co-pyrolysis and has lower activation energy, it could be a strong candidate for the production of bio-oil.

The co-pyrolysis and the catalytic co-pyrolysis of the optimum blend i.e. (20BC-80AC) in an in-situ mixing with the catalyst CeO_2@MNA in two proportions i.e. 3wt.% and 5wt.%

were carried out in thermo-gravimetric analyzer (TGA) at a heating rate of 20 °C/min. The results suggested that the presence of the catalyst further reduces the thermal decomposition temperature (T_p) of the optimum blend. The increased weight loss WL% of 68.7% for 3wt.% shows the beneficial effect towards a higher yield of volatile matter, which attributes to bio-oil production with less oxygenates, nitrogen, and water content. The catalyst CeO_2@MNA used, optimized the energy consumption and catalyst deactivation. The Kinetic triplets and thermodynamic Parameters were calculated for the optimum blend i.e. 0wt.%, 3wt.%, and 5wt.%. The activation energy (E_a) of Optimum Blend in co-pyrolysis was further lowered through catalytic co-pyrolysis i.e. in 3wt.% which showed excellent results. Overall from this investigation, the increasing performance of catalyst mass loading ratio on co-pyrolysis of the optimum blend is in the following order: 3wt.%> 5wt.%> 0wt.%. Hence, 3wt.% is a favorable catalyst mass loading that will reduce the cost of excessive catalyst usage in co-pyrolysis.

5.2 Recommendations

In the future, it is suggested that the catalytic co-pyrolysis of the optimum blend i.e. (20BC-80AC) using CeO_2@MNA catalyst should be conducted in a fixed bed reactor or fluidized bed reactor to clarify the product distribution. Although many co-pyrolysis and catalytic co-pyrolysis studies have been performed at the lab scale, only a few have been carried out at the pilot scale. Furthermore, the analysis of co-pyrolysis and catalytic co-pyrolysis bio-oil via gas chromatography-mass spectrometer (GC-MS) could be used to identify the major organic compounds present in bio-oil. The catalyst may be regarded as a promising method for the production of high-quality bio-oil. The statistics of kinetic triplets and thermodynamic parameters will be dynamic and useful for market scale catalytic co-pyrolysis of the best BC-AC blend for bioenergy use.

Appendix-A

“In-depth thermokinetic investigation on Co-pyrolysis of low-rank coal and algae consortium blends over CeO_2 loaded hydrotalcite (MgNiAl) catalyst”. ***Waqar Ul Habib Khan[1], Asif Hussain Khoja[1,]*, Hamad Gohar[1], Salman Raza Naqvi[2], Israf Ud Din[3], Brock Lumbers[4], Mohamed A. Salem[5,6], Abdullah A. Alzahrani[5].***

Journal of Environmental Chemical Engineering (Under Review) (IF = 7.968)